Break of Reciprocity on the Light Scattered by a Disordered Atomic Cloud

Thesis by
Pedro Henrique Nantes Magnani

In Partial Fulfillment of the Requirements for the
Degree of
Ph.D. in Atomic Physics

UNIVERSIDADE FEDERAL DE SÃO CARLOS
São Carlos, 2024

Thesis submitted through the doctorate program from the Physics Department in UFSCar in order to obtain a postgraduate degree in physics at the level of Doctor of Phylosophy.

Federal University of São Carlos - UFSCar
Physics Department - DF
Graduate Program

Advisor: Raul Celistrino Teixeira
São Carlos, 2024

Pedro Henrique Nantes Magnani
ORCID: 0000-0003-1195-9316

UNIVERSIDADE FEDERAL DE SÃO CARLOS

Centro de Ciências Exatas e de Tecnologia
Programa de Pós-Graduação em Física

Folha de Aprovação

Defesa de Tese de Doutorado do candidato Pedro Henrique Nantes Magnani, realizada em 07/03/2024.

Comissão Julgadora:

Prof. Dr. Raul Celistrino Teixeira (UFSCar)

Profa. Dra. Mônica Adrioli Caracanhas Santarelli (IFSC/USP)

Prof. Dr. Rodrigo Shiozaki (UFSCar)

Prof. Dr. Renné Medeiros Araujo (UFSC)

Prof. Dr. Emanuel Alves de Lima Henn (USP)

O Relatório de Defesa assinado pelos membros da Comissão Julgadora encontra-se arquivado junto ao Programa de Pós-Graduação em Física.

ACKNOWLEDGEMENTS

Este trabalho foi sem dúvidas umas das coisas mais difíceis que realizei até agora. A sensação de conseguir escrever esta tese está, ao mesmo passo, num dos melhores alívios que encontro. Enfrentar não somente desafios acadêmicos, comumente encontrados por qualquer colega que escolha trilhar este caminho, como também desafios pessoais e uma trágica e infeliz pandemia mundial, fizeram destes 5 anos uma experiência no mínimo marcante. Foi graças a diversas pessoas presentes em minha vida que pude enfrentar tudo isso e concluir um trabalho que hoje carrego com certo orgulho.

Primeiramente, gostaria de agradecer ao meu orientador, Raul Celistrino Teixeira. Tudo que sei e aprendi não só sobre o meio acadêmico mas também sobre a física que desenvolvemos vem da capacidade exemplar de explicação e conhecimento que você carrega, Raul. Não é exagero dizer que eu não seria nem metade do cientista que sou hoje se não tivesse você como orientador. Teve muita reviravolta nesse caminho, que já começou com a aventura da câmara explodindo e eu achando que meu mestrado tinha ido por água abaixo. Minha sorte foi que, junto da minha confiança que eu estava em boas mãos, você também depositou confiança no meu trabalho e acreditou no que eu poderia entregar. Fica aqui meu agradecimento por todo esse caminho e amizade.

Segundo, aos meus amigos de laboratório. Pablo, Marcia, Dalila, Claudio, Matheus e Gutavo. Vocês foram bem especiais nesses anos todos, compartilhando a rotina, as frustrações e as comemorações da vida acadêmica que a gente leva. São cientistas que tomo como exemplo, além de amigos que vou lembrar pro resto da vida, tenho certeza. Se teve um dia que o cantinho do Sr não foi algo divertido e acolhedor, eu com certeza vou dizer que estão alucinando. Agradeço também ao professor Philippe, que foi a ponte pra toda essa história ter começado. Além disso, aos amigos de São Carlos (e Rio Claro) que me acompanharam por todos esses anos, e fizeram das memórias que tive nessa cidade as melhores que pude carregar. Sem vocês eu jamais conseguiria chamar essa cidade de lar, e tenho muito orgulho de tudo que construímos nela. Aos amigos do discord, que carrego no coração com alegria e carinho pelas noites de conversa e jogatina. Também gostaria de dedicar agradecimentos a minha família e aos meus amigos de Rio Preto, que mesmo de longe nunca deixaram de demonstrar apoio nessa caminhada, o que foi muito importante pra eu saber que independente de qualquer coisa, sempre terei um porto seguro.

Por fim, gostaria de agradecer à CAPES pelo financiamento da minha bolsa de estudos, à USP pela infraestrutura proporcionada ao nosso laboratório e à UFSCar pelas histórias que vivi dentro do campus que vai ficar marcado, para mim, como o mais lindo que já passei.

"Hey yo, I'm just like my country
I'm young, scrappy and hungry
And I'm not throwin' away my shot!
...
If not, then I'll be Socrates
Throwing verbal rocks at these mediocrities!"
Hamilton

"You won't. That's all that it is, Miles. A leap of faith."
Spider-Man: Into the Spider-verse

"If you assume that there is no hope, you guarantee that there will be no hope. If you assume that there is an instinct for freedom, that there are opportunities to change things, then there is a possibility that you can contribute to making a better world."
Noam Chomsky

ABSTRACT

This study delves into interference phenomena, specifically exploring interference patterns arising from light scattered by a disordered assembly of cold atoms. The investigation focuses on disrupting optical path reciprocity within a mirror-assisted Coherent BackScattering setup (mCBS), where light scattered by a large cold atomic cloud interferes with its mirror image. The introduction of non-commuting polarizing optics, such as a birefringent mirror and a half-waveplate, reveals a reduction in contrast in the fringes, uncovering a geometric interpretation on the Poincaré sphere. The study examinated intensity profiles and fringes in two different clouds: a magneto-optical trap (MOT) based on the 689 nm transition and another on the 461 nm transition. The analysis involves fitting measured curves and understanding contrast reduction and phase shifts related to polarization changes. The study also explored the Pancharatnam-Berry phase, determining its impact on reciprocity in the system influenced by factors like finite optical density and the saturation parameter. The non-commutation of polarizing optics emphasizes the dependence of reciprocity on specific values of parameters. The mCBS configuration offers a distinctive setup, enabling the straightforward introduction of such non-commutative optics. Despite uncertainties, the agreement between theoretical predictions and experimental data validates the robustness of the study, providing valuable insights into the intricate interplay of experimental parameters and system characteristics. In a broader context, the experimental findings underscore the vectorial nature of light as a powerful tool for manipulating the reciprocity of interfering paths, impacting interference while preserving spectral and spatial coherence. This study opens avenues for further exploration in this complex and nuanced research domain.

RESUMO

Este estudo investiga fenômenos de interferência, explorando especificamente padrões de interferência gerados pela luz espalhada por um conjunto desordenado de átomos frios. A pesquisa concentra-se em perturbar a reciprocidade do caminho óptico dentro de uma configuração de Retroespalhamento Coerente assistido por espelho (mCBS), onde a luz dispersa por uma grande nuvem atômica fria interfere com sua imagem no espelho. A introdução de óptica polarizante não comutativa, como um espelho birrefringente e uma placa de meia onda, revela uma redução no contraste nas franjas, descobrindo uma interpretação geométrica na esfera de Poincaré. O estudo examinou perfis de intensidade e franjas em duas nuvens diferentes: uma armadilha magneto-óptica (MOT) baseada na transição de 689 nm e outra na transição de 461 nm. A análise envolve ajustar curvas medidas e compreender a redução de contraste e os deslocamentos de fase relacionados a mudanças de polarização. O estudo também explorou a fase Pancharatnam-Berry, determinando seu impacto na reciprocidade no sistema influenciado por fatores como densidade óptica finita e o parâmetro de saturação. A não comutação da óptica polarizante destaca a dependência da reciprocidade em valores específicos de parâmetros. A configuração mCBS oferece uma configuração distintiva, possibilitando a introdução direta de óptica não comutativa. Apesar das incertezas, a concordância entre as previsões teóricas e os dados experimentais valida a robustez do estudo, proporcionando valiosas insights sobre a intricada interação entre parâmetros experimentais e características do sistema. Em um contexto mais amplo, as descobertas experimentais destacam a natureza vetorial da luz como uma ferramenta poderosa para manipular a reciprocidade de caminhos interferentes, impactando a interferência enquanto preserva a coerência espectral e espacial. Este estudo abre caminhos para uma exploração mais aprofundada neste domínio de pesquisa complexo e sutil.

TABLE OF CONTENTS

Chapter 1

INTRODUCTION

Interference may be understood as a cornerstone in enhancing our comprehension of fundamental properties such as light's wave-like characteristics. Scientists and researchers have dedicated meticulous efforts to the construction of interferometers, specialized devices designed to exploit and manipulate the phenomenon of interference. These devices serve as powerful instruments, enabling us to not only witness but also explore elaborate interference patterns. Such patterns, in turn, give us invaluable insights into the inherent nature of light.

Among various examples of these systems are the well-known Michelson, Mach-Zender, and Young double-slit interferometers. Such creations have not only set their names in scientific history but have also yielded important discoveries, such as the wave nature of light and the aether non-existence. Serving as robust tools throughout the evolution of optics, these interferometers played a pivotal role in unraveling the mysteries of light and continue to be instrumental in ongoing explorations. Their significance lies not only in their historical contributions but also in their relevance as apparatus for probing the intricacies of optical phenomena [1].

Per definition, interference occurs when two waves are superimposed, combining their intensities or displacements while taking into account their phase difference. And here this combination may be seen as a vectorial operation, meaning the waves can both add or subtract *information* from each other, depending on how the interference phenomena happen. If two identical waves are precisely aligned, they can be manipulated to either cancel each other out or amplify their combined amplitude. Aligning crests with troughs results in cancellation, creating darkness, especially in the case of light waves. When crests align with crests, the waves add up, producing brighter light, as brightness correlates with amplitude for light. When the waves aren't identical, overlaying them creates alternating bands of brightness and darkness, forming an interference pattern. Utilizing this interference pattern for measurements is known as interferometry.

Astronomers have utilized interferometry, first pioneered by Martin Ryle in the 1960s [2], to create powerful virtual telescopes. Interferometry combines observations from multiple telescopes, enhancing resolution by analyzing interference patterns between waves taking different paths. Initially used in radio astronomy, it evolved to optical interferometry for higher precision, as exemplified and performed by the launch of Mark III Stellar Interferometer in the 80s [3]. Today, it's a key tool for measuring distant stars' rotation [4], detecting small movements [5], and guiding spacecraft with laser or radar-based precision [6]. Interferometry has revolutionized observational capabilities, with applications spanning astrophysics, geology, and space exploration [7]. Another notable example of how interferometric systems provide groundbreaking discoveries is the 2017

Nobel Prize-winning measurement of gravitational waves achieved by B.P. Abbott *et al* at LIGO (the Laser Interferometer Gravitational-Wave Observatory). Figure 1.1, presented in their own article, brings an illustration of what was done in order to achieve such measurement. It consists of two considerably large Michelson interferometer (one at Hanford, Washington - USA, and another at Livingston, Louisiana - USA). That because, considering that a strain h causes a shift ΔL in an initially unperturbed length L of an object, where their relation can be equated as:

$$\Delta L = hL, \tag{1.1}$$

then an expected strain of $\approx 10^{-21}$ caused by the gravitational waves means building large enough interferometer for it to detect such small value. Each arm was built with a length of 4 km, translating to 1200 km length in the optical path (each beam is reflected 300 times for the measurement to take place), assuring the necessary interferometer sensibility. LIGO's colossal and highly sensitive interferometer made it possible to detect strains in gravitational fields, demonstrating the tremendous utility of interferometric systems in unraveling the mysteries of the physical world [8].

The repercussion of interferometry's impact resonate not only in the greatness of the cosmos but also in the small realms of controlled laboratory experiments. Cold monoatomic gases, a sample that may be seen as a set of disordered scattering centers frozen in place for typical light scattering timescales, serve as interesting bases for controlled experiments due to their unique advantages. For example, they are devoid of vibrational-rotational degrees of freedom, allowing for a high degree of sample control, one of them being that, at low temperatures, we eliminate the inhomogeneous distribution of transition frequencies caused by the Doppler shift of individual atom resonances. The electronic simplicity of these elements allows for a meticulous manipulation of samples. Several laboratories use, for this purpose, elements belonging to the alkali metals group, such as Rb [9] and Na-K [10]. Contrastingly, alkaline earth metals (which have two electrons in their valence shell) such as strontium (Sr) exhibit distinctive properties not found in alkali metals: meta-stable states, narrow transition lines, and ground states free from any magnetic moment [11]. In our laboratory, we use the bosonic isotope ^{88}Sr, which offers, with its unique electronic structure providing narrow and broad transitions, the possibility to create magneto-optical traps where the trapped cloud can reach temperatures below 1 μK.

In fact, these type of disordered systems also provide us with enough controlled characteristics that new phenomena may be observed and studied. For example, in 1958, Philip W. Anderson demonstrated that when observing a two(or less)-dimensional system, any amount of disordering in your system provides the opportunity to detect the constructive interference between waves traveling along multiple paths, which enables the localization of the wave-function. Unlike in an ordered medium, where waves can propagate freely, in a disordered system, interference causes certain regions to experience constructive interference, trapping the waves in localized states. This

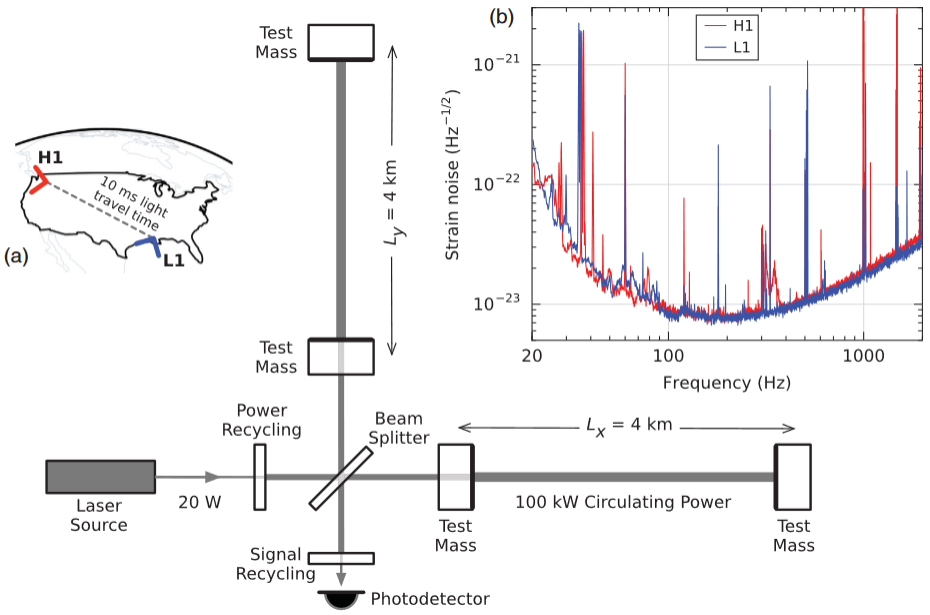

Figure 1.1: The diagram illustrates an Advanced LIGO detector, noting that it's not to scale. Gravitational waves, polarized parallel to the 4-km optical cavities and propagating orthogonally to the detector plane, cause length changes in the arms during half-cycles. The photodetector records these variations. While the detector's maximal directional response aligns with this case, it remains significant for other angles or polarizations due to gravitational waves freely traversing Earth. In the provided insets, (a) details the location and orientation of the LIGO detectors at Hanford, WA (H1) and Livingston, LA (L1), while (b) offers insight into the instrument noise for each detector around the time of signal detection. This noise is presented as an amplitude spectral density, denoted in terms of equivalent gravitational-wave strain amplitude. Notably, sensitivity is constrained by photon shot noise at frequencies surpassing 150 Hz and a combination of other noise sources at lower frequencies. Specific features within the narrow-band spectrum encompass calibration lines (33–38, 330, and 1080 Hz), vibrational modes of suspension fibers (500 Hz and harmonics), and 60 Hz electric power grid harmonics.

Source: [8]

effect is now commonly known as Anderson Localization. In three-dimensions, a type of disorder threshold arises, beyond which localization occurs [12].

One particularly intriguing manifestation of interference, central to this thesis, is the phenomenon known as Coherente BackScattering (CBS), illustrated at figure 1.2. Unlike classical diffuse scattering, that is responsible for what is known as speckle (which is formed when different optical paths for light beams passing through transmissible objects vary significantly in size on the scale of the wavelength [14]), CBS involves waves that scatter coherently in the backwards direction. It was demonstrated, in references [15] and [16] that this type of system provides an increase in the visibility of the interference pattern when observed in that specific direction, and the reason for that is because of the reciprocity that exists between the paths that the light may

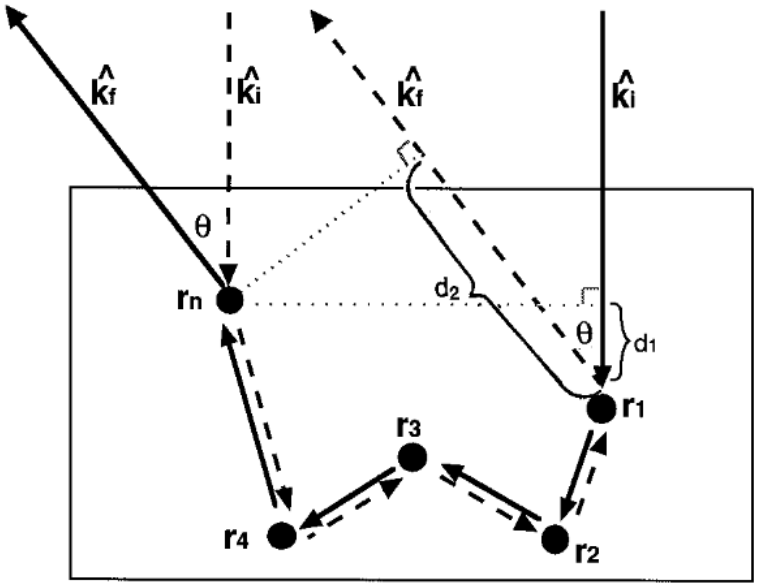

Figure 1.2: This illustration shows a scattering path (solid line) and its time-reversed counterpart (dashed line) for incident light (k_i) and final direction (k_f). Five scattering centers are indicated by positions r_1 to r_n, relative to an arbitrary origin. The optical path length difference between these paths depends on the physical difference ($d_2 - d_1$). The scattering angle (θ), relative to the backscattered direction ($-k_i$), is also depicted. For direct backscattering ($k_f = -k_i$) with θ at zero and $d_2 = d_1$, constructive interference occurs.

Source: [13]

travel. Essentially, reciprocity in this context may be understood as path's characteristics that represent the direction at which light travels through the system. The idea of this reciprocity and the paths along a CBS system in a mirror-assisted configuration (mirror-assisted Coherent BackScattering, mCBS) will be better explored in chapter 4, where the calculations for each of the possible paths the light may travel will be made and, eventually, an expression for the interference pattern' intensity will be found.

This system, governed by reciprocity, reveals a specific type of interference fringes, demonstrating the interplay between paths of equal length. What I aim to demonstrate within this thesis is that, at the specific regime of low saturation, the mCBS system configuration presents a break of said reciprocity. In the realm of optics, reciprocity manifests itself as the symmetrical transformation of waves traveling in opposite directions. Which brings this discussion to the context of symmetry.

Symmetries stands as fundamental properties inherent to a system, wielding the power to determine the conserved quantities governing its dynamic evolution [17], [18]. Among these symmetries, one that can be applied to all known forces and holds an important place in this context is the charge, parity and time reversal (CPT) symmetry. It is crucial to grasp the global nature

of this symmetry, considering all the three factors as a whole set instead of isolating one single aspect. To illustrate this principle, one can turn to classical optics for a straightforward example.

The CPT symmetry, a steady property in the scattering of light by particles when all degrees of freedom are under careful examination, encounters a subtle unfolding when attention is focused on coherently scattered light. As the scattering of electromagnetic energy in other modes, commonly encapsulated in the imaginary part of the medium refractive index, happens, the breakdown of symmetry becomes clear. This subtle occurrence induces a dissipative nature into the system, disrupting the previous equilibrium provided by the CPT symmetry. The challenge in this phenomenon arises from the necessity to discern absorption, a process that introduces an arrow for time and prevents time reversal symmetry, from alternative energy-preserving mechanisms that may incite a deviation in this symmetry [19], [20]. Actually, such challenge is what gave rise to the concept of reciprocity to begin with. In essence, reciprocity becomes a guiding principle that offers a specific point of view through which it is possible to untangle the complex interaction of symmetries and variations in the dynamic evolution of optical systems.

However, this symmetry, and therefore the reciprocity of our system, is disrupted by introducing non-commuting polarizing optics. When incorporating a birefringent mirror and a half-waveplate, the interference fringes suffers discernible changes. The consequential break of reciprocity is meticulously observed through the interference fringes produced in our setup, and the reduction in the contrast of these fringes directly stems from the non-commutative nature of the polarizing optics mentioned earlier. This lack of commutation is a crucial factor influencing the dynamics of light scattering in the experimental framework presented here.

To grasp this phenomenon better, a connection to the Poincaré sphere is made, where the contrast is linked to the geodesic distance between polarizations. Simultaneously, the phase difference, related to the Pancharatnam-Berry phase [21], [22], corresponds to the geodesic surface connecting injected and scattered polarizations. Such intricate relationship is investigated at our experiment by measuring the displacement of fringes, providing a geometrical interpretation that sheds light on the breaking of reciprocity. This approach not only expands our understanding of light interactions in disordered media but also offers a visual and geometric framework to comprehend the nuanced dynamics at play.

In Chapter II, the experimental setup (along with the samples created by it) will be presented, while at Chapter III the basic concepts of interference and interferometry are discussed. The goal is first to familiarize the reader with the experiment at our lab and the basic concepts of what I aim to investigate before continuing to the full disclosure of the investigation done in this work, along with the results and its discussion, presented at Chapter IV. Finally, Chapter V presents the conclusion of this work.

Chapter 2

EXPERIMENTAL SETUP

Within this chapter, my goal is to deliver a brief but detailed explanation of our experiment. Some information may be withhold but I'll do this for concise matters only. For this chapter to be fully understood, concepts as radiation pressure, detuning, resonance, ground and excited states, and so on should be familiar to the reader. If not, references such as [23] and [24] are a great way to accomplish that. If Portuguese is a language that the reader has a good understanding, I would like to add my masters dissertation [25] as a reference as well, since the reader will find there a much more detailed discussion not only about the concepts discussed in this chapter but also about our experiment, when compared to this thesis.

So, why write this chapter if I'm not doing it with all of its possible information? Well, this serves for two purposes: create a mental picture for the reader, so they have a better understanding about the experimental sequences involved, and detail the procedures on how we created the samples used in this work. This way the reader can feel a bit of familiarity with our experiment and, therefore, have a clearer picture of how the results presented were accomplished. For that, I first want to introduce the reader to a schematics of our experiment, seen at Figure 2.1. As seen, the experiment is divided into two main sections: the Oven Section (where the atoms are released and somewhat selected in order to create a collimated atomic beam) and the Science Chamber Section (where the atoms in such atomic beam are cooled down and trapped). Both sections are separated by a manual vacuum valve, the reason for that is to prevent that any accident in one section that takes place while we are not operating the experiment do not affect the other one. Actually, the whole part of the experiment where the atoms travel and are trapped is under vacuum. This is because we do not want collisions with the background gas to remove atoms from our cold atomic trap. To ensure that this is what happens, we work with ionic pumps that helps maintain $7,4 \times 10^{-10}$ mbar and $2,7 \times 10^{-9}$ mbar pressures on different parts of the experiment.

We begin our process at the Oven Section. The oven itself is a metallic tube, where we deposit a small amount of solid Strontium. This metallic tube is heated by three different resistances, one at its beginning, one at its end and the last one around all the tube. Each area heated by such resistances (beginning, end and the entire oven) operate at temperatures of 562 °C, 553 °C and 524 °C, respectively. Also, at the end of this tube, we have several micro-tubes, made from commercial needles with 130 μm internal and 300 μm external diameters, that are responsible for the collimation process of the atomic effusive beam [26]. To prevent thermal losses, the whole thing is wrapped with glass wool and aluminum foil. The result is a collimated atomic beam with atoms around 484 m/s leaving the micro-tubes, which means a thermal energy equivalent

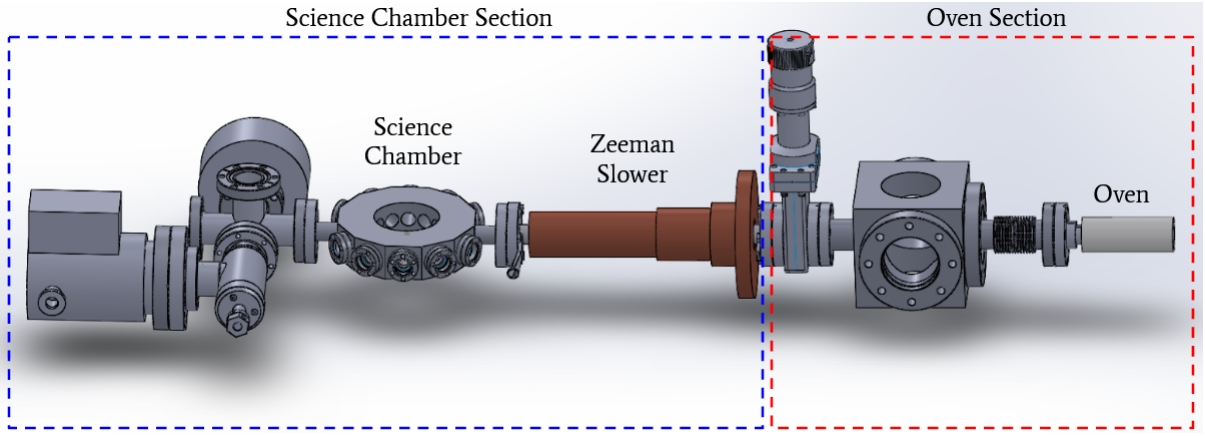

Figure 2.1: Schematics from our experiment, detailing both sections and its mainly apparatus.

Source: author

to temperatures of 823 K. Our samples operates at temperatures of mK and μK, so we need to cool down our samples several orders of magnitude for the trapping to be possible. The first step in order to do that is to use a Zeeman Slower so the atoms at the atomic beam are with a low enough kinetic energy. That requires using not only, as the name suggests, the Zeeman Effect at the energy levels but also radiation pressure so a counter-propagating laser beam (relative to the atomic beam) is always on resonance with the atoms. But what resonance mean for us?

2.1 Strontium

At our laboratory, we utilize the chemical element known as Strontium, specifically its bosonic isotope Strontium-88 (^{88}Sr). Strontium is an earth-alkaline metal, therefore having two valence electrons, which allows singlets and triplet states (total spin equals 0 and 1, respectively). Since it is a bosonic isotope, it is also worth to remember that it has a null total magnetic moment for its ground state ($J = 0$). Figure 2.2 shows some of the energy levels and transitions of ^{88}Sr.

The main transitions for our research are: the 461 nm (blue), with width $\Gamma = 30.5$ MHz and the 689 nm (red), with width $\Gamma = 7.6$ kHz. We also have the 497 nm (green) transition, used for repump. This is needed since, at a rate $1 : 50\,000$ transitions, the atoms from $[5s5p]^1P_1$ state may decay to the $[5s5p]^3P_J$ triplet states. Within these triplet states, the one with magnetic moment $J = 2$ has the property of being a meta stable state, which means it has a long lifetime ($\approx$ 1000s). As long as an atom is in such excited state, it doesn't suffer radiation pressure. The consequence is an atom not receiving any type of force to be trapped or cooled down, and therefore being free to fall out of our trapping region. Thus, the use of the green transition to repump the atoms from the $[5s5p]^3P_2$ state to the $[5s5d]^3D_2$ one. From there, they can decay to the $[5s5p]^3P_1$ state again and close the cycle for the blue transition.

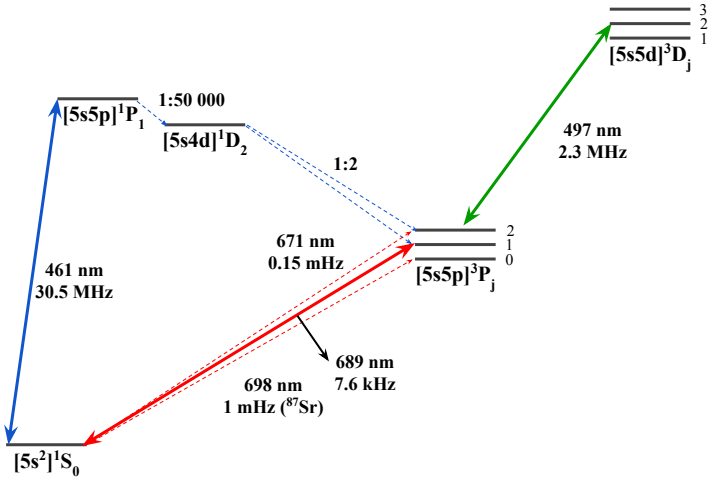

Figure 2.2: ^{88}Sr energy levels and transitions relevant for our experiment.

Source: [26] e [11], with modifications

2.2 Radiation Pressure

Being of vital importance in order to achieve our samples, the radiation pressure force helps to cool down the atoms in the collimated atomic beam produced by our oven since the goal is to trap them in a specific spatial region. Cool down, within the atomic physics context, means reducing their velocities, therefore meaning that an exchange in momentum between light and matter is occurring so this cooling process is possible. Thus a dissipative type of force known as radiation pressure is used. Considering a system where a photon and a two-level (ground and excited states) atom interacts, this force can be expressed as [25]:

$$\boldsymbol{F}_{dissipative} = \hbar \boldsymbol{k} \Lambda \tag{2.1}$$

Here, Λ is defined as:

$$\Lambda = \frac{s_0 \Gamma / 2}{1 + s_0 + \left(\frac{2(\Delta - \boldsymbol{k}\cdot\boldsymbol{v})}{\Gamma}\right)^2} \tag{2.2}$$

This represents the photon absorption rate by the atom. In these equations, $\hbar$ the Plank constant over 2π, $\Delta = \omega_L - \omega_0$ signifies the detuning of our laser compared to the transition resonance and $s_0 = \frac{I}{I_{sat}}$ denotes the resonance saturation parameter. The term $\boldsymbol{k} \cdot \boldsymbol{v}$, where $\boldsymbol{v}$ is the velocity of the atom, correlates with the Doppler effect experienced by the atom. Specifically, if we envision the photon traveling in the opposite direction to the atom, it will appear to the atom with a higher frequency than sent. Conversely, if we consider the same direction, it will be perceived with a lower frequency.

Consider a scenario in which a photon with momentum $\boldsymbol{p}_f = \hbar\boldsymbol{k}$ impinges on an atom. Upon absorption, the atom undergoes a recoil in its momentum of equivalent magnitude. By efficiently employing this effect in a continuous process, the cooling effect initiates. Consequently, the parameter Λ assumes the role of quantifying the photon absorption rate. Subsequent to photon absorption and the atom remaining in the excited state, spontaneous emission occurs. If the atom emits a photon (with a new momentum $\boldsymbol{p}'_f = \hbar\boldsymbol{k}' \neq \boldsymbol{p}_f$), it experiences a new recoil relative to $\boldsymbol{p}'_f$. Therefore, we have two events of momentum exchange: during the absorption process and during the emission process. The absorption process helps with decreasing the atom initial velocity and, hence, cooling down the atom while the emission process just makes the atom gain a new velocity to a random direction, which also means heating up the atom. However, emission manifests itself as an isotropic effect, where the average velocity contribution goes to zero. On the other hand, the mean squared velocity, $\langle v^2 \rangle$, is not, therefore explaining the heating process.

At equilibrium, the heating and cooling rates are equal, which sets a limit on the amount by which the atom can be cooled known as Doppler limit, given by:

$$k_B T_{min} = \frac{\hbar\Gamma}{2} \tag{2.3}$$

with k_B the Boltzmann constant and T_{min} the minimum possible temperature.

Since each transition has its own linewidth Γ, this means different Doppler limit Temperatures we can achieve with each transition. In the case of strontium, we found $T_{min} = 0.18$ μK for the Red transition and $T_{min} = 0.72$ mK for the Blue one. Comparing this with 2.1 it is also possible to notice how both these are affected by Γ inversely. That is, the broader the linewidth of the transition, the higher it is the radiation pressure the atom will suffer, but that also means a higher T_{min} achieveble due to the Doppler limit.

2.3 Zeeman Slower

As it was said before, the Zeeman Slower works upon a combination of the Zeeman Effect on the excited states of ^{88}Sr along with the radiation pressure from a counter-propagating laser beam. As the atoms suffers a recoil caused by the radiation pressure from the counter-propagating beam (which is already red-detuned in frequency due to Doppler effect), it will eventually become slow enough that the Doppler shift also changes, meaning the beam will no long be in resonance with the atom and, therefore, the cooling proccess will stop. Using for our advantage the magnetic field interaction for an atom with $J = 0 \rightarrow J = 1$ transition (our case), we can choose a magnetic field behavior that changes with the atom position, thus allowing a controlled change in the resonance frequency of the atom so it keeps in resonance with the laser, even considering the loss in velocity and the Doppler Effect. In theory, the ideal behavior for such magnetic field as a function of position is given by [25]:

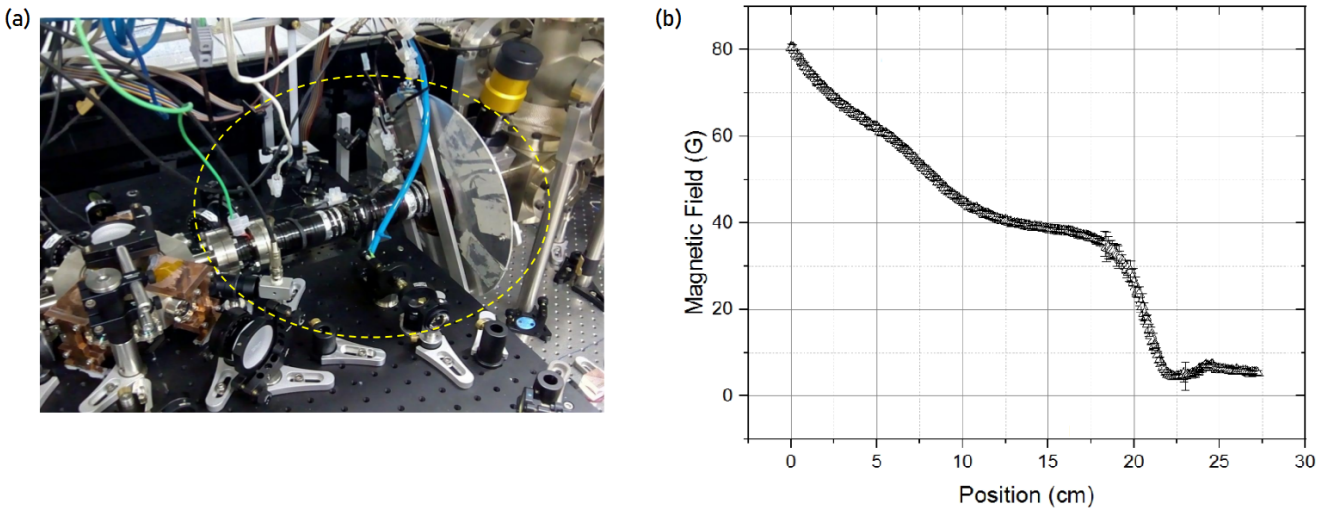

Figure 2.3: At (a), a photo of our Zeeman Slower, composed by different sections of a coil made out of rectangular cross-section copper wire, each section with a different number of layers. At (b) a graph of the magnetic field generated by our Zeeman Slower as a function of the position along our experiment. Since the internal passage for the atoms after the oven was too narrow for our magnetic field probe, the region with the biggest field value could not be measured. Therefore, the position's axis origin, even though being the region closest to the oven, is arbitrary. For scale and comparison reasons, the end of our oven is located at ≈ -28 cm and our atomic cloud at ≈ 35 cm.

$$B(x) = \frac{\hbar}{\mu_B}\left(\Delta + k\sqrt{{v_0}^2 - 2a_{cool}x}\right) \tag{2.4}$$

here, μ_B is the Bohr magneton, v_0 the atom initial velocity, x its position, k the wave vector and a_{cool} the atom deceleration.

At the experiment itself we tried to match this behavior. When measured, the behavior seen is the one depicted in Figure 2.3. At the figure, $x = 0$ represents the point at which the magnetic field measurement started, which experimentally means the position closest to our oven (≈ 28 cm from the outer face of the micro-tubes). As for further values of x means the further away we are from the such region. Meanwhile a simulation made for the atomic behavior for atoms with different class of velocities to its position, for our experiment's parameters, can be seen at Figure 2.4. At our experiment, the Zeeman Slower is made from a coil built with a 5 mm $\times$ 1 mm rectangular cross-section copper wire, plus a laser beam in resonance with our ^{88}Sr atoms. The coil is divided into six sections, divided by the number of layers in each one of them: 95, 35, 12, 11 and 8, being the one with 95 layers the one closest to the oven. With it, the mean velocity of the atoms at the atomic beam goes from the initial 484 m/s to tenths of m/s at the end of this apparatus [26]. With such considerable lower velocities, trapping the atoms into samples known as Magneto-Optical Traps is now possible.

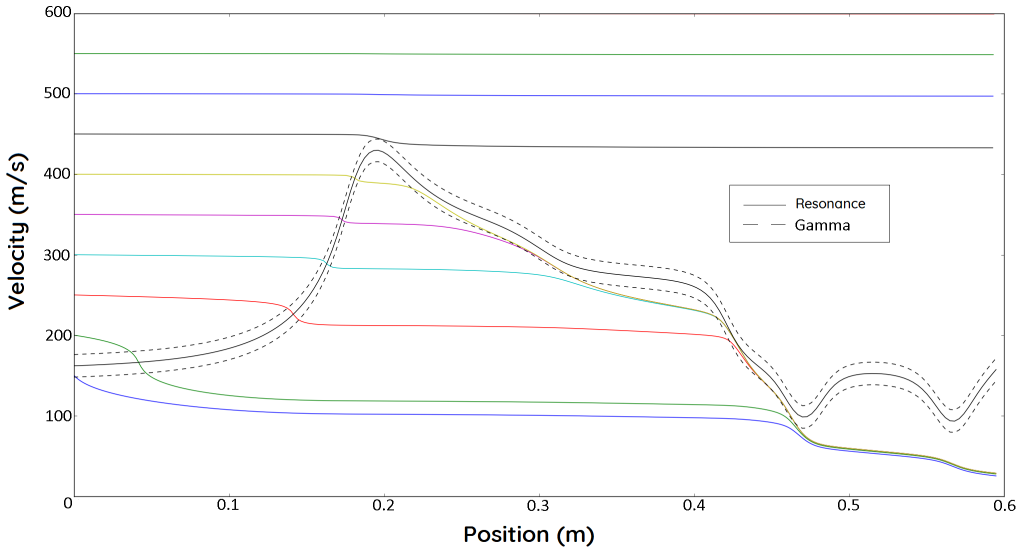

Figure 2.4: Graph for the numerical calculation of the atom velocity behavior with different initial velocities when at the Zeeman Slower, as a function of its position inside the same apparatus. The dotted line indicates the class of velocities that are in resonance with the laser, considering a linewidth of Γ to the resonance.

2.4 Magneto-Optical Traps

In order to create a Magneto-Optical Trap, or MOT for short, one does not simply cool down the atom using radiation pressure force indefinitely. It is necessary to be sure that the cooling effect is efficient continuously while the atoms you wish to trap remains confined in a specific region of space. That process involves the use of radiation pressure for sure, but here a modified version when compared to equation 2.1. At it, only one beam was considering interacting with the cloud. In reality, if you *hit* an atom with photons for enough time, its momentum will continuously suffer a recoil just as explained in section 2.2 until it begins not to reduce its velocity but actually gain a velocity in the photon's direction due to that momentum exchange. Therefore, a counter-propagating beam is necessary to avoid such effect. Consider a one dimensional example: an atom travels to the positive side of your axis. On it, you also have two beams: one behind the atom travelling at the same direction (beam 1), and another in front of the atom but on a counter-propagating direction (beam 2). Due to radiation pressure, the atom will display different behavior for each beam depending on their interaction. The force each one exerts on the atom is equal to:

$$F_1 = \hbar k \frac{s_0 \Gamma/2}{1 + s_0 + \left(\frac{2(\Delta - kv)}{\Gamma}\right)^2} \tag{2.5a}$$

$$F_2 = -\hbar k \frac{s_0 \Gamma/2}{1 + s_0 + \left(\frac{2(\Delta + kv)}{\Gamma}\right)^2} \tag{2.5b}$$

Since the Zeeman Slower apparatus at our experiment cool down the atoms to velocities close to cm/s, such forces will be acting upon a low velocity regime. Because of that, we can look only at the first order of the resultant force that acts upon the atom, where we have:

$$F_{res} \simeq 4\hbar k^2 s_0 \frac{(2\Delta/\Gamma)v}{\left(1+\left(\frac{2\Delta}{\Gamma}\right)^2\right)^2} \tag{2.6}$$

Which can be interpreted as:

$$F_{res} = -\alpha v \tag{2.7}$$

with $\alpha = -4\hbar k^2 s_0 \frac{(2\Delta/\Gamma)}{\left(1+\left(\frac{2\Delta}{\Gamma}\right)^2\right)^2}$.

Therefore, as long as we use a detuning $\Delta < 0$, the dissipative behavior of this resultant force is maintained. Now, MOTs are traps that uses not only the light-matter interaction that provides the radiation pressure but also adds a magnetic component to the equation due to the quadrupolar magnetic field present. The behavior of a quadrupole field, which can be created by coils in a anti-Helmholtz configuration (just as the case of our experiment), has a behavior given by $\boldsymbol{B}(x,y,z) = B_0(x\hat{x} + y\hat{y} - 2z\hat{z})$, which can be simplified to a one direction problem if we consider: $\boldsymbol{B} = B_0 x\hat{x}$, with $y = z = 0$. This behavior is responsible for creating an spatial modulation in the atomic resonance due to the Zeeman effect and, when used correctly, creates a confinement potential at the radiation pressure. Keeping the one dimensional example used just now, but here instead of having the atom travelling in a specific direction, we consider it remains still, the forces that each beam exerts in the atom will suffer a change in their expression and become:

$$F_1 = \hbar k \frac{s_0\Gamma/2}{1 + s_0 + \left(\frac{2(\Delta + \frac{\mu_B m_J B_0 x}{\hbar})}{\Gamma}\right)^2} \tag{2.8a}$$

$$F_2 = -\hbar k \frac{s_0\Gamma/2}{1 + s_0 + \left(\frac{2(\Delta - \frac{\mu_B m_J B_0 x}{\hbar})}{\Gamma}\right)^2} \tag{2.8b}$$

where, μ_B is Bohr's magneton resonance and m_J the quantum number associated to the magnetic moment.

Where now the resultant force of this magnetic component, considering the region near the origin ($x \to 0$), can be given by:

$$F_{res,mag} = k s_0 \frac{8\Delta\mu_B g_J m_J B_0}{\Gamma(1 + 4\Delta/\Gamma^2)^2} x \tag{2.9}$$

Which in turn can be interpreted as:

$$F_{res,mag} = -\beta x \tag{2.10}$$

with $\beta = -ks_0 \frac{8\Delta\mu_B g_J m_J B_0}{\Gamma(1+4\Delta/\Gamma^2)^2}$

Characterizing a confining force. This also indicates the polarization for each beam, since now we've also taken into account the magnetic effects on our atom due to the Zeeman effect. In this case, the best polarization to be chosen is ζ^+ (counterclockwise circular polarization) for beam 1 and ζ^- (clockwise circular polarization) for beam 2. That is, the beam propagating from the right (left) with polarization ζ^- (ζ^+) will exert maximum force on atoms displaced to the right (left) relative to the center of the quadrupole magnetic field.

Therefore, we now have forces that acts upon the atoms that not only cool them down but also confine them to the region of least potential. The force that acts upon the atom in order to trap it in a MOT is the sum of both these resultant forces which, in the limit of low light intensity, can be simplified to the following expression [27]:

$$F_{MOT} = -\alpha v - \beta x \tag{2.11}$$

2.5 Acquiring our Samples

Now that I have explained what chemical element we work with along with how the radiation pressure works, it is time to explain how the samples used within this work were acquired. Due to the strontium levels depicted in figure 2.2, we need to operate with lasers that achieve the main transitions, that is, we need lasers that can operate with a wavelength of 461 nm, 689 nm and 497 nm. Because of that, the following subsections will present the systems for each one of this transitions used at our laboratory, along with a schematic of how these lasers are installed.

Blue System

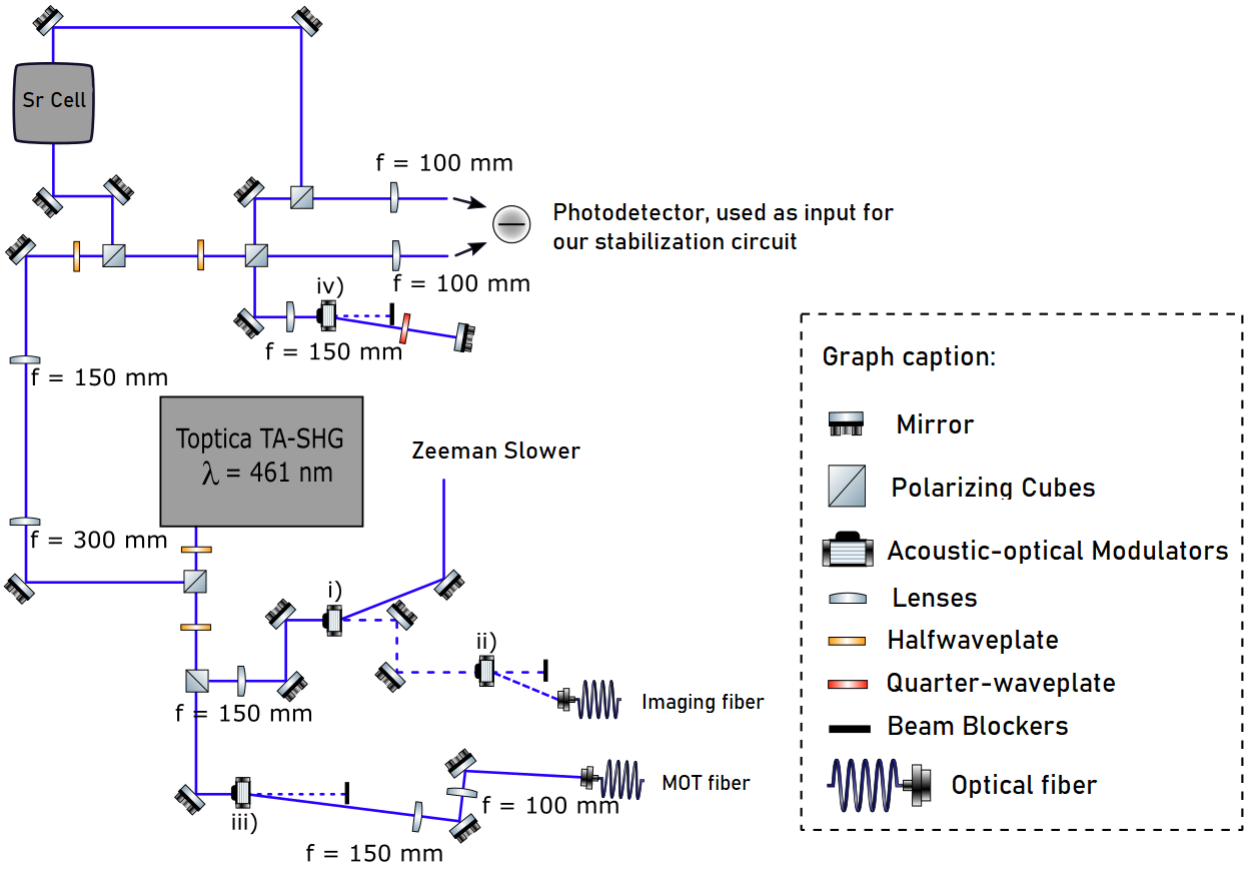

Figure 2.5: Simplified schematic of the blue laser system.

Source: author.

The generation of the blue laser involves the use of a commercial laser diode with frequency doubling from Toptica Photonics. Specifically, we employ the TA-SHG pro model, resulting in a final wavelength of 461 nm. This blue laser serves multiple purposes in our experimental setup, illustrated in Figure 2.5. To realize this configuration, a set of acoustic-optical modulators (AOM) is employed. These AOMs use principles such as radio-frequencies and the refractive index of materials to alter the diffraction order of the laser. Such behavior mimics Bragg diffraction and is important in order to achieve the desired configuration in the Blue System. The first two purposes of the Blue System are:

- Zeeman Slower Beam: This beam, as detailed in Section 2.3, is used in the Zeeman Slower apparatus as a counter-propagating beam in order to cool the collimated atomic beam originated from the oven.

- Counter-Propagating Beams for BlueMOT: due to the behavior of the forces that govern the MOT and the order cited in the last section, these beams are crucial in the establishment of the samples in our experiment, being responsible for creating the BlueMOT.

A third and also important application of the Blue System is the use of a separate beam for the absorption imaging process. Such process consists of taking a set of three shots:

1. Atoms Image: the first image is an image with everything on (atomic cloud captured, all lasers on and any residual light of both the room and the experiment).
2. Probe image: for the second, we take an image where the cloud is no longer captured (so to see the probe light intensity).
3. Dark Image: we turn off everything but the residual light in order to get the noise value for the camera.

For each image, we associate a corresponding intensity: I_{atoms} for the first, I_{probe} for the second, and I_{dark} for the third. A program developed in LabVIEW by the group itself then analyzes the captured images, transforming the values related to the optical density of each pixel into a matrix. Mathematically, what we have is:

$$I_{final} = \frac{I_{atoms} - I_{dark}}{I_{probe} - I_{dark}}$$

Where I_{final} is the final intensity of the beam, carrying the information related to the atomic cloud. The information we can grasp from the absorption imaging process can be plenty, such as number of atoms trapped (with that we can know the spatial density of our cloud), cloud position (it helps with possible alignment issues, for instance), cloud size (also alignment) and something called Optical Density (OD), let's focus on the latter for a bit.

When you shine a resonant laser through an atomic cloud, part of the laser intensity is absorbed. The cloud ends up creating a shadow of itself into the laser and what we capture is an image of such shadow. Now, intuitively, we can say that the higher the number of atoms, the *shadowier* the image will be (as long as the cloud size remains the same). This feature is what Optical Density is: the characteristic of how *shadowier* the cloud's shadow in the image you capture can be. That can be equated by the Beer-Lambert law:

$$I(\vec{r}) = I_0 e^{-\sigma \int n(x,y,z)dx} \tag{2.12}$$

$I(\vec{r})$ is the laser intensity that travels in the x axis, I_0 its intensity before going through the cloud, σ the cross-section of one atom when considering the low light intensity limit (which can be

interpreted as the shadow area that an atom creates at the laser) and $n(x, y, z)$ the cloud spatial density.

At equation 2.12, the terms on the exponential (besides the minus signal) are the OD, where we conclude: OD $= \sigma \int n(x, y, z)dx$. Now, keep in mind that the OD thus holds information about the spatial density of the atomic cloud (and therefore its number of atoms) but also has an effect on the beam intensity (where the greater the OD, the lower the beam intensity after passing through the cloud is). Since the absorption imaging process relies on capturing the shadow on that beam, we also need a relevant amount of its power to reach our CCD camera, which means that if we get an abnormally high OD (higher than 1 at our case), the information that we can withdraw from our image is misleading since such image is saturated, which yields miscalculations of specific values. That can be fixed by the use of something known as Time of Flight (ToF)

The ToF is the time interval between the moment we turn off the components used for capturing the atoms and the moment the first shot is made. The higher the ToF, higher will be the free fall of the atomic cloud, meaning that if we consider a typical Maxwell-Boltmann distribution, that has as a consequence an isotropic gaussian density distribution, then the size of the cloud (along with its density and therefore its optical density) will shift in value. The cloud size ($\sigma_{y,z}$) can be estimated as:

$$\sigma_{y,z}^2 = v_{rms,y,z}^2 t_{ToF}^2 \tag{2.13}$$

where $v_{rms,y,z}^2$ is the quadratic mean velocity in each of the axis that form the image (y and z, as for x is the axis the beam is travelling) and t_{ToF} is the time interval known as Time of Flight (ToF).

This is how we experimentally control our atomic cloud in order to measure parameters of it without misleading or fake values. This is important since we can only rightfully calculate and measure the fringes intensity with the correct values of number of atoms and cloud's size for instance. At Figure 2.6 you can see an example of one of our clouds with different time of flights.

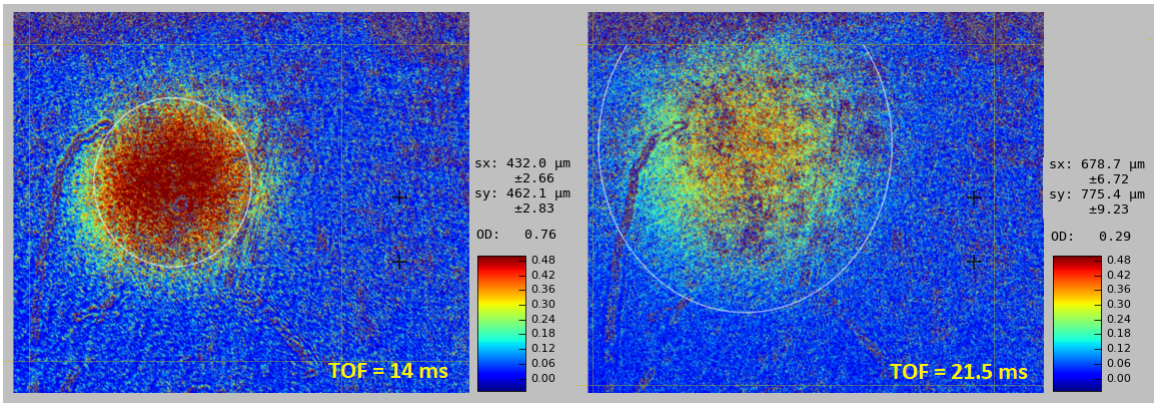

Figure 2.6: RedMOT with different TOFs and how that affects some characteristics of the cloud. While the number of atoms changed a bit, 9.6E6 on the left while 9.1E6 on the right, this can be considered as just a normal fluctuation between shots of the cloud. The relevant parameters changed with the TOF are the ones represented: i) the mean size went from ≈ 450 µm with 14 ms to ≈ 700 µm with 21.5 ms of TOF, and ii) the OD went from 0.8 to 0.3. While 0.8 may seem not saturated, the less chance of that happening, the better.

Source: author

Green System

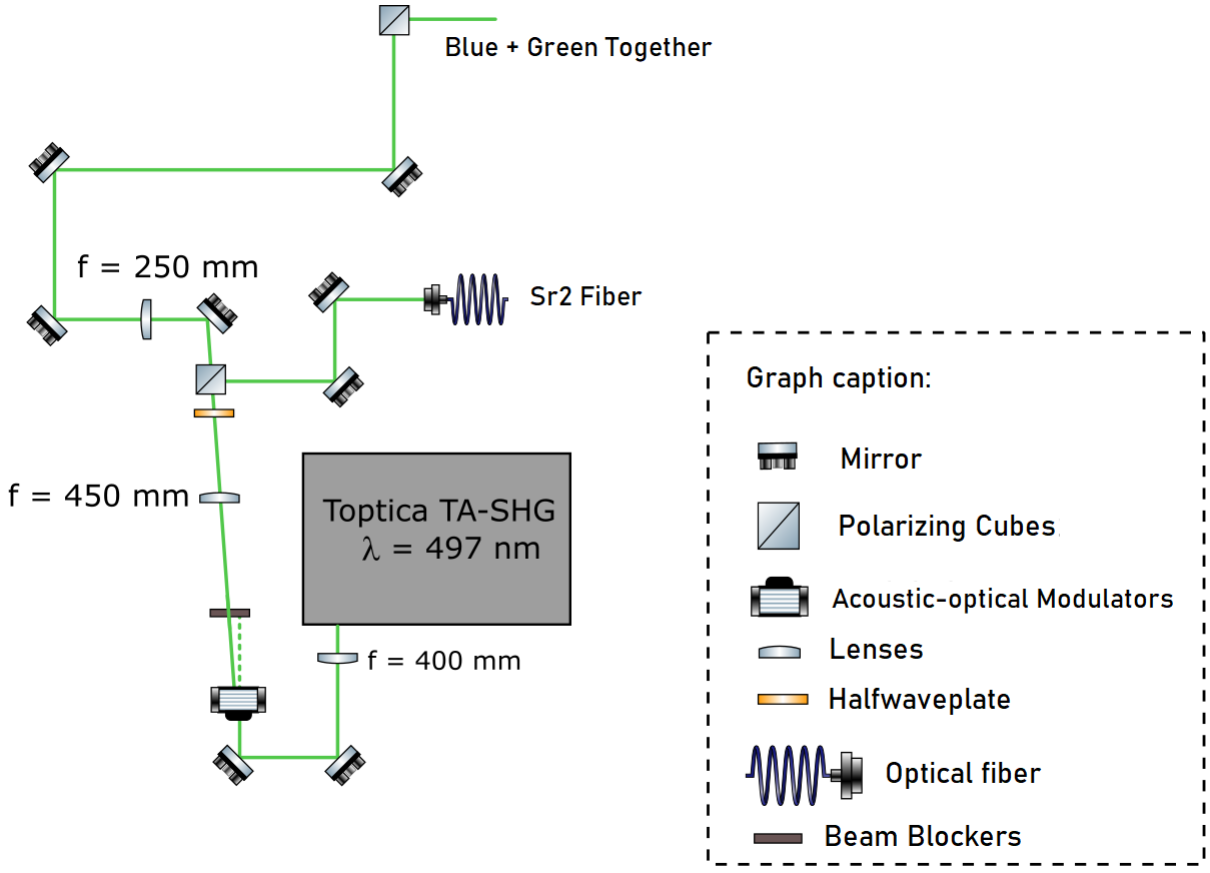

Figure 2.7: Simplified schematic of the green laser system.

Source: author.

Just as the Blue System, the Green is also created using the commercially available frequency-doubled laser diode TA-SHG Pro model from Toptica Photonics, providing a laser beam with a final wavelength of 497 nm, which is used for the repump process.

It is crucial to note that, for the BlueMOT, the transition occurs between $[5s^2]^1S_0$ $[5s5p]^1P_1$, and at a rate of 1 in every 50000 transitions, there is a decay to the $[5s4d]^1D_2$ state, followed by transitions to the $[5s5p]^3P_J$ states. The state with magnetic moment $J = 2$ is a meta-stable state, meaning it has a long lifetime (approximately 1000 s); furthermore, while the atom is in this state, it is not affected by the optical force governing the MOT. Considering that the trapping region of the cloud is defined by the size of the BlueMOT beam, with a diameter of ≈ 2 cm, and atoms in this cloud are at a temperature of 10 mK, we can calculate the time it takes for an atom to traverse this region: approximately 12 ms. This duration is more than enough for an atom in the $J = 2$ state to exit the MOT region and, therefore, avoid being trapped.

To address this issue, we employ the green transition (497 nm), pumping the atoms to the $[5s5d]^3D_2$ state. From there, atoms can decay to the $[5s5p]^3P_1$ state, returning to the ground state and thereby achieving cooling. However, there is also the possibility of atoms decaying to the $[5s5p]^3P_2$ and $[5s5p]^3P_0$ states. For atoms that decay to the state with magnetic moment $J = 2$, re-pumping occurs, exciting them back to the $[5s5d]^3D_2$ state until eventually decaying to the $J = 1$ state, completing the cooling cycle. On the other hand, atoms that decay to the $J = 0$ state, which is also a meta-stable state due to its long lifetime, do not undergo re-pumping and are thus unable to complete their cooling cycle, remaining untrapped. The proportion of atoms that fall into this level is less than 0.1 %, demonstrating that despite the imperfect re-pumping scheme, it exhibits high efficiency in the experiment. [28]

Red System

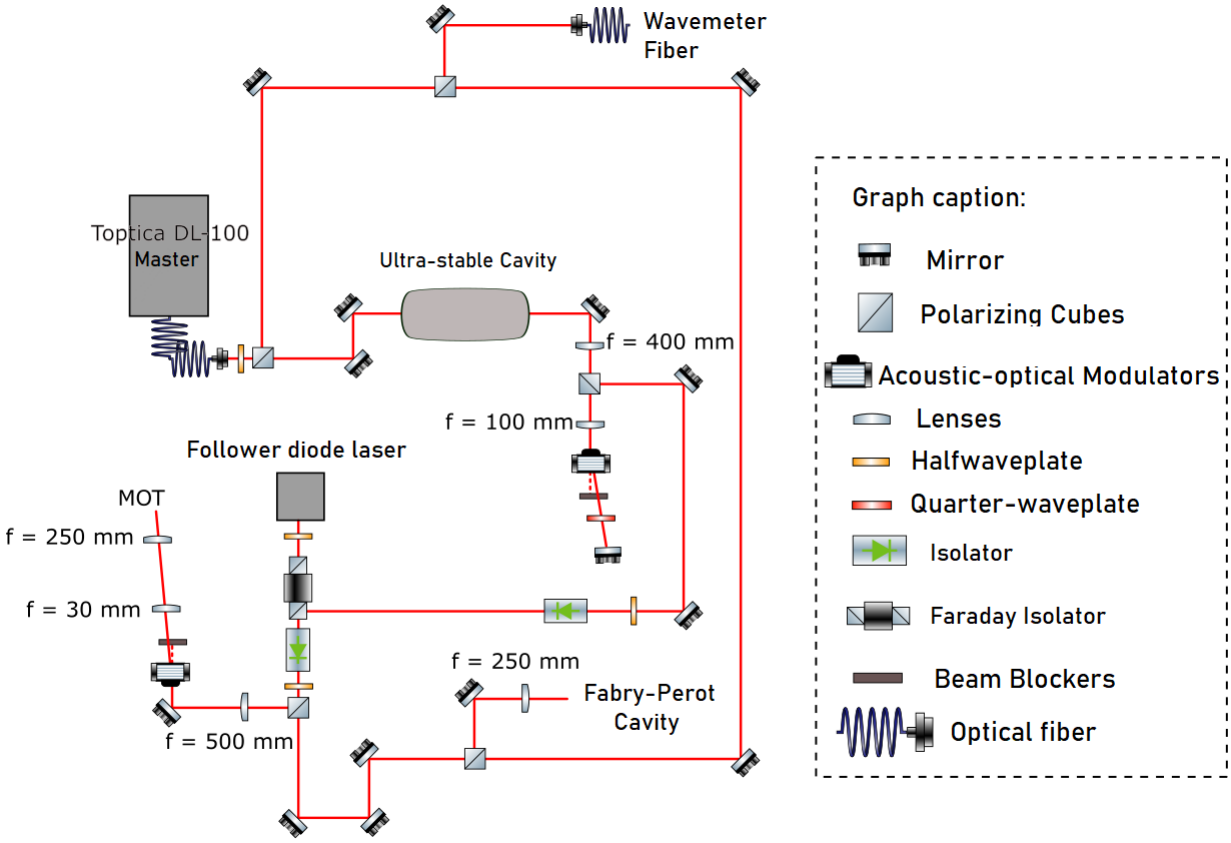

Figure 2.8: Simplified schematic of the red laser system.

Source: author.

Being a more intricate system, it adopts a master-follower configuration. In this setup, a follower laser with high power, albeit accompanied by high noise, has its frequency controlled by another laser denoted the master, which maintains a low noise level. Frequency stabilization is achieved through a technique known as injection locking [29]. This technique ensures that the follower laser operates precisely at the injected frequency with low noise [26]. Consequently, the final frequency of the red system remains stable when compared to the natural linewidth of its respective transition, which is 7.6 kHz, provided that the master laser frequency remains stable as well.

For the construction of the red laser system we employ the commercial diode DL 100 pro model, also from Toptica Photonics, as the master laser.Additionally, for the follower, a diode laser within a temperature stabilization system, designed by the research group itself, is utilized. At our experiment, the Red System is responsible for creating the RedMOT.

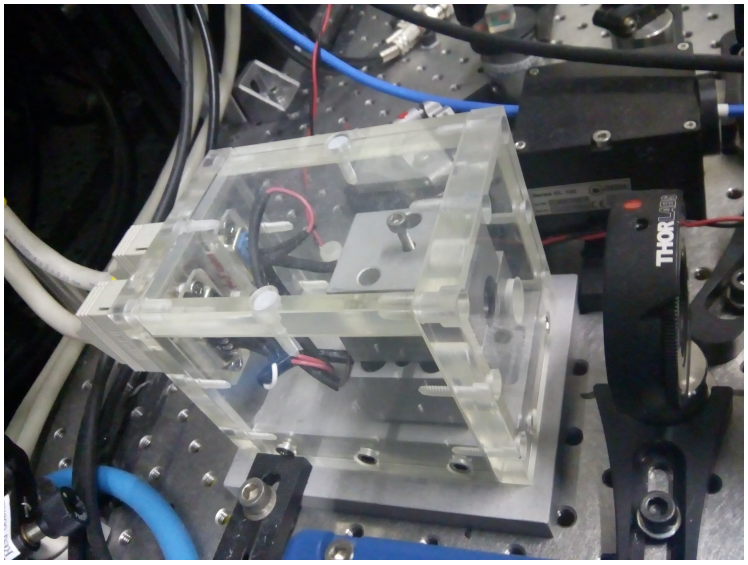

Figure 2.9: Photo of the self-built follower diode laser by the group.

Source: author.

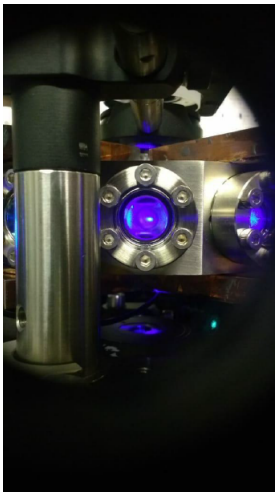

Figure 2.10: Photo of our BlueMOT seen from one of our Science Chamber windows.

Source: author

Experimental Sequence

With all the three system combined, we are able to acquire the samples used within this work. As I stated earlier, it is necessary to achieve first the BlueMOT before acquiring the RedMOT, due to the linewidth of their transition and the forces behavior. That is done through a control computer connected to a National Instruments commercial board, models MF6259 and AO6723. From it, we can operate the necessary apparatus for atom trapping using digital signals.

To efficiently trap atoms in the blue transition, a wait time of 2 s is used in order to load

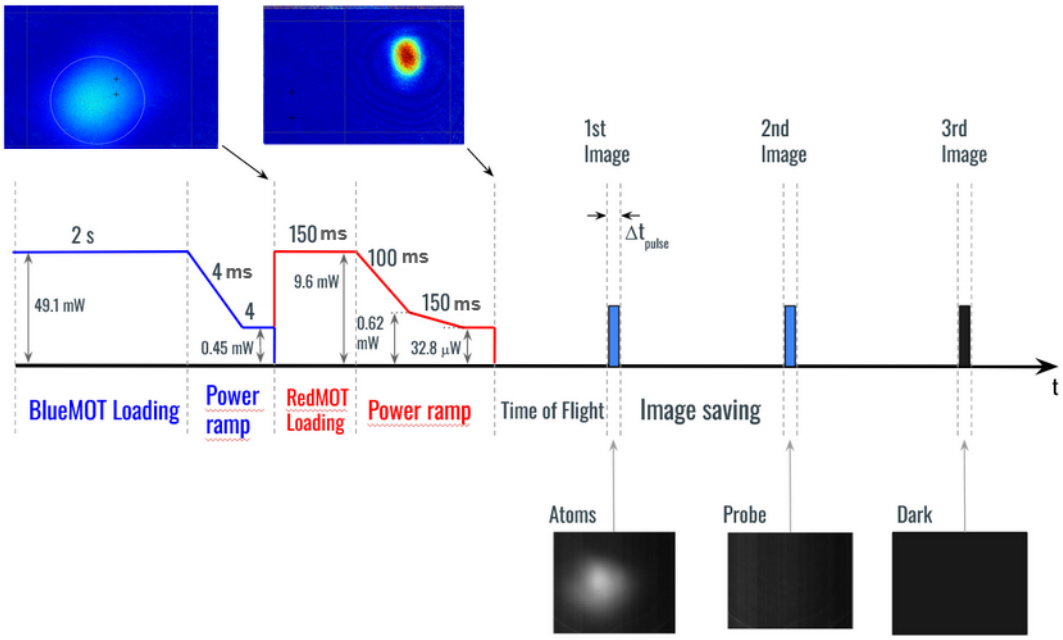

Figure 2.11: Simplified experimental sequence schematic for obtaining our absorption image, the values indicates the time and power from each step (not in scale). At the top left corner, the absorption image made from each MOT with an indication of when the imaging process would begin. At the bottom right, a visual representation of what each image would be like (they are not what the CCD really captures since it would be necessary a normalization imaging process, the shots are represented that way only for didactically purposes). Δt_{pulse} represents the pulse duration for each image.

Source: author

the BlueMOT. This time is necessary to load the experimental sequence onto the control boards from the computer. After the initial 2 s, a power ramp on the blue beam is executed over 4 ms: we configure initial and final power values for the trapping beam, gradually changing the power using software programmed in Python, developed by the group. This technique, along with another known as frequency ramping, enables further cooling of the cloud. The power and frequency values are experimentally tested and optimized for each MOT.

Figure 2.11 schematically represents, though in a simplified manner, the experimental sequence employed at our lab along with the power ramps in each laser system. Even though when captured by the BlueMOT the atoms are with way lower thermal energies, operating at values of mK, some may still be too hot to perceive the radiation pressure created by the RedMOT. For such transfer of atoms from the BlueMOT to the RedMOT be optimized, we followed the steps presented on Simon Stellmer Ph.D. thesis, *Degenerate quantum gases of strontium* [11]. There, he divided the process to obtain his RedMOT into specific stages, which we also adopted for our experiment and its specific characteristics:

1. First Stage: In this initial stage, concurrently with a frequency ramp, we perform a frequency scan that artificially broadens the transition. Initially, with respect to the resonance frequency, we detune our laser by a maximum value of -8 MHz, changing as we execute the frequency ramp, and -1.12 MHz for the minimum value. The laser frequency is scanned between these limits with a frequency of 30 kHz. This stage has a duration of 150 ms, while the beam power is maintained at 9.6 mW.

2. Second Stage: The methodology in this stage is the same as the first (ramp combined with frequency scan), but now the initial maximum value is a detuning of -6 MHz, while the minimum value remains the same at -1.12 MHz. It has a duration of 100 ms, and during this time, we also perform a power ramp, initially taking it from the value mentioned in the first stage to a final value of 0.62 mW.

3. Third Stage: In the final stage, we perform a frequency ramp (without artificially broadening the transition), starting at a detuning of -2 MHz with respect to resonance and ending at a detuning of -1.82 MHz. Simultaneously, we execute another power ramp, taking the beam from the final value of the second stage to a value of 32.8 μW. This stage has a duration of 150 ms.

In Figure 2.12, there is a schematic representation of the frequency ramps performed in all stages of the red MOT. Each MOT has its own unique characteristics, as follows:

- BlueMOT: 3×10^7 atoms, optical density equals to 0.4, sizes at $\hat{x}$ and $\hat{y}$ axis ~ 1100 μm.
- RedMOT: 8×10^6 atoms, optical density equals to 0.4, sizes at $\hat{x}$ and $\hat{y}$ axis ~ 600 μm.

At our experiment, setting up the different variables within this procedure to optimize our system, we manage to transfer 30.6% atoms from the BlueMOT onto the RedMOT. In Figure 2.13 you see an absorption image of both the clouds used for this thesis.

Each one of them have its specific pros and cons when considering the research presented here. If we consider that the RedMOT is considerably smaller when compared to the BlueMOT, then we have the upper-hand of a sample that will have a constant electric field value throughout the whole cloud, important for not having any side-effects of the light-atom interaction. On the other hand, the BlueMOT have, as seen, a way larger number of atoms, which means a way better signal to noise-ration, facilitating in obtaining the results we were looking for. How that affects such results will be explored in chapter 4, but a spoiler I can tell is that we decided to use the BlueMOT since with the bigger number of atoms, the fringes were way more visible.

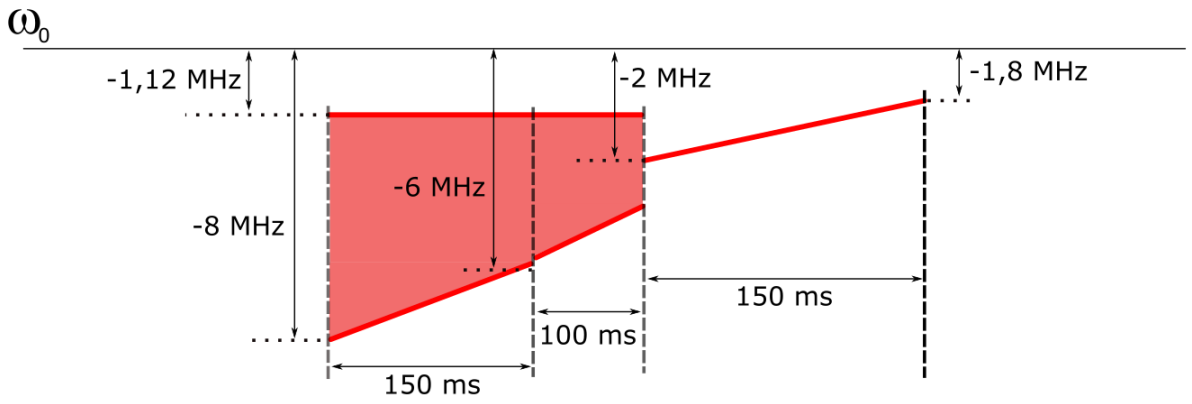

Figure 2.12: Schematic representation of the frequency ramp employed in the stages of the Red-MOT. The depicted values indicate the resonance utilized relative to the resonance frequency ω_0 of the transition. The figure also illustrates the duration of each stage. The red band means the range within which we scan the frequency in both the first and second stages.

Source: [25]

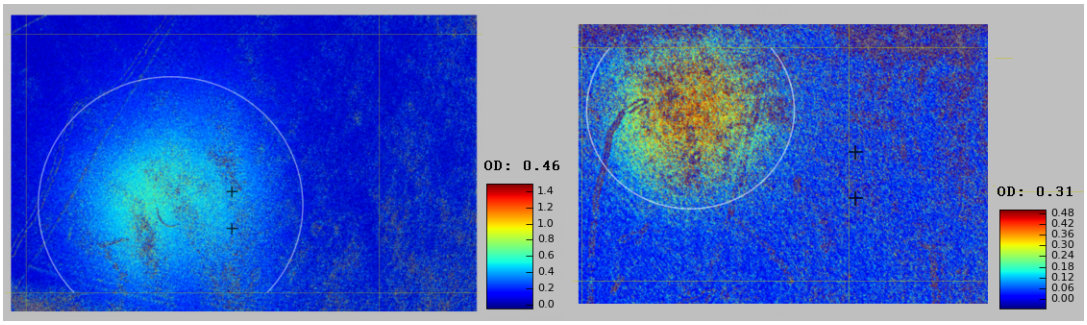

Figure 2.13: Absorption images from both our MOTS (Blue at left and Red at right). The color scheme indicates the optical density of each image. Even though it is shown here a lower OD for the RedMOT, I must clarify that this only happens since the RedMOT has a higher TOF (21.5ms against 0.8ms for the blue). As seen in figure 2.6, a RedMOT with TOF = 14 ms is enough to show a much higher optical density for this sample. This is due to the fact that the OD also takes indirectly into account the cloud's size (with the cross-section, while the BlueMOT have sizes of ≈ 1100 µm, the RedMOT have ≈ 600 µm with their respective TOF). Hence the use of TOFs to control such variable with each measure taken.

Source: author

Chapter 3

INTERFERENCE AND INTERFEROMETRY

To start the main discussion of this thesis, I'll first introduce basic concepts surrounding interference and interferometry in general. Such discussion may seem too simple at first glance but I believe it will help create a solid basis to the reader when presented our specific system and results, thus helping with the discussion. A good reference to explore and understand these basic concepts is the book *Basics of Interferometry* by P. Hariharan. Even though Hariharan gives an detailed explanation about the concepts involved, here I'll take a more direct approach, with the care of not losing any important information. What we want is to understand what information we can grasp from interferometric systems, and that means understanding what can be measured from them.

When talking about light, which can be understood as two transverse fields (one eletric and one magnetic), one can see that measuring information from light most frequently means measuring information from one of these fields. It is usual to consider only the electric field when having such discussions. That being said, a useful and simple basis for describing the electric field at a position x and a time t is composed of plane waves of the form:

$$\boldsymbol{E}(x,t) = Ae^{i(\omega t - kx)}\boldsymbol{\epsilon} \tag{3.1}$$

Here, A is a complex amplitude, $\omega = 2\pi f$ the angular frequency, $k = 2\pi/\lambda$ the wave number (f the frequency of the field and λ the wavelength) and $\boldsymbol{\epsilon}$ the light polarization.

But to measure light's electric field is not always simple. Depending on the system, a better way to investigate such value is to look into the field's intensity, given by [30]:

$$\boldsymbol{I}(x) = \frac{\varepsilon_0 c}{2} \mid \boldsymbol{E}(x,t) \mid^2 \tag{3.2}$$

where ε_0 is the vacuum permittivity and c the speed of light in vacuum.

In interference phenomena, the total intensity that can be measured is a result from the combination of the two light fields that interfere with each other. Lets calculate such intensity.

3.1 Total Intensity for two fields interference

Two fields interfering will have a resultant intensity that depends on whether or not they reinforce or cancel one another, which the reader may know from basic undulatory problems [31]. Assuming both fields propagates in opposite directions, we can describe each field as:

$$\boldsymbol{E_1}(x,t) = A_1 e^{i(\omega t - kx)}\boldsymbol{\epsilon_1} \tag{3.3a}$$
$$\boldsymbol{E_2}(x,t) = A_2 e^{i(\omega t + kx)}\boldsymbol{\epsilon_2} \tag{3.3b}$$

At equations 3.3, $A_j = a_j e^{i\phi_j}$ are the complex amplitudes of each field, with a_j a scalar and ϕ_j the field's phase, while ϵ_j are the polarization vectors. The total electric field responsible for the total intensity of the interference pattern is just the sum of both electric fields presented:

$$\boldsymbol{E_T}(x,t) = A_T e^{i\omega t} = (A_1 e^{-ikx}\boldsymbol{\epsilon_1} + A_2 e^{ikx}\boldsymbol{\epsilon_2})e^{i\omega t} \tag{3.4}$$

The total intensity is then:

$$\boldsymbol{I_T}(x) = \frac{\varepsilon_0 c}{2}|\ \boldsymbol{E_T}(x,t)\ |^2 = \frac{\varepsilon_0 c}{2} A_T^* A_T \tag{3.5}$$

But

$$\begin{aligned} A_T^* A_T &= (A_1^* e^{ikx}\boldsymbol{\epsilon_1} + A_2^* e^{-ikx}\boldsymbol{\epsilon_2})(A_1 e^{-ikx}\boldsymbol{\epsilon_1} + A_2 e^{ikx}\boldsymbol{\epsilon_2}) \\ &= (A_1^* A_1 + A_2^* A_2 \ + \ A_1^* A_2 e^{2ikx}\boldsymbol{\epsilon_1}\cdot\boldsymbol{\epsilon_2} \ + \ A_2^* A_1 e^{-2ikx}\boldsymbol{\epsilon_1}\cdot\boldsymbol{\epsilon_2}) \end{aligned} \tag{3.6}$$

Which lead us to:

$$\boldsymbol{I_T}(x) = \boldsymbol{I_1}(x) + \boldsymbol{I_2}(x) + \frac{\varepsilon_0 c}{2}(A_1^* A_2 e^{2ikx} + A_2^* A_1 e^{-2ikx})\boldsymbol{\epsilon_1}\cdot\boldsymbol{\epsilon_2} \tag{3.7}$$

If we say that $\phi = \phi_1 - \phi_2$, then the total intensity for such interference can be calculated as:

$$\boldsymbol{I_T}(x) = \boldsymbol{I_1}(x) + \boldsymbol{I_2}(x) + 2\sqrt{\boldsymbol{I_1}(x)}\sqrt{\boldsymbol{I_2}(x)}\cos(\phi - 2kx)\boldsymbol{\epsilon_1}\cdot\boldsymbol{\epsilon_2} \tag{3.8}$$

Such equation has some interesting characteristics related specially to its last term. First, that for it to make sense, then the polarization from both electric fields shouldn't be perpendicular, otherwise we would have $\boldsymbol{\epsilon_1}\cdot\boldsymbol{\epsilon_2} = 0$. Second, that looking at the phase difference, we can see that such term is always comprised between a maximum (when $\cos(\phi - 2kx) = 1$) and a minimum ($\cos(\phi - 2kx) = -1$), which leads the total intensity $\boldsymbol{I_T}(r)$ to also vary between a maximum and a minimum value. Therefore, we can say that this last term is the one responsible for the fringes pattern that arises from the interference. More than that, we now have a result from the interference phenomena that we can measure: the intensity of the fringes itself. One advantage of measuring the fringe's intensity pattern is the fact that it makes it possible to extract the contrast of such pattern.

Contrast

Let's assume both fields have the same polarization, hence $\boldsymbol{\epsilon_1} \cdot \boldsymbol{\epsilon_2} = 1$. If we define the maximum and minimum intensities as:

$$\boldsymbol{I_{max}}(x) = \boldsymbol{I_1}(x) + \boldsymbol{I_2}(x) + 2\sqrt{\boldsymbol{I_1}(x)}\sqrt{\boldsymbol{I_2}(x)} \tag{3.9a}$$

$$\boldsymbol{I_{min}}(x) = \boldsymbol{I_1}(x) + \boldsymbol{I_2}(x) - 2\sqrt{\boldsymbol{I_1}(x)}\sqrt{\boldsymbol{I_2}(x)} \tag{3.9b}$$

Then we may define the observable known as contrast $\mathcal{C}$ (or fringe's visibility) as:

$$\mathcal{C} = \frac{\boldsymbol{I_{max}}(x) - \boldsymbol{I_{min}}(x)}{\boldsymbol{I_{max}}(x) + \boldsymbol{I_{min}}(x)} \tag{3.10}$$

That is, the ratio between the amplitude of the fringes and the sum of the powers of the individual waves involved in interference, providing a measure of how well-defined and noticeable the alternating bright and dark regions are in relation to the overall intensity of the interference. To perform this measurement at our case, for instance, we take photos of the fringes and can afterwards calculate its contrast by the equations that govern our specific system and their own characteristics (I'll discuss more about that in chapter 4).

3.2 Michelson Interferometer

Being a common setup to explain interference in general, the Michelson Interferometer is one of the earliest generations of interferometers, along with the also famous Young's Double-Slit experiment. While in the latter the british polymath wanted (and succeeded) to demonstrate light's wave behavior due to interference created by two subsequent waves created by one initial plane wave after going through the slits, the experiment developed by the prussian physicist helped with the goal to investigate the medium in which the physicists of the time believed the light needed to propagate: aether.

Despite having actually proven the opposite, the Michelson Interferometer is still a great tool to understand interference in a practical way, along with having quite relevant results to modern physics as stated in my introduction. Here, I'll use it as the great tool that it is. So far, I have explained the intensity profile that rises from the interference phenomena and the observable we can use to measure it. But I haven't explained how such interference can be created to start with. We need two electric fields interfering with each other and the experimental setup provided by a Michelson Interferometer can provide that.

It consists of one coherent light source (I'll explore more of that in a bit, for now, understand that coherence is a light property that describes how well-defined is the phase difference between the electric field at different positions and instants) that sends a light beam through a 50/50

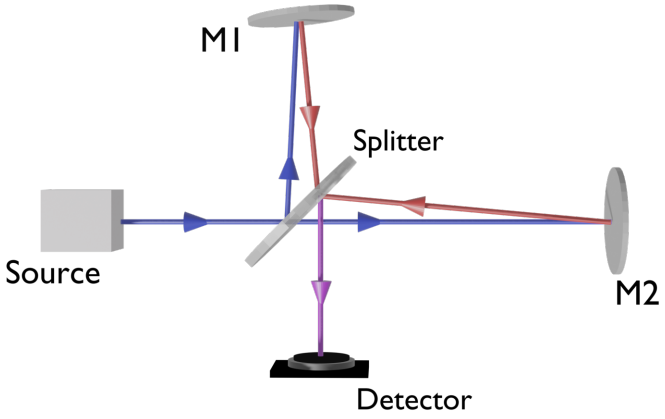

Figure 3.1: Schematics of a Michelson Interferometer setup. The light source probes a coherent beam that passes through a 50/50 splitter, having equal chances to go to mirror 1 (M1) or mirror 2 (M2). After being reflected by each mirror (reflected beams represented by color red, while blue represent the incoming ones), the beams are recombined (purple) and reflected once again into the detector. Depending on the phase difference, the detector may see different kind of fringes.

Source: author

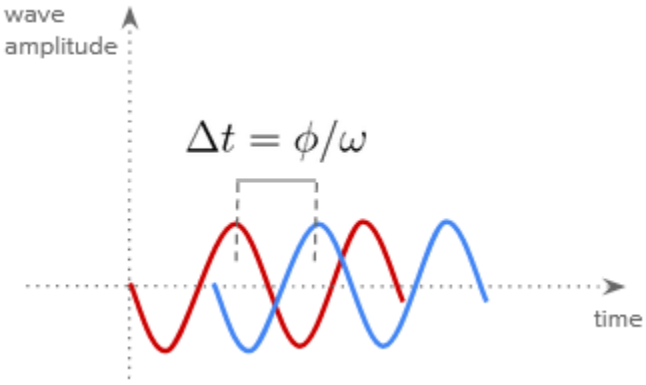

Figure 3.2: Illustration of a phase difference ϕ between two identical waves.

splitter. After going through such splitter, the beam can travel both paths reaching either mirror 1 or mirror 2 (see Figure 3.1), which in turn reflect the beam towards the splitter again. The last stage is the recombination of both beams into one, creating at the detector the appearance of fringes (or lack of).

This is due to constructive and destructive interference. As I stated before, the fringes obey an intensity profile given by equation 3.8, and the destructive or constructive behavior comes from the phase difference term $\cos(\phi - kx)$ (given that since the light source is the same, and

none of the components in the experiment alters the beam polarization, we may assume that $\boldsymbol{\epsilon_1} \cdot \boldsymbol{\epsilon_2} = 1$ as discussed in the contrast subsection). What the phase difference ϕ represents is easily illustrated by figure 3.2. Note that, considering the two waves identical, constructive and destructive interference appears as ϕ values changes. Due to their cosine behavior, it is possible to conclude that the behavior of ϕ is periodic, with its values obeying:

$$\phi = 2\pi m \tag{3.11}$$

Therefore, constructive (destructive) interference appears when the real number m is an even (odd). However, what causes the appearance of this phase difference? Keeping that both waves are identical, any change in the phase of one relative to the other implies that it has traveled a path of different length compared to the other. It is possible to relate the phase difference ϕ to this path difference Δd through [32]:

$$\phi = \frac{2\pi}{\lambda}\Delta d \tag{3.12}$$

Where now we may relate both equations to find the condition for constructive interference:

$$\Delta d = m\lambda \tag{3.13}$$

If we define $\Delta d = 2d_1 - 2d_2$, where d_1 is the path length of the splitter reflected beam and d_2 the length of the splitter transmitted one, then these equations shows the dependence of the position of maxima and minima of the interference pattern on the relative phase acquired by the light when propagating through the two interfering paths. Historically, this was used to show that the speed of light was not a function of any absolute referential such as stated by the aether hypothesis (in the calculations shown here, we assumed it implicitly, since we considered that the wavelength of monochromatic light was the same for any propagation direction). This means that the interference pattern of the Michelson interferometer can be used to measure small path differences between the arms, just as the one responsible for the measurement of gravitational waves [8] cited in the introduction of this text, for example.

Now, for all that to be true, an important concept needs to be reminded: I stated that our Michelson Interferometer has a coherent light source. Mathematically, that means that the phase difference ϕ must be a well-defined observable. But what happens if, by any reason, the value of ϕ begins to vary over time? That's what I'll explore in the next section, since to understand what ϕ being constant means we need to comprehend the actual meaning of coherence. Let's dive a bit more into such a concept.

3.3 Coherence

In the previous section, I have defined coherence as a light property that describes how well-defined is the phase difference between the electric field at different positions and instants [33]. Hariharan in his book, stated a bit differently: *"Coherence theory is a statistical description of the radiation field due to a light source, in terms of the correlation between the vibrations at different points in the field."* [34]. In this context, when investigating the coherence of your light field, what you want is to study its behavior (the vibrations mentioned by Hariharan) either over time or over specific positions (the points in the field, since they can change due to time passing or due to which position you consider your point). That means investigating how the phase difference Φ may vary not only over time, but also over the spacial position you consider your wave to be in. The consequence of this statement is that, now, we have two different types of coherence: temporal coherence and spatial coherence, and a field can be temporally coherent without being spatially coherent, and vice-versa.

Temporal Coherence

Temporal coherence happens when our field maintains a well defined relative phase over a period of time. It describes how well the wave maintains a constant phase relationship as it evolves, where high temporal coherence indicates that the wave maintains a consistent phase over a long period, while low temporal coherence means that the phase relationship is changing rapidly. A practical way to understand this concept is to imagine the phase difference (Φ), as illustrated in Figure 3.2, situated over two fixed points on the same wave along the time axis. The more constant Φ value remains, the greater the temporal coherence in our field. Essentially, temporal coherence provides insights into the monochromatic nature of the light source.

Spatial Coherence

Spatial coherence, on the other hand, happens when our field also maintains a well defined relative phase, but now over a specified transverse distance. In this context, spatial coherence characterizes how consistently the wavefronts of the same wave at distinct locations maintain a constant phase relationship. A high degree of spatial coherence indicates a strong correlation among wavefronts, meaning a consistent phase relationship across space. In simpler terms would it be as if we replaced the time axis in figure 3.2 with a spatial axis. Analogously, the longer Φ value stays constant, the more spatially coherent our field is.

It is possible to relate both of these concepts through basic physics. For instance, imagine a point source producing a single wave that travels through time with constant amplitude, but with a not perfectly defined frequency. This induces a broadening of the statistical distribution of the relative phase, that increases over time; when the phase broadening reaches 2π, the coherence is greatly reduced, which lead to define a Coherence Time (τ_c) given by the time it takes for the phase

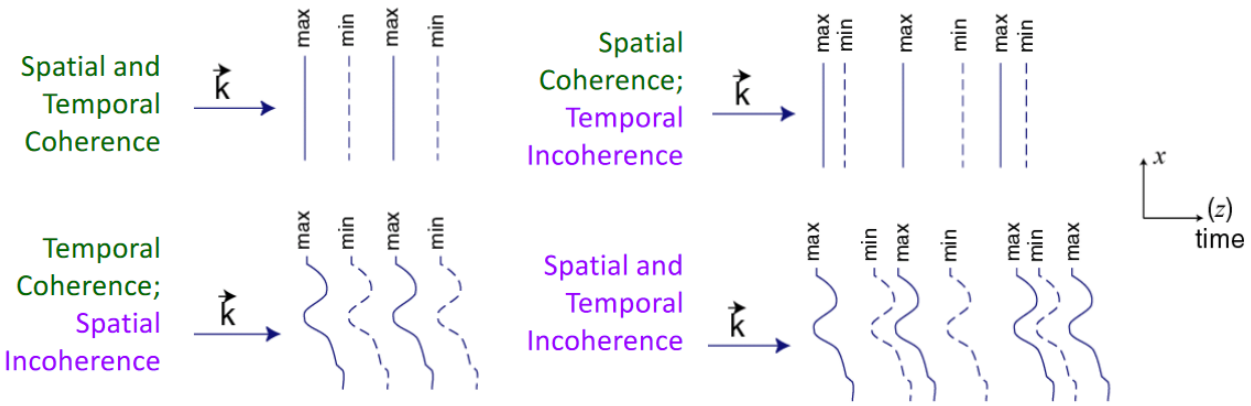

Figure 3.3: Different specifications of temporal and spatial coherence, along with their combination showing how a wave can be temporally coherent, spatially coherent, neither or both.

Source: [35]

broadening to reach 2π. Because of this definition, it is also common to often refer to another value called Coherence Length ($L_c = c\ \tau_c$). The longer the coherence time τ_c is, the more temporally coherent is the light source. While the longer L_c is, the more spatially coherent it will be.

For a practical example, imagine a Michelson interferometer just as figure 3.1. Initially, you have both mirrors $M1$ and $M2$ at the same distance l from the splitter. But, if a distance d is added in one of the paths, then that would mean light would take different times to travel each path. The finite coherence length of light means that now the contrast of the interfering path is a function of d, with maximum contrast for $d = 0$ and $C \to 0$ for $d \to \infty$, with typical length scale L_c for this contrast reduction. However, this may lead to a wrong assumption: that both concepts (spatial and temporal coherence) are always related. The reader must recall that a field can be temporally coherent without being spatially coherent. Figure 3.3 illustrates this idea, giving a good example over the different possible configurations a field may present when talking about coherence.

3.4 Correlation Function

Per definition, a correlation function is a mathematical expression that quantifies the statistical correlation, or coherence, among random variables based on their spatial or temporal separation. At our specific case, this means being a tool to measure how coherent (either temporal or spatial) our field is. There are different orders if one desires to investigate this function, and while the second order correlation may verify and give rise to phenomenons such as light bunching and antibunching [36] at the same time that superior orders also exists, within this work I'll focus only on the first order, due to its simplicity and relevance to the interference phenomena in general, and in particular to the one I'll present later on at the text.

First Order Correlation Function

The first order correlation function would, as the definition before, quantify a correlation of the electric field at two different times. Picturing yet again the Michelson Interferometer, it is useful to imagine as if a field reaching mirror $M1$ would take a time t to travel that path, while for mirror $M2$, the field would take a time $t' = t + \tau$, where τ is the time delay between the two paths. Thus, the correlation function then quantify the degree of coherence between the electrical field for $M1$, $E(t)$, and the one for $M2$, $E(t')$. In order to do that, we investigate the interference between these two fields. Hence, we calculate the intensity pattern of this interference just as done for equation 3.8. To evaluate the average interference pattern of the waves at a fixed time delay τ, we need to average (denoted by $\langle\rangle$) such process over all possible values of t:

$$\langle I(t,\tau)\rangle = \frac{\varepsilon_0 c}{2}|\mathcal{R}|^2\ |\mathcal{T}|^2\Big\{\langle|E(t)|^2\rangle + \langle|E(t')|^2\rangle + 2\mathrm{Re}[\langle E^*(t)E(t')\rangle]\Big\} \tag{3.14}$$

Here, $\mathcal{R}$ and $\mathcal{T}$ are the coefficients related to the reflection and transmission of the splitter that satisfies $|\mathcal{R}|^2 + |\mathcal{T}|^2 = 1$ and $\mathcal{R}\mathcal{T}^* + \mathcal{T}\mathcal{R}^* = 0$.

This averaging, in turn, is the same as if we perform an statistical averaging for stationary light sources; i.e., this problem may be addressed as having a stationary distribution, where its statistical properties, including the correlation function, remain constant over time. Now, notice how equation 3.14 (just as the one obtained at equation 3.8) is composed of three terms: while the first two represents the intensities of each path separated and do not contribute to the interference pattern, the third not only do contribute to it but also involves the main goal of this section, the correlation function. It can be defined as [37]:

$$\langle E(t)^* E(t')\rangle = \frac{1}{T}\int_T E(t)^* E(t')dt \tag{3.15}$$

At this equation, the variable T is the observation period of our system. Since we are looking at it from a stationary perspective, we may conclude that this correlation function does not depend neither from t nor t', but actually from the delay between them, τ. Matching both this information, we may define the observation period as the delay between the two fields and rewrite equation 3.15 as:

$$\langle E(t)^* E(t+\tau)\rangle = \frac{1}{T}\int_T E(t)^* E(t+\tau)dt \tag{3.16}$$

From equation 3.16, it is possible to write the spectral density S of this interference profile over the frequency domain, obtaining [37]:

$$S(\omega) = \frac{1}{2\pi}\int_{-\infty}^{\infty}\langle E^*(t)E(t+\tau)\rangle e^{i\omega\tau}d\tau \tag{3.17}$$

However, we may also rewrite equation 3.16 if we consider the Cauchy-Schwarz inequality:

$$|\langle E(t)^* E(t+\tau)\rangle|^2 \leq |\langle E(t)\rangle|\ |\langle E(t+\tau)\rangle| \tag{3.18}$$

Since we are considering that $E(t)$ is stationary over time t, its modulus is constant in any time instant, hence $|\langle E(t)\rangle| = |\langle E(t+\tau)\rangle|$. And since we the only dependence is, yet again, over τ, it is possible to state that the real part of this first order correlation function is the same whether we have a positive or negative value of τ:

$$\langle E^*(t)E(t-\tau)\rangle = \langle E^*(t+\tau)E(t)\rangle = \langle E^*(t)E(t+\tau)\rangle \tag{3.19}$$

Thus, a normalized correlation function with respect to the stationary electric field $E(t)$ may be defined as:

$$g^{(1)}(\tau) = \frac{\langle E^*(t)E(t+\tau)\rangle}{\langle E^*(t)E(t)\rangle} \tag{3.20}$$

Which also allow us to write an intensity profile with respect to the correlation function $g^{(1)}(\tau)$:

$$\langle I(t)\rangle = \frac{\varepsilon_0 c}{2}|\mathcal{R}|^2\ |\mathcal{T}|^2\Big\{2\langle|E(t)|^2\rangle + 2\langle|E(t)|^2\rangle \mathrm{Re}[g^{(1)}(\tau)]\Big\} \tag{3.21}$$

Or, as Hariharan states in his book [34]:

$$I(t) = I_1 + I_2 + 2\sqrt{I_1 I_2}\mathrm{Re}[g^{(1)}(\tau)] \tag{3.22}$$

This brings an important concept to the surface: the relation between the interference profile of our fringes and the first order correlation function. Because of this relation, it is possible to write [33]:

$$\mathcal{C} = \frac{I_{max}(t) - I_{min}(t)}{I_{max}(t) + I_{min}(t)} = \frac{2\sqrt{I_1(t)I_2(t)}}{I_1(t) + I_2(t)}|g^{(1)}(\tau)| \tag{3.23}$$

Which means that if both intensities are the same (as the case of our experiment, for instance, due to both fields come from the same laser beam, meaning they have approximately the same intensity), then the contrast $\mathcal{C}$ is a direct measurement of your field's coherence through the first order correlation function $g^{(1)}(\tau)$. On a final note concerning this approach, it is also possible to write a normalized spectral density function with relation to $g^{(1)}$:

$$S_{norm}(\omega) = \frac{1}{2\pi}\int_{-\infty}^{\infty} g^{(1)}(\tau)e^{i\omega\tau}d\tau = \frac{1}{\pi}\int_{0}^{\infty} g^{(1)}(\tau)e^{i\omega\tau}d\tau \tag{3.24}$$

since $g^{(1)}(\tau) = g^{*(1)}(\tau)$.

First Order Correlation - Quantum approach

In the previous subsection, the development of the first order correlation function was given in a classical approach, but it is also possible to find such relation in a fully quantum approach. At our system, the goal is to acquire information provided by the light scattered by the atoms. This means that in order to consider this scattered light, the interaction between the electrical field and the atom is relevant, which will be what I aim to explain within this subsection. To achieve that, a quantum approach is best suited, where the atom, being a quantum object, makes the light scattered by it inherit its quantum properties. Within the quantum context we then have new tools used to describe such interaction with the electromagnetic field [24]:

$$\hat{n}|n\rangle = n|n\rangle \tag{3.25a}$$
$$\hat{a}^{\dagger}|n\rangle = \sqrt{n+1}|n+1\rangle \tag{3.25b}$$
$$\hat{a}|n\rangle = \sqrt{n}|n-1\rangle \tag{3.25c}$$
$$\tag{3.25d}$$

At these equations, the reader may understand the following concepts:

- $|n\rangle$ are the possible states of the field, related to a specific n quantity of photons.
- $\hat{a}$ is the annihilation operator, which describes the loss of a photon, bringing your field to a state of lower energy.
- $\hat{a}^{\dagger}$ is its complex conjugate, known as creation operation, which brings the field to a state of higher energy.

The number operator, $\hat{n} = \hat{a}^{\dagger}\hat{a}$, help describe the dynamic of the system, where it is possible to find through Heisenberg representation the following expression [24]:

$$\mathrm{E}_n = \left(n + \frac{1}{2}\right)\hbar\omega_{field} \tag{3.26}$$

where E_n is the energy of the nth state and ω_{field} the frequency of the field.

This expression of energy then show us that each photon emitted by the system actually carry with itself a specific quantity of energy related to the value $\hbar\omega_{field}$. Just as in the classical

approach, the goal is to find a correlation function $g^{(1)} \propto E(t)$. Though, due to the quantum nature of the current approach, the electric field operator is more suited. Considering the operators just mentioned, it is possible to write the electric field operator as:

$$\hat{\boldsymbol{E}}(r,t) = i\sum_{\boldsymbol{k},j}\left(\frac{\hbar\omega_k}{2\varepsilon_0 V}\right)^{1/2}\epsilon_{\boldsymbol{k},j}\left[\hat{a}_{\boldsymbol{k},j}e^{i(\boldsymbol{k}\cdot\boldsymbol{r}-\omega_k t)} - \hat{a}^{\dagger}_{\boldsymbol{k},j}e^{-i(\boldsymbol{k}\cdot\boldsymbol{r}-\omega_k t)}\right] = \hat{\boldsymbol{E}}^{(+)} + \hat{\boldsymbol{E}}^{(-)} \tag{3.27}$$

here, $\boldsymbol{k}$ represents the wavevector of each mode of electromagnetic radiation, j the possible polarizations the polarization vector ϵ may assume, V the quantization volume, ω_k the frequency of the mode $\boldsymbol{k}$.

Thus, it is safe to say that the electric field can be described as the sum of two parts: one related to the annihilation operator ($\hat{\boldsymbol{E}}^{(+)}$), and the other to the creation operator ($\hat{\boldsymbol{E}}^{(-)}$). If we consider only one possible polarization for our field, we may then rewrite these terms as the following:

$$\hat{\boldsymbol{E}}^{(+)}(\boldsymbol{r},t) \approx i\sum_{\boldsymbol{k}}\left(\frac{\hbar\omega_k}{2\varepsilon_0 V}\right)^{1/2}\hat{a}_{\boldsymbol{k}}e^{i(\boldsymbol{k}\cdot\boldsymbol{r}-\omega_k t)}\epsilon_{\boldsymbol{k}} \tag{3.28a}$$

$$\hat{\boldsymbol{E}}^{(-)}(\boldsymbol{r},t) \approx -i\sum_{\boldsymbol{k}}\left(\frac{\hbar\omega_k}{2\varepsilon_0 V}\right)^{1/2}\hat{a}^{\dagger}_{\boldsymbol{k}}e^{-i(\boldsymbol{k}\cdot\boldsymbol{r}-\omega_k t)}\epsilon_{\boldsymbol{k}} \tag{3.28b}$$

Yet, if we also consider that we are dealing with only one mode of electromagnetic radiation as, for example, when the light detector detects only one specific light mode of frequency ω_l, a new operator defined as $\hat{\boldsymbol{E}}^{(-)}(\boldsymbol{r},t)\hat{\boldsymbol{E}}^{(+)}(\boldsymbol{r},t)$ can be written:

$$\hat{\boldsymbol{E}}^{(-)}(\boldsymbol{r},t)\hat{\boldsymbol{E}}^{(+)}(\boldsymbol{r},t) \approx \left[-i\left(\frac{\hbar\omega_l}{2\varepsilon_0 V}\right)^{1/2}\hat{a}^{\dagger}e^{-i(kr-\omega_l t)}\right]\left[i\left(\frac{\hbar\omega_l}{2\varepsilon_0 V}\right)^{1/2}\hat{a}e^{i(kr-\omega_l t)}\right] = \frac{\hbar\omega_l}{2\varepsilon_0 V}\hat{a}^{\dagger}\hat{a} = \frac{\hbar\omega_l}{2\varepsilon_0 V}\hat{n} \tag{3.29}$$

where $\epsilon_{\boldsymbol{k}}\cdot\epsilon_{\boldsymbol{k}} = 1$ was used.

It is worth to notice that this new operator retains a dependence on the number operator $\hat{n}$, which is related to the specific states the field must be in. To a more realistic approach, the electromagnetic field may actually not be in a pure initial state $|i\rangle$, for example, but in a superposition of different states. This is better described by the density matrix $\hat{\rho}$ and the transition probability P, given by:

$$\mathrm{P} = \langle i|\hat{\boldsymbol{E}}^{(-)}(\boldsymbol{r},t)\hat{\boldsymbol{E}}^{(+)}(\boldsymbol{r},t)|i\rangle \tag{3.30a}$$

$$\hat{\rho} = \sum_i p_i|i\rangle\langle i| \tag{3.30b}$$

Because of that, we must consider a weighted sum over all possible field states given by the density matrix, meaning:

$$\sum_i \mathrm{P}_i p_i = \sum_i p_i \langle i|\hat{\boldsymbol{E}}^{(-)}(\boldsymbol{r},t)\hat{\boldsymbol{E}}^{(+)}(\boldsymbol{r},t)|i\rangle = \sum_i p_i \mathrm{Tr}\Big\{|i\rangle\langle i|\hat{\boldsymbol{E}}^{(-)}(\boldsymbol{r},t)\hat{\boldsymbol{E}}^{(+)}(\boldsymbol{r},t)\Big\}$$
$$= \mathrm{Tr}\Big\{\sum_i p_i|i\rangle\langle i|\hat{\boldsymbol{E}}^{(-)}(\boldsymbol{r},t)\hat{\boldsymbol{E}}^{(+)}(\boldsymbol{r},t)\Big\} = \mathrm{Tr}\Big\{\hat{\rho}\hat{\boldsymbol{E}}^{(-)}(\boldsymbol{r},t)\hat{\boldsymbol{E}}^{(+)}(\boldsymbol{r},t)\Big\} = G(\boldsymbol{r},t) \quad (3.31)$$

We now have a function $G(\boldsymbol{r},t)$ that is related to the electric field operators, which also allow us to obtain a correlation function in this quantum approach:

$$g^{(1)}(\tau) = \frac{G(t,t+\tau)}{G(t)} = \frac{Tr\Big\{\hat{\rho}\hat{\boldsymbol{E}}^{(-)}(t)\hat{\boldsymbol{E}}^{(+)}(t+\tau)\Big\}}{Tr\Big\{\hat{\rho}\hat{\boldsymbol{E}}^{(-)}(t)\hat{\boldsymbol{E}}^{(+)}(t)\Big\}} \quad (3.32)$$

3.5 Elastic and inelastic Scattering

When talking about light scattering, two fundamental types govern this phenomenon: inelastic and elastic scattering. The distinguishing factor between these two lies in the alteration, or lack of, of the scattered photon's wavelength. In the case of inelastic scattering, the scattered photon undergoes a wavelength change, meaning a transformation in its energy state. This alteration in wavelength can be attributed to interactions with the scattering medium (our atomic cloud, for instance), such as excitation of electrons or other energy transfer processes. On the other hand, elastic scattering is characterized by the preservation of the original wavelength of the scattered photon. Throughout the elastic scattering process, there is no net exchange of energy between the incident and scattered photons.

Because of this difference, knowing the type of scattering that happens in each system is relevant in order to comprehend the data the reader aims to acquire. If we consider the case of an inelastic scattering system, such as the one I present within this work, we may see that changes in the wavelength of the scattered photon can introduce complexities in the interference pattern of said system, affecting its coherence and influencing the overall characteristics of the scattered light. As I intend to demonstrate during this section, the correlation function can also be described as a sum of an elastic and inelastic terms.

Operators of an Atomic System

Before finding the said expression for the correlation function, it is worth to cite the atomic operators that govern the system in hand. Considering Heisenberg's representation, the time evolution of the system is contained at the time evolution of the operators, which for a random operator $\hat{\mathcal{O}}$ would be given by:

$$i\hbar\frac{d}{dt}\hat{\mathcal{O}} = \left[\hat{\mathcal{O}}, \hat{\mathcal{H}}\right] \tag{3.33}$$

where $\hat{\mathcal{H}}$ would be the system's total Hamiltonian.

Hence, an intuitive starting point would be to identify this total Hamiltonian. Three distinct terms contribute to the Hamiltonian that governs our system: one associated with the atom ($\hat{\mathcal{H}}_a$), another related to electromagnetic radiation ($\hat{\mathcal{H}}_{EM}$), and the third connected to the interaction between the atom and the laser field ($\hat{\mathcal{H}}_i$). Similar to the final subsection of the previous section, the analysis involves an atom initially in the ground state $|g\rangle$ transitioning to a final excited state $|e\rangle$ with an energy difference of $\hbar\omega_t$. Here, ω_t represents the resonance frequency between states $|g\rangle$ and $|e\rangle$. Given this context, the atomic operators that can describe the dynamics of this atomic system are:

$$\text{Difference between state's population: } \hat{\sigma} = |e\rangle\langle e| - |g\rangle\langle g| \tag{3.34a}$$

$$\text{Rising operator: } \hat{\sigma}^+ = |e\rangle\langle g| \tag{3.34b}$$

$$\text{Lowering operator: } \hat{\sigma}^- = |g\rangle\langle e| \tag{3.34c}$$

Using these operators, it is possible to write the three terms of the total Hamiltonian. For the atom operator, as long as we define the level zero of energy as $\hat{\mathcal{H}}_a|g\rangle = 0|g\rangle$ and the excited state energy as $\hat{\mathcal{H}}_a|e\rangle = \hbar\omega_t|e\rangle$, we have:

$$\hat{\mathcal{H}}_a = \frac{\hbar\omega_t}{2}\left(\hat{\sigma} + \frac{1}{2}\right) \tag{3.35}$$

The operator related to the electromagnetic radiation modes is the energy sum of all the vacuum modes, proportional to the annihilation and creation operators already discussed:

$$\hat{\mathcal{H}}_{EM} = \sum_{\boldsymbol{k},\epsilon} \hbar\omega_k \hat{a}^\dagger_{\boldsymbol{k},\epsilon}\hat{a}_{\boldsymbol{k},\epsilon} \tag{3.36}$$

Finally, for the interaction Hamiltonian it is necessary to consider the dipole operator $\hat{\boldsymbol{d}}$:

$$\hat{\boldsymbol{d}} = q\langle e|\hat{\boldsymbol{r}}|g\rangle\left(\hat{\sigma}^- + \hat{\sigma}^+\right) \tag{3.37}$$

with $\hat{\boldsymbol{r}}$ the electron position operator.

Which would provide us with:

$$\hat{\mathcal{H}}_i = \hat{\boldsymbol{d}} \cdot \left(\boldsymbol{E}_{laser}(r,t) + \hat{\boldsymbol{E}}(r,t) \right) \tag{3.38}$$

here, $\boldsymbol{E}_{laser}(r,t) = \boldsymbol{E_0} \cos(\boldsymbol{k}_{laser} \cdot \boldsymbol{r} - \omega_{laser} t)$ and $\hat{\boldsymbol{E}}(r,t)$ is the same as equation 3.27.

Thus, the total Hamiltonian for our system would be given by the following expression:

$$\begin{aligned}
\hat{\mathcal{H}} &= \hat{\mathcal{H}}_a + \hat{\mathcal{H}}_{EM} + \hat{\mathcal{H}}_i \\
&= \frac{\hbar\omega_t}{2}\left(\hat{\sigma} + \frac{1}{2}\right) + \sum_{\boldsymbol{k},\epsilon} \hbar\omega_k \hat{a}^\dagger_{\boldsymbol{k},\epsilon}\hat{a}_{\boldsymbol{k},\epsilon} + \frac{\hbar}{2}\left(\Omega_{rabi}(r)e^{-i\omega_{laser}t} + \Omega^*_{rabi}(r)e^{i\omega_{laser}t}\right)\left(\hat{\sigma}^- + \hat{\sigma}^+\right) \\
&\quad + i\hbar \sum_{\boldsymbol{k},\epsilon}\left(u_{\boldsymbol{k},\epsilon}(r)\hat{a}_{\boldsymbol{k},\epsilon}e^{-i\omega_k t} - u^*_{\boldsymbol{k},\epsilon}(r)\hat{a}^\dagger_{\boldsymbol{k},\epsilon}e^{i\omega_k t}\right)\left(\hat{\sigma}^- + \hat{\sigma}^+\right)
\end{aligned} \tag{3.39}$$

where $\Omega_{rabi} = q\langle e|\hat{\boldsymbol{r}}|g\rangle \cdot E_0 e^{i\boldsymbol{k}_{laser}\cdot\boldsymbol{r}}$ is the Rabi frequency and $u_{\boldsymbol{k},\epsilon}(r) = q\langle e|\hat{\boldsymbol{r}}|g\rangle \cdot \epsilon_{\boldsymbol{k},s}\sqrt{\hbar\omega_{\boldsymbol{k}}/2\varepsilon_0 V}e^{i\boldsymbol{r}\cdot\boldsymbol{R}}$ is the coupling between the atom and vacuum modes.

Having in our hands the total Hamiltonian of our system finally allow us to write the dynamic evolution of the atomic operators $\hat{\sigma}$, $\hat{\sigma}^+$ and $\hat{\sigma}^-$. Although it requires some algebra that I won't elucidate in this text, following reference [38] and its approximations, it is possible to find:

$$\frac{d\hat{\sigma}}{dt} = i\left(\hat{\sigma}^- - \hat{\sigma}^+\right)\left(\Omega_{rabi}(r)e^{-i\omega_{laser}t} + \Omega^*_{rabi}(r)e^{i\omega_{laser}t}\right) - \Gamma(1+\hat{\sigma}) \tag{3.40a}$$

$$\frac{d\hat{\sigma}^-}{dt} = -i\omega_t\hat{\sigma}^- + \frac{i\sigma}{2}\left(\Omega_{rabi}(r)e^{-i\omega_{laser}t} + \Omega^*_{rabi}(r)e^{i\omega_{laser}t}\right) - \frac{\Gamma}{2}\hat{\sigma}^- \tag{3.40b}$$

$$\left(\frac{d\hat{\sigma}^-}{dt}\right)^\dagger = \frac{d\hat{\sigma}^+}{dt} \tag{3.40c}$$

Due to the atom-laser coupling, it is also possible to simplify such algebra if we perform the rotating-wave approximation (RWA), turning the terms that oscillate with frequency $|2\omega_{laser}|$ negligible. Such approximation is valid in our system since $|\Delta| = |\omega_t - \omega_{laser}|, \Omega_{rabi} \ll \omega_{laser}$. Then, we can write the atomic operators within the context of the RWA:

$$\frac{d\hat{\varrho}}{dt} = i\left(\Omega^*_{rabi}(r)\hat{\varrho}^- - \Omega_{rabi}(r)\hat{\varrho}^+\right) - \Gamma(1+\hat{\varrho}) \tag{3.41a}$$

$$\frac{d\hat{\varrho}^-}{dt} = \left(i\Delta - \frac{\Gamma}{2}\right)\hat{\varrho}^- + i\frac{\Omega_{rabi}(r)}{2}\hat{\varrho} \tag{3.41b}$$

where the operators $\hat{\varrho}$ are the operators $\hat{\sigma}$ redefined considering the RWA.

During the demonstration of the classical first order correlation function, I considered that $E(t)$ was stationary over time t due to the nature of our experiment. Over here, I aim to consider the same thing. The stationary regime is reached when $t \to \infty$, or, in other words, when the dynamics of the system is null: $\frac{d\hat{\varrho}}{dt} = \frac{d\hat{\varrho}^-}{dt} = 0$. With that, a system of coupled equations for the mean value of the stationary operators $\langle\varrho\rangle$ and $\langle\varrho^-\rangle$ is found:

$$i\left(\Omega^*_{rabi}(r)\langle\varrho^-\rangle - \Omega_{rabi}(r)\langle\varrho^+\rangle\right) - \Gamma(1+\langle\varrho\rangle) = 0 \tag{3.42a}$$

$$\left(i\Delta - \frac{\Gamma}{2}\right)\langle\varrho^-\rangle + \frac{i\ \Omega_{rabi}(r)}{2}\langle\varrho\rangle = 0 \tag{3.42b}$$

We may solve this system for the average value of the population operator $\langle\varrho\rangle$, having as a result:

$$\langle\varrho\rangle = -\frac{\Delta^2 + \frac{\Gamma^2}{4}}{\Delta^2 + \frac{\Gamma^2}{4} + \frac{|\Omega_{rabi}(r)|^2}{2}} = -\frac{1}{1+s} \tag{3.43}$$

with the definition of saturation parameter $s = \frac{|\Omega_{rabi}(r)|^2/2}{\Delta^2+\Gamma^2/4}$, usually found in the literature, appearing.

Not only that but we also can rewrite the mean values of both rising and lowering atomic operators in terms of s:

$$\langle\varrho^-\rangle = \frac{-i}{1+s}\frac{\Omega_{rabi}(r)}{\Gamma - 2i\Delta} \tag{3.44a}$$

$$\langle\varrho^+\rangle = \frac{i}{1+s}\frac{\Omega^*_{rabi}(r)}{\Gamma + 2i\Delta} \tag{3.44b}$$

Elastic and Inelastic Intensities

Now that all the operators that act upon our system are presented, this discussion can move forward so to demonstrate how the intensity scattered by this system can be written as a sum of inelastic and elastic terms, and how that is affected by the saturation parameter s (justifying the correction that the interference contrast needs upon fitting the data I've measured, which will be discussed in the next chapter).

Just as the last previous sections and subsections, here I'll consider the stationary case as to simplify the algebra presented. Within this context, the electric field operator considered when

realizing the measurements ($\hat{E}^{(+)}$, due to the fact that a measurement takes into account the absorption and destruction of the photon, and thus is related to the annihilation operator term of the electric field operator) is now related to the electric field scattered by the atom, therefore being also related to the atom dynamic operators just found. The modulus of this electric field scattered by the atom in the far-field limit $\hat{E}_a^{(+)}$ is given by:

$$\hat{E}_a^{(+)}(\boldsymbol{r},t) = \frac{\boldsymbol{k}_{laser}^2|\boldsymbol{d}|}{4\pi\varepsilon_0|\boldsymbol{r}-\boldsymbol{R}|}\sin\theta_a\hat{\sigma}^-\left(t-\frac{|\boldsymbol{r}-\boldsymbol{R}|}{c}\right)e^{i\boldsymbol{k}_{laser}\cdot(\boldsymbol{r}-\boldsymbol{R})}e^{-i\omega_{laser}t} \tag{3.45}$$

where $\boldsymbol{d}$ is the electrical dipole moment of the atom, considered as a classical dipole that oscillates in order to achieve this equation, $\boldsymbol{r}$ the atoms position, $\boldsymbol{R}$ the detector position and θ_a the angle between $\boldsymbol{r}$ and the vector related to the oscillation direction of the dipole.

If we also consider its complex conjugate, $\hat{E}_a^{(-)}$, then the total intensity scattered by this atom can be found:

$$I(\boldsymbol{r},t) = \frac{\varepsilon_0 c}{2}\langle\hat{E}_a^{(-)}(\boldsymbol{r},t)\hat{E}_a^{(+)}(\boldsymbol{r},t)\rangle = I_0\left\langle\hat{\varrho}^+\left(t-\frac{|\boldsymbol{r}-\boldsymbol{R}|}{c}\right)\hat{\varrho}^-\left(t-\frac{|\boldsymbol{r}-\boldsymbol{R}|}{c}\right)\right\rangle \tag{3.46}$$

with $I_0 = \frac{c\boldsymbol{k}_{laser}^4|\boldsymbol{d}|^2}{32\pi^2\varepsilon_0|\boldsymbol{r}-\boldsymbol{R}|^2}\sin^2\theta_a$.

Or, in a simplified notation:

$$I(\boldsymbol{r},t) = I_0\langle\ \hat{\varrho}^+\hat{\varrho}^-\rangle \tag{3.47}$$

with I_0 being understood just as a proportional constant for this specific discussion.

But, from the definition for the atomic operators given by 3.34, and since those operators must operate within a closed base, it follows that:

$$\hat{\varrho}^+\hat{\varrho}^- = |e\rangle\langle e| \tag{3.48a}$$

$$|e\rangle\langle e| = \frac{\hat{\varrho}+1}{2} \tag{3.48b}$$

More than that, due to the stationary regime and from equations 3.44 and 3.43, it is possible to write the emitted intensity as a function of the saturation parameter:

$$\frac{I(r,t)}{I_0} = \left(\frac{\langle\hat{\varrho}\rangle}{2}+\frac{1}{2}\right) = \frac{1}{2}\frac{s}{s+1} \tag{3.49}$$

Since these calculations take into account the stationary state, which means consider only the mean value of the operators, this also means that fluctuations upon their values are being neglected. If we were to consider such fluctuations, we would need to rewrite the atomic operators as the following [39]:

$$\hat{\varrho}^-(t) = \langle\hat{\varrho}^-\rangle + \delta\hat{\varrho}^-(t) \tag{3.50a}$$

$$\hat{\varrho}^+(t) = \langle\hat{\varrho}^+\rangle + \delta\hat{\varrho}^+(t) \tag{3.50b}$$

Considering these fluctuations, and that their mean value is zero ($\langle\delta\varrho^-\rangle = \langle\delta\varrho^+\rangle = 0$), we end up with, for the emitted intensity:

$$\frac{I(r,t)}{I_0} = \langle\hat{\varrho}^+\hat{\varrho}^-\rangle = \langle\hat{\varrho}^+\rangle\langle\hat{\varrho}^-\rangle + \langle\delta\hat{\varrho}^+(t)\ \delta\hat{\varrho}^-(t)\rangle = \frac{I_{el}}{I_0} + \frac{I_{inel}}{I_0} \tag{3.51}$$

Meaning that we have found the total intensity of our system as a sum of an elastic and an inelastic terms. This holds to be true to the definition I presented earlier for each concept since the radiation spectra either remains the same (elastic term) or changes (inelastic) with respect to the incoming spectra. To demonstrate that we can, considering equations 3.44, first begin with the elastic one:

$$\frac{I_{el}}{I_0} = \langle\hat{\varrho}^+\rangle\langle\hat{\varrho}^-\rangle = \frac{i}{1+s}\frac{\Omega^*_{rabi}(r)}{\Gamma+2i\Delta}.\frac{-i}{1+s}\frac{\Omega_{rabi}(r)}{\Gamma-2i\Delta} = \frac{1}{2}\frac{s}{(s+1)^2} \tag{3.52}$$

The second term, related to the inelastic scattering, can be then calculated as:

$$\frac{I_{inel}}{I_0} = \langle\delta\hat{\varrho}^+(t)\ \delta\hat{\varrho}^-(t)\rangle = \frac{I(r,t) - I_{el}}{I_0} = \frac{1}{2}\frac{s^2}{(s+1)^2} \tag{3.53}$$

The dependence of s in the scattered intensity then becomes clear as both equations are presented. Plotting this relation, illustrated at figure 3.4, showcases how the contribution of each process is affected by it, which can be expected since both only change for one exact factor s. Notice, however, how the elastic term (equation 3.52) has a dependence on the Rabi frequency, which in turn is proportional to the classical electrical field from the incoming laser, thus not changing its radiation spectra and therefore being correctly named as elastic. For the inelastic term (equation 3.53), on the other hand, the radiation spectrum changes since this term carries the quantum characteristics of the system I've considered so far.

To demonstrate this, it is useful to calculate the normalized spectral density S_{norm} given by 3.24, but in order to do that we must first find the first order correlation function for this system. It follows from equation 3.32:

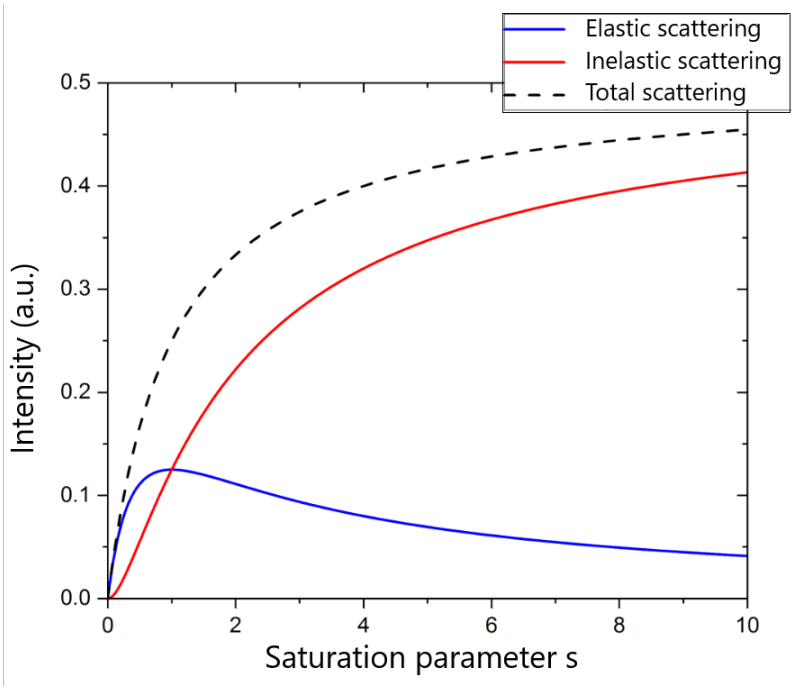

Figure 3.4: Plot from the intensities found in equations 3.52 and 3.53 as a function of the saturation parameter s.

Source: [40]

$$g^{(1)}(\tau) = \frac{\langle \hat{E}_a^{(-)}(\boldsymbol{r},t)\hat{E}_a^{(+)}(\boldsymbol{r},t+\tau)\rangle}{\sqrt{\langle \hat{E}_a^{(-)}(\boldsymbol{r},t)\hat{E}_a^{(+)}(\boldsymbol{r},t)\rangle\langle \hat{E}_a^{(-)}(\boldsymbol{r},t+\tau)\hat{E}_a^{(+)}(\boldsymbol{r},t+\tau)\rangle}} = \frac{\langle \hat{\varrho}^{+}(t)\hat{\varrho}^{-}(t+\tau)\rangle}{\sqrt{\langle \hat{\varrho}^{+}(t)\hat{\varrho}^{-}(t)\rangle\langle \hat{\varrho}^{+}(t+\tau)\hat{\varrho}^{-}(t+\tau)\rangle}} e^{-i\omega_{laser}\tau} \tag{3.54}$$

Where, using the relations from 3.50, we find:

$$g^{(1)}(\tau) = \frac{\langle (\langle \hat{\varrho}^{+}\rangle + \delta\hat{\varrho}^{+}(t))\,(\langle \hat{\varrho}^{-}\rangle + \delta\hat{\varrho}^{-}(t+\tau))\rangle}{\sqrt{\langle |\hat{\varrho}^{-}(t)|^2\rangle\langle |\hat{\varrho}^{-}(t+\tau)|^2\rangle}} e^{-i\omega_{laser}\tau}$$
$$= \frac{\langle \hat{\varrho}^{+}\rangle\langle \hat{\varrho}^{-}\rangle}{\sqrt{\langle |\hat{\varrho}^{-}(t)|^2\rangle\langle |\hat{\varrho}^{-}(t+\tau)|^2\rangle}} e^{-i\omega_{laser}\tau} + \frac{\langle \delta\hat{\varrho}^{+}(t)\delta\hat{\varrho}^{-}(t+\tau)\rangle}{\sqrt{\langle |\hat{\varrho}^{-}(t)|^2\rangle\langle |\hat{\varrho}^{-}(t+\tau)|^2\rangle}} e^{-i\omega_{laser}\tau} = g_{el}^{(1)}(\tau) + g_{inel}^{(1)}(\tau) \tag{3.55}$$

We now have found that the first order correlation function can also be written as the sum of terms related to elastic and inelastic scattering. This facilitates the calculations of the spectral density, where for the elastic term:

$$S_{norm,el}(\omega) = \frac{1}{\pi}\int_0^\infty g_{el}^{(1)}(\tau)e^{i\omega\tau}d\tau = \frac{s}{(s+1)^2}\delta(\omega-\omega_{laser}) \tag{3.56}$$

And for the inelastic term:

$$S_{norm,inel}(\omega) = \frac{1}{\pi}\int_0^\infty g_{inel}^{(1)}(\tau)e^{i\omega\tau}d\tau = \frac{1}{\pi}\int_0^\infty \langle\delta\hat{\varrho}^+(t)\delta\hat{\varrho}^-(t+\tau)\rangle e^{i(\omega-\omega_{laser})\tau}d\tau \tag{3.57}$$

While for the elastic term the solution is straightforward, showing a Dirac's delta behavior and justifying the non-change on the density spectra when compared to the incoming radiation, the solution for the inelastic term is more complex. It was obtained the first time by Benjamin Mollow in 1969 [41], and its solution has a dependence on the values of $\Omega_{rabi}(r)$, ω_t and ω. As demonstrated by reference [42], the solution for equation 3.57 can be given by:

$$\begin{aligned} S_{norm,inel}(\omega) = \frac{s}{4(s+1)}\mathrm{Re}\Bigg\{ &\frac{1}{\frac{\Gamma}{2}-i\omega} + \frac{1}{2}\frac{s-1}{s+1}\left(\frac{1}{\frac{3\Gamma}{4}+i(\omega-\Omega_M(r))} + \frac{1}{\frac{3\Gamma}{4}+i(\omega+\Omega_M(r))}\right) \\ &+ \frac{\Gamma}{8i\Omega_M(r)}\frac{5s-1}{s+1}\left(\frac{1}{\frac{3\Gamma}{4}+i(\omega-\Omega_M(r))} - \frac{1}{\frac{3\Gamma}{4}+i(\omega+\Omega_M(r))}\right)\Bigg\} \end{aligned} \tag{3.58}$$

The result is a scattering pattern for this spectral density which presents a center peak with two sidebands separated by the generalized Rabi frequency $\Omega_M(r) = \sqrt{\Omega_{Rabi}^2(r) - \Gamma^2/16}$ of the system. This is known as the Mollow Triplet. When compared to the elastic term on equation 3.56, it is possible to notice the broadening that the spectral density suffers here. This is why this term is called inelastic: the frequency density of light (and hence the energy density of the individual photons) is altered. Figure 3.5 illustrate such phenomena.

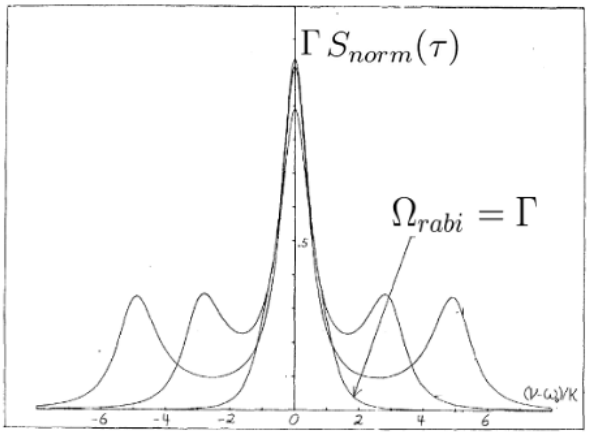

Figure 3.5: Spectral density S_{norm} for a two-level atom driven exactly on resonance. The figure highlight the broadening of such spectra with sidebands separated by different values of Rabi frequencies.

Source: [41], with modifications.

Chapter 4

THE INTERFEROMETRIC SYSTEM

At this chapter I'll present a discussion about the interferometric system we've built at our experiment, which provided the results of this thesis. The system itself is one already known called mirror-assisted Coherent BackScattering (mCBS). This type of system has as a specific property the presence of a mirror really close to the atomic cloud, which provides a set of characteristic circular fringes as a result.

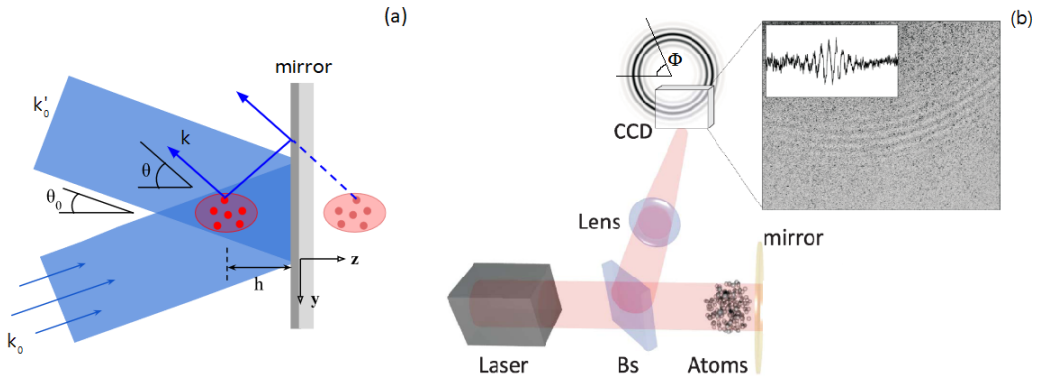

Figure 4.1: At (a), the interferometric system is presented in a simplified version, showcasing only the components responsible for the interference fringes. At (b) a representation of the same system along with the interference fringes mentioned. In this figure, θ_0 is the angle that the incoming beam is reflected by the mirror, θ is the angle of the light scattered by the cloud with respect to the normal of the mirror and ϕ is the azimuthal angle along the fringe's circumference pattern.

At figure 4.1a, the reader will find a schematic (simplified when compared to the actual system we needed to build) of the interference phenomenon we want to observe. An incoming field of wavevector $\mathbf{k}_0 = (0, -k\sin\theta_0, k\cos\theta_0)$ is reflected by a mirror with an angle θ_0. After being reflected, its wavevector changes to $\mathbf{k}_0' = (0, -k\sin\theta_0, -k\cos\theta_0)$. Meanwhile, we have the atomic cloud at a distance h from the mirror, which can scatter the light directly towards a position $\mathbf{R}$ in the far field (the detector position, at an angle θ) with wavevector $\mathbf{k} = (k\sin\theta\sin\phi, -k\sin\theta\cos\phi, -k\cos\theta)$ or to the mirror, with wavevector **k'** $= (k\sin\theta\sin\phi, -k\sin\theta\cos\phi, k\cos\theta)$. The angle ϕ is the azimuthal angle related to the fringes with circular pattern seen at 4.1b.

Interference phenomena emerge, as seen in chapter 3, from the superposition of at least two electric fields. In this type of setup, there are four electric fields that interfere with each other: i) the incoming field is directly scattered by the cloud towards the detector; ii) the incoming field first is reflected by the mirror and then scattered by the cloud towards the detector; iii) the incoming

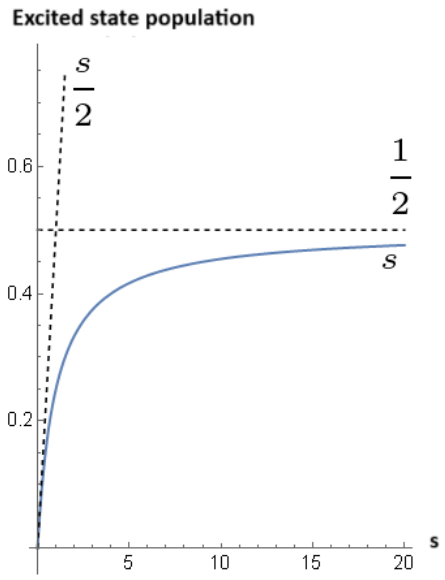

Figure 4.2: Graph depicting the population in the excited state as a function of the parameter s. The dashed lines serve to delineate the boundaries of the two distinct regimes characterizing the function.

Source: [25]

field is scattared by the cloud first towards the mirror, and then is reflected to the detector; and, finally, iv) both reflections happen, before being scattered by the cloud and afterwards. The interference of these four fields create the circular fringes. At the next section, I'll present the calculation for each of this fields in order to achieve an equation for the fringe's intensity profile.

4.1 Calculating the Intensity Profile

As stated, we have four paths and therefore four electric fields that will interfere with each other. To calculate the total electric field (and thus the intensity profile), we must take into account some system characteristics. One of them being the saturation parameter s, that emerges as a crucial factor in understanding the dynamics of light-matter interactions when calculating the Bloch equations. This parameter establishes a direct relationship with the excited state population ρ_e through the following equation [25]:

$$\rho_e = \frac{1}{2}\frac{s}{1+s} \tag{4.1}$$

The consequence of this relationship is shown in the asymptotic behavior observed in figure 4.2, which offers a visual representation of how ρ_e evolves concerning the saturation parameter. Beyond the graphical insight, s holds a significant interpretation: it characterizes the saturation level of our system, providing valuable information regarding the relationship between laser power and the population of atoms in the excited state (both are directly proportional, meaning the

higher the laser power, the closer to 1/2 the excited state population ρ_e gets, putting the system on a saturated regime). The calculations presented here assume the system resides in the linear regime, denoted by $s \ll 1$. In that sense, it is possible to continue the calculations, and state that the total electric field $\boldsymbol{E}_{T,1}$ for a single atom at position $\boldsymbol{r} = (x, y, z)$ and detected at $\boldsymbol{R}$ would be the sum of all the electric fields from each path:

$$\boldsymbol{E}_{T,1}(\boldsymbol{r}, \boldsymbol{R}) = \boldsymbol{E}_{1,I} + \boldsymbol{E}_{1,II} + \boldsymbol{E}_{1,III} + \boldsymbol{E}_{1,IV} \tag{4.2}$$

But, each path's field is different from one another and should be seen carefully. First, it is useful to understand that each path's field is related to either the incoming field and/or the reflected one. The incoming field is related to the wavevector $\mathbf{k}_0$ supposing an incoming monochromatic laser field:

$$\boldsymbol{E}_{inc}(r) = \boldsymbol{E_0}\ e^{i\mathbf{k}_0 \cdot \boldsymbol{r}} = \boldsymbol{E_0}\ e^{i(-k \sin\theta_0 y + k \cos\theta_0 z)} \tag{4.3}$$

While the reflected would be related to $\mathbf{k}_0'$:

$$\boldsymbol{E}_{refl}(r) = \boldsymbol{E_0}\ e^{i\boldsymbol{k_0'} \cdot \boldsymbol{r}} = \boldsymbol{E_0}\ e^{-i(k \sin\theta_0 y + k \cos\theta_0 z)} \tag{4.4}$$

For the electric field scattered by one atom at position r, giving the linear regime I'm considering, detected at R we have, however [30]:

$$\boldsymbol{E_1}(\boldsymbol{r}, \boldsymbol{R}) = \frac{k^2}{4\pi\varepsilon_0 R}\ \boldsymbol{P}(\boldsymbol{r})\ e^{i\boldsymbol{k} \cdot (\boldsymbol{R} - \boldsymbol{r})} \tag{4.5}$$

where $\boldsymbol{P}(\boldsymbol{r}) = \alpha \boldsymbol{E}(\boldsymbol{r})$ is the polarization induced in the atom by an incident electric field $\boldsymbol{E}$, with α being the dipole polarizability, and k the wavevector. Here, depending on the path, $\boldsymbol{E}$ can be either $\boldsymbol{E}_{inc}$ or $\boldsymbol{E}_{refl}$. Each path will have a different combination of these fields and their own characteristic. That being said, let's analyze the paths separately:

Path I

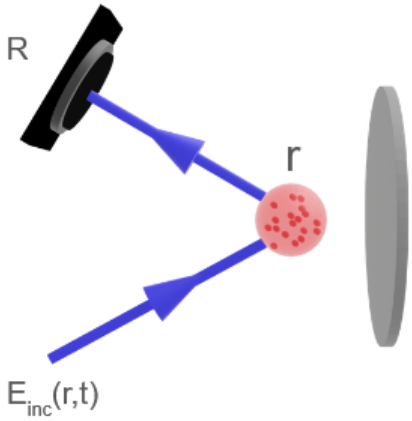

Figure 4.3: Path I may be interpreted as the shortest of the paths. Here, the incoming field $\boldsymbol{E}_{inc}(\boldsymbol{r}, t)$ is scattered by the cloud in position $\boldsymbol{r}$ directly into the detector at the far field, $\boldsymbol{R}$.

Figure 4.3 shows the path that light travels here, with the cloud interacting with the incoming field. Therefore we have $k = \mathbf{k}$ and $\boldsymbol{E} = \boldsymbol{E}_{inc}(\boldsymbol{r})$, which means that:

$$\begin{aligned} \boldsymbol{E}_{\mathbf{1},\boldsymbol{I}}(\boldsymbol{r}, \boldsymbol{R}) &= \frac{k^2}{4\pi\varepsilon_0 R}\, \boldsymbol{P}(\boldsymbol{r})\, e^{i\boldsymbol{k}\cdot(\boldsymbol{R}-\boldsymbol{r})} = \frac{k^2}{4\pi\varepsilon_0 R}\alpha e^{i\boldsymbol{k}\cdot\boldsymbol{R}} e^{-i\boldsymbol{k}\cdot\boldsymbol{r}} \boldsymbol{E}_{inc}(\boldsymbol{r}) \\ &= \frac{k^2\alpha \boldsymbol{E_0}}{4\pi\varepsilon_0 R}\, e^{ikR}\, e^{i(-k\sin\theta_0 y + C_0 z)}\, e^{-i\boldsymbol{k}\cdot\boldsymbol{r}} \end{aligned} \tag{4.6}$$

Since the detector position is at the direction of wavevector $\mathbf{k}$, then $\boldsymbol{k}\cdot\boldsymbol{R} = kR$. Also, from now on, we'll adopt $C_0 = k\cos\theta_0$, where $k = |\boldsymbol{k}|$ and $R = |\boldsymbol{R}|$.

Path II

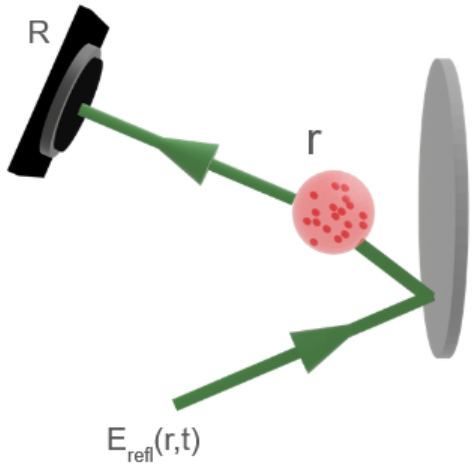

Figure 4.4: Path II shows that the incoming field is first reflected by the mirror before probing the cloud. It is, then, scattered to the detector.

At this one, the beam is first reflected before probing the cloud, as seen in figure 4.4. Hence $\boldsymbol{E} = \boldsymbol{E}_{refl}(\boldsymbol{r})$.

$$\boldsymbol{E}_{\mathbf{1},\boldsymbol{II}}(r,R) = \frac{k^2}{4\pi\varepsilon_0 R}\ \alpha\ e^{i\boldsymbol{k}\cdot\boldsymbol{R}}\ e^{-i\boldsymbol{k}\cdot\boldsymbol{r}}\boldsymbol{E}_{refl}(\boldsymbol{r}) = \frac{k^2\alpha\boldsymbol{E_0}}{4\pi\varepsilon_0 R}\ e^{ikR}\ e^{-i(k\sin\theta_0 y + C_0 z)}\ e^{-i\boldsymbol{k}\cdot\boldsymbol{r}} \tag{4.7}$$

For paths III and IV, however, we must take into account the fact that the scattered field can be thought of as emitted by the mirror image of the atom, at position $\boldsymbol{r'} = (x, y, -z)$ and with same wavevector $\mathbf{k}$ (recalling Figure 4.1a, that would be the atoms represented on the cloud at the right side of the mirror). That being said, let's continue.

Path III

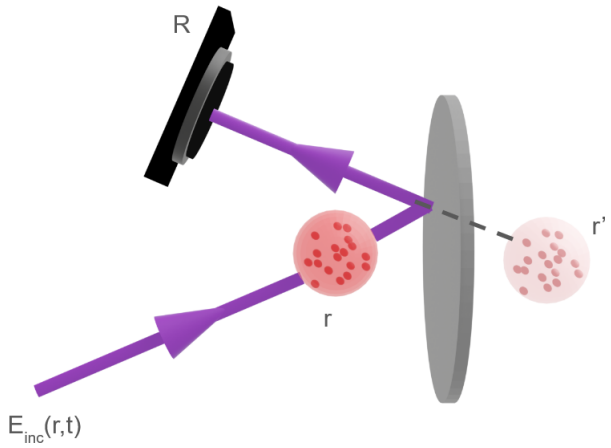

Figure 4.5: Path III may be interpreted as basically the opposite of path II: the cloud scatter the field towards the mirror, which is then reflected towards the detector.

At this path, seen in figure 4.5, the electric field probes the cloud and, afterwards, is scattered to the mirror's direction. Therefore, what we have is the incoming field but, as mentioned, as if emitted at position $\boldsymbol{r'}$. The electric field considered is the incoming one. Thus:

$$\boldsymbol{E}_{\mathbf{1},III}(\boldsymbol{r'},\boldsymbol{R}) = \frac{k^2}{4\pi\varepsilon_0 R}\,\boldsymbol{P}(\boldsymbol{r})\; e^{i\boldsymbol{k}\cdot(\boldsymbol{R}-\boldsymbol{r'})} = \frac{k^2}{4\pi\varepsilon_0 R}\alpha e^{i\boldsymbol{k}\cdot\boldsymbol{R}} e^{-i\boldsymbol{k}\cdot\boldsymbol{r'}}\boldsymbol{E}_{inc}(\boldsymbol{r})$$
$$= \frac{k^2\alpha\boldsymbol{E_0}}{4\pi\varepsilon_0 R}\; e^{ikR}\; e^{i(-k\sin\theta_0 y + C_0 z)} e^{-i\boldsymbol{k}\cdot\boldsymbol{r'}} \tag{4.8}$$

Path IV

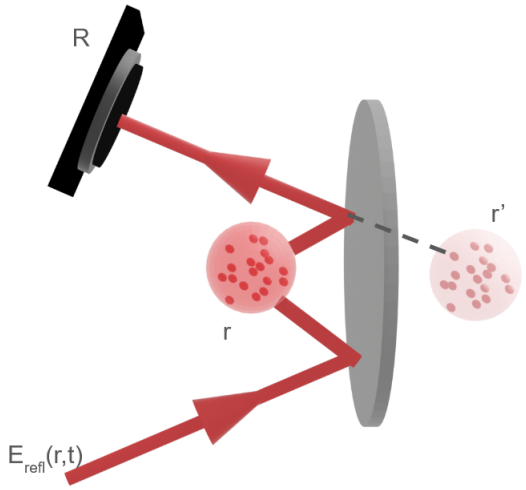

Figure 4.6: Path IV is the longest of the paths, where the field is reflected by the mirror before interacting with the cloud, which then scatters the field towards the mirror once more before finally traveling towards the detector.

Finally, for the path with both reflections (figure 4.6), we'll have the laser field reflected along with the fact of being scattered by the atom's mirror image, giving us:

$$\boldsymbol{E_{1,IV}}(\boldsymbol{r'},\boldsymbol{R}) = \frac{k^2\alpha e^{ikR}}{4\pi\varepsilon_0 R} e^{-i\boldsymbol{k}\cdot\boldsymbol{r'}} \boldsymbol{E}_{refl}(\boldsymbol{r}) = \frac{k^2\alpha \boldsymbol{E_0}}{4\pi\varepsilon_0 R}\ e^{ikR}\ e^{-i(k\sin\theta_0 y + C_0 z)} e^{-i\boldsymbol{k}\dot{\boldsymbol{r}}'} \tag{4.9}$$

With all the ingredients, we are now ready to calculate the total electric field. Following equation 4.2 and each field calculated in the paths before, we have:

$$\begin{aligned}
\boldsymbol{E_{T,1}}(\boldsymbol{r},\boldsymbol{R}) &= \boldsymbol{E_{1,I}} + \boldsymbol{E_{1,II}} + \boldsymbol{E_{1,III}} + \boldsymbol{E_{1,IV}} \\
&= \frac{k^2\alpha \boldsymbol{E_0}}{4\pi\varepsilon_0 R}\ e^{ikR}\ e^{i(-k\sin\theta_0 y + C_0 z)}\ e^{-i\boldsymbol{k}\cdot\boldsymbol{r}} + \frac{k^2\alpha \boldsymbol{E_0}}{4\pi\varepsilon_0 R}\ e^{ikR}\ e^{-i(k\sin\theta_0 y + C_0 z)}\ e^{-i\boldsymbol{k}\cdot\boldsymbol{r}} \\
&+ \frac{k^2\alpha \boldsymbol{E_0}}{4\pi\varepsilon_0 R}\ e^{ikR}\ e^{i(-k\sin\theta_0 y + C_0 z)} e^{-i\boldsymbol{k}\cdot\boldsymbol{r'}} + \frac{k^2\alpha \boldsymbol{E_0}}{4\pi\varepsilon_0 R}\ e^{ikR}\ e^{-i(k\sin\theta_0 y + C_0 z)} e^{-i\boldsymbol{k}\cdot\boldsymbol{r'}} \\
&= \frac{k^2\alpha \boldsymbol{E_0}}{4\pi\varepsilon_0 R}\ e^{ikR}\{e^{i(-k\sin\theta_0 y + C_0 z)}\ e^{-i\boldsymbol{k}\cdot\boldsymbol{r}} + e^{-i(k\sin\theta_0 y + C_0 z)}\ e^{-i\boldsymbol{k}\cdot\boldsymbol{r}} \\
&\qquad + e^{i(-k\sin\theta_0 y + C_0 z)} e^{-i\boldsymbol{k}\cdot\boldsymbol{r'}} + e^{-i(k\sin\theta_0 y + C_0 z)} e^{-i\boldsymbol{k}\cdot\boldsymbol{r'}}\}
\end{aligned} \tag{4.10}$$

The colors in the equation above identify the terms related to each path: I, II, III and IV. Let's first, for didactic purposes, pay attention to all of these terms before coming back and rewriting the total electric field. Recalling that **r** = (x, y, z), **r'** = $(x, y, -z)$ and **k** = $(k\sin\theta\sin\phi, -k\sin\theta\cos\phi, -k\cos\theta)$, we have that:

$$\boldsymbol{k}\cdot\boldsymbol{r} = (k\sin\theta\sin\phi, -k\sin\theta\cos\phi, -k\cos\theta)(x,y,z) = k\sin\theta\sin\phi\ x - k\sin\theta\cos\phi\ y - Cz \tag{4.11a}$$

$$\boldsymbol{k}\cdot\boldsymbol{r'} = (k\sin\theta\sin\phi, -k\sin\theta\cos\phi, -k\cos\theta)(x,y,-z) = k\sin\theta\sin\phi\ x - k\sin\theta\cos\phi\ y + Cz \tag{4.11b}$$

where $C = k\cos\theta$.

That way, looking at the sum inside the brackets, we get:

$$\begin{aligned}
&\{e^{i(-k\sin\theta_0 y + C_0 z)}\ e^{-i\boldsymbol{k}\cdot\boldsymbol{r}} + e^{-i(k\sin\theta_0 y + C_0 z)}\ e^{-i\boldsymbol{k}\cdot\boldsymbol{r}} + e^{i(-k\sin\theta_0 y + C_0 z)} e^{-i\boldsymbol{k}\cdot\boldsymbol{r'}} + e^{-i(k\sin\theta_0 y + C_0 z)} e^{-i\boldsymbol{k}\cdot\boldsymbol{r'}}\} \\
&= e^{i(-k\sin\theta_0 y + C_0 z)} e^{-i(k\sin\theta\sin\phi\ x - k\sin\theta\cos\phi\ y - Cz)} + e^{-i(k\sin\theta_0 y + C_0 z)} e^{-i(k\sin\theta\sin\phi\ x - k\sin\theta\cos\phi\ y - Cz)} \\
&+ e^{i(-k\sin\theta_0 y + C_0 z)} e^{-i(k\sin\theta\sin\phi\ x - k\sin\theta\cos\phi\ y + Cz)} + e^{-i(k\sin\theta_0 y + C_0 z)} e^{-i(k\sin\theta\sin\phi\ x - k\sin\theta\cos\phi\ y + Cz)} \\
&= e^{-ik\sin\theta_0 y}\ e^{-ik\sin\theta\sin\phi\ x}\ e^{ik\sin\theta\cos\phi\ y}\left(e^{i(C_0+C)z} + e^{-i(C_0-C)z} + e^{i(C_0-C)z} + e^{-i(C_0+C)z}\right)
\end{aligned} \tag{4.12}$$

Which in turn give us, finally, the total electric field equation:

$$\boldsymbol{E_{T,1}}(\boldsymbol{r},\boldsymbol{R}) = \frac{k^2\alpha \boldsymbol{E_0}}{4\pi\varepsilon_0 R}\; e^{ikR}e^{-ik\sin\theta_0 y}\; e^{-ik\sin\theta\sin\phi\;\, x}\; e^{ik\sin\theta\cos\phi\;\, y} \left(e^{i(C_0+C)z} + e^{-i(C_0-C)z} + e^{i(C_0-C)z} + e^{-i(C_0+C)z}\right) \quad (4.13)$$

Or, for simplicity,

$$\boldsymbol{E_{T,1}}(\boldsymbol{r},\boldsymbol{R}) = \frac{k^2\alpha \boldsymbol{E_0}}{4\pi\varepsilon_0 R}\; e^{ikR}e^{-ik\sin\theta_0 y}\; e^{-ik\sin\theta\sin\phi\;\, x}\; e^{ik\sin\theta\cos\phi\;\, y}\; \mathcal{E} \quad (4.14)$$

Where:

$$\mathcal{E} = e^{i(C_0+C)z} + e^{-i(C_0-C)z} + e^{i(C_0-C)z} + e^{-i(C_0+C)z} \quad (4.15)$$

As intended, notice that the total electric field that reaches our detector is indeed a combination of the four possible paths the light may travel. Now, to calculate the intensity profile that arises from such electric field, it is necessary to calculate the intensity scattered by one atom $I_1(r,R)$, which can be given by:

$$I_1(\boldsymbol{r},\boldsymbol{R}) = \frac{\varepsilon_0 c}{2}|\; \boldsymbol{E_{T,1}}(r,R)\;|^2 = \frac{\varepsilon_0 c}{2}\;\langle \boldsymbol{E_{T,1}}^{\dagger}\cdot \boldsymbol{E_{T,1}}\rangle = \frac{k^4 c|\alpha|^2|\boldsymbol{E_0}|^2}{32\pi^2\varepsilon_0 R^2}\;\mathcal{E}^{\dagger}\cdot\mathcal{E} \quad (4.16)$$

Calculating the intensity profile is, at the very end, the same thing as to calculate $\mathcal{E}^{\dagger}\cdot\mathcal{E}$:

$$\begin{aligned}\mathcal{E}^{\dagger}\cdot\mathcal{E} &= \left(e^{-i(C_0+C)z} + e^{i(C_0-C)z} + e^{-i(C_0-C)z} + e^{i(C_0+C)z}\right)\\ &\quad\cdot\left(e^{i(C_0+C)z} + e^{-i(C_0-C)z} + e^{i(C_0-C)z} + e^{-i(C_0+C)z}\right)\\ &= 4+\left(e^{2i(C_0+C)z} + e^{-2i(C_0+C)z}\right)+\left(e^{2i(C_0-C)z} + e^{-2i(C_0-C)z}\right)+2\left(e^{2iC_0z} + e^{-2iC_0z}\right)+2\left(e^{2iCz} + e^{-2iCz}\right)\\ &= 4\left(1+\frac{1}{2}\cos[2C_0z+2Cz]+\frac{1}{2}\cos[2C_0z-2Cz]+2\cos(C_0z+Cz)\cos(C_0z-Cz)\right)\end{aligned} \quad (4.17)$$

where I have used that $\cos a+\cos b = 2\cos\left(\frac{a+b}{2}\right)\cos\left(\frac{a-b}{2}\right)$ and $e^{ix}+e^{-ix} = 2\cos(x)$.

Consequently, the equation for the intensity profile of the light scattered by a single atom has been found:

$$I_1(\boldsymbol{r},\boldsymbol{R}) = I_a\left(1+\frac{1}{2}\cos[2(C_0+C)z]+\frac{1}{2}\cos[2(C_0-C)z]+2\cos(C_0z+Cz)\cos(C_0z-Cz)\right) \quad (4.18)$$

here, $I_a = \frac{k^4 c|\alpha|^2|E_0|^2}{8\pi^2\varepsilon_0 R^2}$.

At our system, however, we must calculate the intensity profile for a whole atomic cloud. Such cloud is considered to have a gaussian distribution density profile, which can be given by:

$$\rho(r) = \frac{N}{(2\pi)^{3/2}\ s_z\ s_r^2}\ e^{-\frac{(x^2+y^2)}{2s_r^2}}\ e^{-\frac{(z+h)^2}{2s_z^2}} \tag{4.19}$$

with s_z and s_r being the longitudinal and radial sizes of the cloud, respectively.

To calculate the total intensity, we integrate over all directions:

$$I_T(\boldsymbol{r}) = \int_{\mathbb{R}^3} \rho(\boldsymbol{r}) I_1(\boldsymbol{r},t) d\boldsymbol{r}^3 = \int_{\mathbb{R}^3} \frac{N}{(2\pi)^{3/2}\ s_z\ s_r^2}\ e^{-\frac{(x^2+y^2)}{2s_r^2}}\ e^{-\frac{(z+h)^2}{2s_z^2}}\ I_a \left(1 + \frac{1}{2}\cos[2(C_0+C)z] + \frac{1}{2}\cos[2(C_0-C)z] + 2\cos(C_0z+Cz)\cos(C_0z-Cz)\right) dr^3 = \frac{NI_a}{(2\pi)^{3/2}\ s_z\ s_r^2} \int_{-\infty}^{\infty} e^{-\frac{(x^2+y^2)}{2s_r^2}} dxdy \int_{-\infty}^{\infty} e^{-\frac{(z+h)^2}{2s_z^2}}\ \left(1 + \frac{1}{2}\cos[2(C_0+C)z] + \frac{1}{2}\cos[2(C_0-C)z] + 2\cos(C_0z+Cz)\cos(C_0z-Cz)\right) dz \tag{4.20}$$

The first integral has no mystery: $\int_{-\infty}^{\infty} e^{-\frac{(x^2+y^2)}{2s_r^2}} dxdy = 2\pi s_r^2$. But the second requires a bit more attention. That because, essentially, when doing such integral we are actually averaging the intensity $I_1(r,t)$ over all possible z positions of the cloud's atom. Each term of equation 4.20 behaves differently with the consequent averaging. The cosine argument $C_0z + Cz$ oscillates fast, which means that $\cos(2C_0z + 2Cz)$ and $\cos(C_0z + Cz)$ averages to 0. On the other hand, the term with argument $C_0z - Cz$ gives rise to the fringes and the result of such term when averaging over the atomic cloud is:

$$\langle \cos[2(C_0z - Cz)] \rangle \simeq e^{-2(k\theta_0 s_z)^2(\theta-\theta_0)^2} \cos[2\theta_0 kh(\theta-\theta_0)] \tag{4.21}$$

leading us to:

$$I_T(r) = \frac{NI_a}{(2\pi)^{3/2}\ s_z\ s_r^2}\ 2\pi\ s_r^2\ \int_{-\infty}^{\infty} e^{-\frac{(z+h)^2}{2s_z^2}}\ \left(1 + \frac{1}{2}\cos[2(C_0-C)z]\right) dz \tag{4.22}$$

Then, we finally have:

$$I_T(\theta) = NI_a \left(1 + \frac{1}{2} e^{-2(k\theta_0 s_z)^2(\theta-\theta_0)^2} \cos[2\theta_0 kh(\theta-\theta_0)]\right) \tag{4.23}$$

When examining both intensity profiles calculated through equations 4.18 (which considers only a single atom scattering the radiation) and 4.23 (encompassing the whole cloud), there is a characteristic that is worth to notice. Specifically, both intensity profiles show that the fringes present a circular profile, depending not on ϕ but only on θ. This circular profile emerges as an intrinsic aspect of the mCBS configuration, highlighting the particular geometric nature of this interferometric setup. It is noteworthy that this circular profile manifests consistently across both individual atom scenarios and when considering the aggregate response of the entire atomic cloud. This observation contributes to a deeper understanding of the spatial distribution of interference fringes within the context of mCBS. On what I aim to investigate within this work, this circular profile provided the liberty to explore our system in a specific configuration that allowed the break of reciprocity on a system otherwise not expected to do so.

4.2 Adding the polarization

At the previous section, I demonstrated the calculations for the intensity profile inherent to the mCBS, which is the experimental setup we have at our interferometer. By studying the four possible paths the light may travel, an equation for the total intensity profile was constructed. The new aspect I aim to introduce in this study involves the analysis of how different components that act upon the light polarization may affect such result. Two main components at our experimental interferometer system are relevant in order to consider this, both seen at figure 4.7: the half-waveplate (HWP, depicted in orange) and the 45° mirror (depicted in purple).

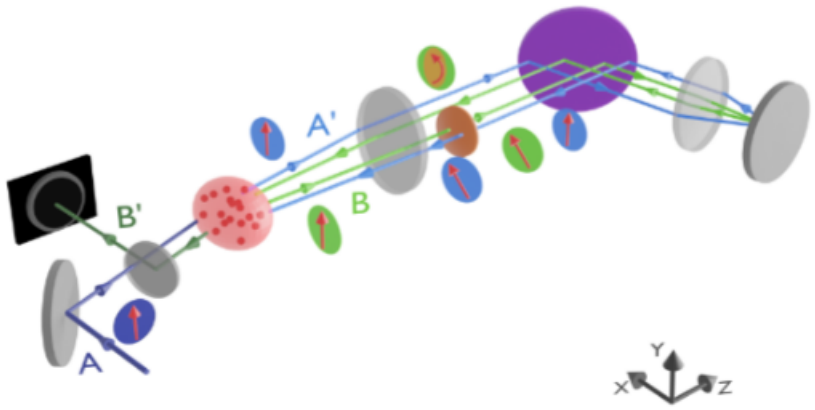

Figure 4.7: A representation of our interferometric system, where are depicted not only the set of lenses in order to create the virtual mirror, but also the waveplate (orange) and the 45° mirror (purple).

Each of these components will apply different transformations to the light polarization. When reflected twice by a dielectric mirror, a relative phase shift ξ is induced in the $\boldsymbol{\epsilon_y}$ direction of the light polarization. This relative phase shift can be equated as the following linear transformation:

$$\hat{\mathcal{M}}[\boldsymbol{\epsilon_x}] = \boldsymbol{\epsilon_x} \tag{4.24a}$$

$$\hat{\mathcal{M}}[\boldsymbol{\epsilon_y}] = e^{i\xi}\boldsymbol{\epsilon_y} \tag{4.24b}$$

While the change in the polarization provided by the waveplate can be described by:

$$\hat{\mathcal{P}}[\boldsymbol{\epsilon_x}] = \boldsymbol{\epsilon_1} \tag{4.25a}$$

$$\hat{\mathcal{P}}[\boldsymbol{\epsilon_1}] = \boldsymbol{\epsilon_x} \tag{4.25b}$$

Where

$$\boldsymbol{\epsilon_1} = \cos\gamma\ \boldsymbol{\epsilon_x} + \sin\gamma\ \boldsymbol{\epsilon_y} \tag{4.26}$$

here, γ is a factor related to the angle chosen at the waveplate.

At our experiment, we are looking at the fringes through the slice of the circular fringes related to $\phi = \pi$, where our detector sees the light that is back-scattered by our system. That means that the detection is made at the furthest direction with respect to the reflected laser beam, basically $\boldsymbol{k} \sim -\boldsymbol{k_0'}$. In this case, both the reflected laser beam and the scattered light will suffer specific transformations depending on which path they travel. Since it was shown that only paths II and III are the ones responsible for the fringes, I'll focus the following discussion on both of these paths. Paths I and IV are still needed to achieve the final equation of this section, but since they only contribute for background radiation, their omission from the calculations can be justified for concise matters only.

For path II, the beam hits the mirror twice before passing through the waveplate, so the total transformation at the polarization of the reflected light is given by $\hat{\mathcal{T}}_1 = \hat{\mathcal{P}} \circ \hat{\mathcal{M}}$, which means that the electric field considered is: $\mathbf{E}_{refl}(r) = \boldsymbol{E_0}\ e^{i\boldsymbol{k_0'}r}\ \hat{\mathcal{T}}_1[\boldsymbol{\epsilon_x}] = \boldsymbol{E_0}\ e^{-i(k\sin\theta_0 y + C_0 z)}\ \boldsymbol{\epsilon_1}$. Resulting in:

$$\mathbf{E}_{1,II}(r,R) = \frac{k^2\alpha E_0}{4\pi\varepsilon_0 R} e^{ikR}\ e^{-i(k\sin\theta_0 y + C_0 z)}\ e^{-i\boldsymbol{kr}}\ \boldsymbol{\epsilon_1} \tag{4.27}$$

since $\hat{\mathcal{T}}_1[\boldsymbol{\epsilon_x}] = \hat{\mathcal{P}} \circ \hat{\mathcal{M}}[\boldsymbol{\epsilon_x}] = \hat{\mathcal{P}}[\boldsymbol{\epsilon_x}] = \boldsymbol{\epsilon_1}$.

For path III, however, due to $\phi = \pi$ the scattered light goes the other way around, passing first by the waveplate and therefore suffering another transformation $\hat{\mathcal{T}}_2 = \hat{\mathcal{M}} \circ \hat{\mathcal{P}}$. Since in this path we have the incoming beam, what we have is: $\mathbf{E}_{inc}(r) = \boldsymbol{E_0}\ e^{i\boldsymbol{k_0}\cdot\boldsymbol{r}}\ \hat{\mathcal{T}}_2[\boldsymbol{\epsilon_x}] = \boldsymbol{E_0}\ e^{i(-k\sin\theta_0 y + C_0 z)}\ \boldsymbol{\epsilon_2}$. Thus, the electric field for path III considering the polarization changes is:

$$\mathbf{E}_{1,III}(\boldsymbol{r'}, \boldsymbol{R}) = \frac{k^2 \alpha \boldsymbol{E_0}}{4\pi\varepsilon_0 R}\ e^{ikR}\ e^{i(-k\sin\theta_0 y + C_0 z)} e^{-i\boldsymbol{k}\cdot\boldsymbol{r'}}\ \boldsymbol{\epsilon_2} \tag{4.28}$$

where $\boldsymbol{\epsilon_2} = \cos\gamma\ \boldsymbol{\epsilon_x} + \sin\gamma\ e^{i\xi}\boldsymbol{\epsilon_y}$

Before continuing with the calculations, an important concept surrounding these transformations must be looked with care. Because of their nature, where one path would be at first glance reciprocal to the other, due to their similar path lengths, the fact that both share the same transformations but in opposite order is not negligible. To understand why that is, we can look at the transformations $\hat{\mathcal{M}}$ and $\hat{\mathcal{P}}$ as matrices, where considering the Jones formalism can be written as [43], [44]:

$$\hat{\mathcal{M}} = \begin{bmatrix} 1 & 0 \\ 0 & e^{i\xi} \end{bmatrix} \quad \hat{\mathcal{P}} = \begin{bmatrix} \cos\gamma & \sin\gamma \\ \sin\gamma & -\cos\gamma \end{bmatrix}$$

And when calculating the commutator of both matrices, we get:

$$[\hat{\mathcal{M}}, \hat{\mathcal{P}}] = \begin{bmatrix} 0 & \sin\gamma(1 - e^{i\xi}) \\ \sin\gamma(e^{i\xi} - 1) & 0 \end{bmatrix}$$

It is worth to notice that these transformations only commute for specific values of γ ($n\pi$) and ξ (0). For any other value, the commutation does not happen, meaning that for the majority of the cases, the paths are actually non-reciprocal. This will impact how the interference pattern is measured, causing a geometrical phase acquired by the light and affecting both the fringe's center and its contrast, but that discussion will be made later on in the text. For now, let's get back to calculating the total intensity. Recalling that I'm only showing the calculations for paths II and III, we may summarize the total electric field to the following result:

$$\begin{aligned} \mathbf{E}_{1,T}(r, R) &= \mathbf{E}_{1,II}\ +\ \mathbf{E}_{1,III} \\ &= \frac{k^2 \alpha \boldsymbol{E_0}}{4\pi\varepsilon_0 R}\ e^{ikR} e^{-ik\sin\theta_0 y}\ e^{-ik\sin\theta\sin\phi\ x}\ e^{ik\sin\theta\cos\phi\ y} \left(e^{-i(C_0 - C)z}\boldsymbol{\epsilon_1} + e^{i(C_0 - C)z}\boldsymbol{\epsilon_2}\right) \end{aligned} \tag{4.29}$$

As in the previous section, when calculating the total intensity, the only necessary calculus is to see what happens with the terms inside the parenthesis. That being said:

$$\begin{aligned}\left(e^{i(C_0-C)z}\boldsymbol{\epsilon_1^*}+e^{-i(C_0-C)z}\boldsymbol{\epsilon_2^*}\right)\cdot\left(e^{-i(C_0-C)z}\boldsymbol{\epsilon_1}+e^{i(C_0-C)z}\boldsymbol{\epsilon_2}\right)\\ =e^{2i(C_0-C)z}\left(\cos^2\gamma+e^{i\xi}\sin^2\gamma\right)+e^{-2i(C_0-C)z}\left(\cos^2\gamma+e^{-i\xi}\sin^2\gamma\right)\\ =\cos^2\gamma\left(e^{2i(C_0-C)z}+e^{-2i(C_0-C)z}\right)+\sin^2\left(e^{2i(C_0-C)z}e^{i\xi}+e^{-2i(C_0-C)z}e^{-i\xi}\right)\\ =2\cos^2\gamma\cos(2C_0z-2Cz)+2\sin^2\gamma\cos(2C_0z-2Cz+\xi)\end{aligned}\tag{4.30}$$

Where what we get as a result is the following equation for the intensity:

$$I_1(\boldsymbol{r},\boldsymbol{R})=\frac{k^4c|\alpha|^2|\boldsymbol{E_0}|^2}{32\pi^2\varepsilon_0R^2}\;2\left(\cos^2\gamma\cos(2C_0z-2Cz)+\sin^2\gamma\cos(2C_0z-2Cz+\xi)\right)\tag{4.31}$$

Still, the equations presented so far in this section are for the one atom case. To carry this discussion to the atomic cloud approach, the same gaussian distribution from equation 4.19 must be considered. When doing this type of calculation, what we have is yet another term that doesn't vanish when doing the average of $I_1(\boldsymbol{r})$ over all the possible z positions of the cloud's atom (i.e., another term that have the C_0z-Cz argument, from paths II and III). This new term is the one resulting from the existence of the phase shift ξ:

$$\langle\cos[2(C_0z-Cz)+\xi]\rangle\simeq e^{-2(k\theta_0s_z)^2(\theta-\theta_0)^2}\cos[2\theta_0kh(\theta-\theta_0)+\xi]\tag{4.32}$$

Finally leading us to:

$$I_T(\boldsymbol{r})=NI_a\left[1+\frac{1}{2}e^{-2(k\theta_0s_z)^2(\theta-\theta_0)^2}\left(\cos^2\gamma\;\cos[2\theta_0kh(\theta-\theta_0)]+\sin^2\gamma\;\cos[2\theta_0kh(\theta-\theta_0)+\xi]\right)\right]\tag{4.33}$$

Of course, as mentioned equation 4.33 not only considers the terms relative to paths II and III that give rise to the fringes but also paths I and IV, responsible for the background radiation. It is worth to mention, however, that such equation is not on its final form so as the one that I've used to perform the data treatment. Although the factors ξ and γ may be measured directly through different equipment (which will be discussed in the following section), it would be easier to fit the data if such factors were related to the contrast, which as explained in chapter 3, is a practical observable: we only need to measure the fringes amplitude and divide it by the background intensity.

4.3 Contrast, Pancharatnam-Berry's phase and Intensity Corrections

To develop such relation between equation 4.33 and the desired contrast $\mathcal{C}$, let's pay a close attention to the term inside the parenthesis of that equation. It is possible to relate both terms through the following equation:

$$\left(\cos^2\gamma\ \cos\Phi + \sin^2\gamma\ \cos(\Phi+\xi)\right) = \mathcal{C}\cos(\Phi-\delta) \tag{4.34}$$

where $\Phi = 2\theta_0 kh(\theta-\theta_0)$ is the phase that describe the angular fringes and δ a displacement of the fringes center with respect to θ_0 that happened during our measurements.

Using the trigonometrical identity $\cos(a-b) = \cos a\cos b + \sin a\sin b$ on both sides, we get:

$$\cos\Phi\{\cos^2\gamma + \sin^2\gamma\cos\xi\} - \sin^2\gamma\sin\xi\sin\Phi = \mathcal{C}\cos\delta\cos\Phi + C\sin\delta\sin\Phi \tag{4.35}$$

Which can only be true if the following system of equations is also true:

$$\mathcal{C}\cos\delta = \cos^2\gamma + \sin^2\gamma\cos\xi \tag{4.36a}$$
$$\mathcal{C}\sin\delta = -\sin^2\gamma\sin\xi \tag{4.36b}$$

Squaring both sides and summing them, we get:

$$\begin{aligned}\mathcal{C}^2 = \cos^4\gamma + \sin^4\gamma + 2\sin^2\gamma\cos^2\gamma\cos\xi &= \left(1-\sin^2\gamma\right)^2 + \sin^4\gamma + 2\sin^2\gamma\cos^2\gamma\cos\xi \\ &= 1 + 2\left(\sin^4\gamma - \sin^2\gamma + \sin^2\gamma\cos^2\gamma\cos\xi\right) = 1 + 2\sin^2\gamma\cos^2\gamma\left(\cos\xi - 1\right) \\ 1 + \frac{\sin^2(2\gamma)}{2}\left(\cos\xi - 1\right) &= 1 + \frac{\sin^2(2\gamma)}{2}\left(1 - 2\sin^2(\xi/2) - 1\right)\end{aligned} \tag{4.37}$$

Resulting in the following equation for the contrast:

$$\mathcal{C} = \sqrt{1 - \sin^2(2\gamma)\sin^2(\xi/2)} \tag{4.38}$$

Here, we found an equation for the contrast $\mathcal{C}$ with respect to the parameters ξ and γ, responsible for the polarization transformation discussed so far. Figure 4.8 shows this dependence and how those factors affect the contrast seen in our system for two different values of s (the influence of the saturation parameter s will be explored in this section, yet, here it's valuable to only grasp the influence of ξ and γ over $\mathcal{C}$ due to the discussion being made). This bring us one step closer to

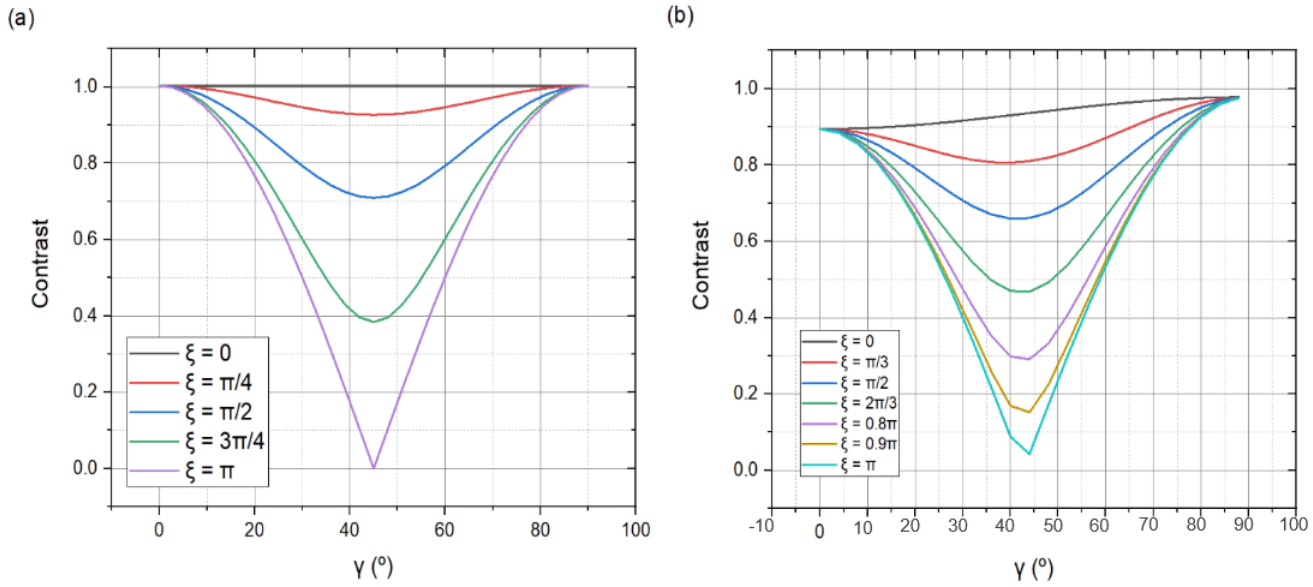

Figure 4.8: Both graphs outline the contrast behavior attributed to the polarization angle, which has a direct correlation to the factor γ. In (a), this behavior is depicted for a saturation parameter of $s = 0.0001$, while at (b) the contrast behavior is illustrated at $s = 0.07$. For higher ξ, a more noticeable contrast modulation is seen.

the equation used to fit the data acquired during this work, where we are able to rewrite equation 4.33 as the following total intensity expression:

$$I_T = 4I_a\left\{1 + \frac{1}{2}\,\mathcal{C}(\gamma,\xi)\; e^{-2(k\theta_0\sigma_z)^2(\theta-\theta_0)^2}\;\cos[2\theta_0 kh(\theta-\theta_0)-\delta]\right\} \tag{4.39}$$

This was only possible due to the first equality that I wrote (equation 4.34), which has the fringes' displacement δ present. Such equation was actually a comparison between equation 4.33 and equation (35) from reference [45]. In it, when discussing the intensity for the case of extended clouds of randomly distributed scatterers, within the linear regime just as considered here ($s \ll 1$), it was possible for the authors to write:

$$I(\boldsymbol{k}) \propto \{1 + e^{-2(k\theta_0 s_z)^2(\theta-\theta_0)^2}\cos[\Phi]\} \tag{4.40}$$

The difference from this equation to the right side of 4.34 is the factor δ, a geometrical phase that appears due to the nature of our experiment. As explained in the previous section, the light acquires this geometrical phase that affects the fringe's center, causing a displacement in it during our measurements, and is added here in the cosine term becoming $\cos[\Phi - \delta]$. This geometrical phase corresponds to the Pancharatnam-Berry's phase [21], [22].

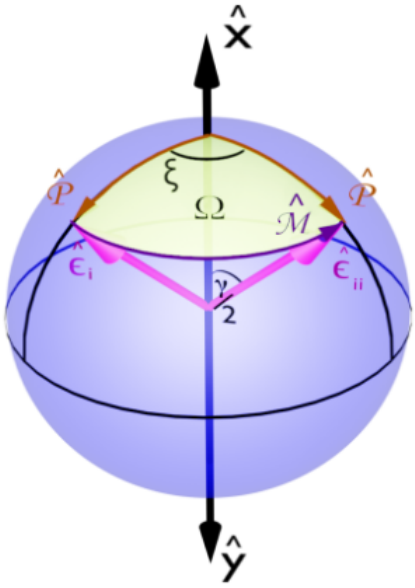

Figure 4.9: Representation in the Poincaré sphere of the light polarization ϵ_1 and ϵ_2, obtained after the action of the transformations $\hat{\mathcal{M}}$ and $\hat{\mathcal{P}}$ in direct or reverse order, respectively. The angles ξ and γ are defined by the operations $\hat{\mathcal{M}}$ and $\hat{\mathcal{P}}$, respectively, and the solid angle Ω is indicated in light yellow.

Pancharatnam-Berry's phase

Both physicists Shivaramakrishnan Pancharatnam (1934–1969) and Michael Berry (born 1941) investigated the same phenomena related to light polarization: the fact that a light field may suffer a geometrical phase shift due to its polarization suffering a cyclic transformation [46]. The difference lies on the nature of each interpretation. While Pancharatnam developed an arithmetic type of analysis, Berry created a geometrical one, in a sense that is possible to state the latter as a general example of the former.

There's no simple way to create an example for this concept but a great tool in order to achieve a visualization of such phenomena is through the Poincaré sphere, a geometrical representation of different states of polarization of your light field. Figure 4.9 shows such information to the specific case for our interferometer. A first step to illustrate this would be, picturing the Poincaré sphere alone, to imagine three random points in it: A, B and C. A polarization vector $\boldsymbol{V}$ could be interpreted as an arrow that points perpendicular to the sphere's surface, and the second step to visualize the phenomena of the Pancharatnam-Berry's phase would be to move this arrow through a closed loop (say $C \to A \to B \to C$, for instance). If that happens, the Pancharatnam-Berry phase states that the final state of the arrow, even though it has the same polarization as its initial one, has gained a global phase due to the geometrical path it travelled. At our experiment, this would be the scattered light being reflected by the 45° mirror twice and passing through the waveplate (for now, do not understand this as the order these transformations occur, but only as

the components responsible for our vector $\boldsymbol{V}$ going through the points A, B and C cited in this example).

Looking at figure 4.9, the two pink arrows that represents the polarization $\boldsymbol{\epsilon_i} = \boldsymbol{\epsilon_1}$ and $\boldsymbol{\epsilon_{ii}} = \boldsymbol{\epsilon_2}$ would be different vectors $\boldsymbol{V}$ at the example I've just mentioned. The question that both Pancharatnam and Berry ask themselves was: how different would the polarization $\boldsymbol{\epsilon_1}$ and $\boldsymbol{\epsilon_2}$ be from each other? Let's consider both transformations present at the system I worked with: $\hat{\mathcal{M}}$ and $\hat{\mathcal{P}}$. Considering the Jones formalism, when writing these transformations as matrices, we can also write that:

$$\boldsymbol{\epsilon_1} = \hat{\mathcal{P}} \circ \hat{\mathcal{M}}\hat{\boldsymbol{x}} \tag{4.41a}$$

$$\boldsymbol{\epsilon_2} = \hat{\mathcal{M}} \circ \hat{\mathcal{P}}\hat{\boldsymbol{x}} \tag{4.41b}$$

Notice how the polarizations are opposite to each other on their respective transformation order. Now, let's apply a new transformation $\mathcal{F} = \hat{\mathcal{M}}^{-1} \circ \hat{\mathcal{P}}^{-1}$, where $\hat{\mathcal{M}}^{-1}$ is the inverse of $\hat{\mathcal{M}}$ and $\hat{\mathcal{P}}^{-1}$ is the inverse of $\hat{\mathcal{P}}$. If we apply $\mathcal{F}$ to both polarization (which we are allowed to do so since when applying the same transformation $\mathcal{F}$ in both polarization, one will not gain any phase relative to the other) , we get:

$$\mathcal{F}\ \boldsymbol{\epsilon_1} = (\hat{\mathcal{M}}^{-1} \circ \hat{\mathcal{P}}^{-1}) \circ (\hat{\mathcal{P}} \circ \hat{\mathcal{M}})\hat{\boldsymbol{x}} = \hat{\mathcal{M}}^{-1} \circ \hat{\mathcal{M}}\hat{\boldsymbol{x}} = \hat{\boldsymbol{x}} \tag{4.42a}$$

$$\mathcal{F}\ \boldsymbol{\epsilon_2} = (\hat{\mathcal{M}}^{-1} \circ \hat{\mathcal{P}}^{-1}) \circ (\hat{\mathcal{M}} \circ \hat{\mathcal{P}})\hat{\boldsymbol{x}} \tag{4.42b}$$

It is worth to notice how, for $\boldsymbol{\epsilon_1}$ we ended up with the initial polarization $\hat{\boldsymbol{x}}$, while for $\boldsymbol{\epsilon_2}$ the result was the same vector $\hat{\boldsymbol{x}}$ but with a transformation applied to it, which means that $\boldsymbol{\epsilon_2}$ gained a phase when compared to $\boldsymbol{\epsilon_1}$ only due to the fact that their transformation matrices order are inverted. This relative phase is the Pancharatnam-Berry phase discussed in this section. Such global phase relative from one vector to the other creates a surface on this geometrical interpretation: the triangle $\boldsymbol{\epsilon_x\epsilon_1\epsilon_2}$ seen in figure 4.9. Both scientists discovered that the area from this triangle, the solid angle Ω represented in yellow in the figure, is related to the phase shift δ that $\boldsymbol{\epsilon_1}$ has with respect to $\boldsymbol{\epsilon_2}$, and can be equated as [46]:

$$\delta = -\frac{\Omega}{2} \tag{4.43}$$

And that is possible to measure if one make both these fields interfere with each other. Considering that such phase shift δ comes from the scalar product between the polarization, then it is possible to relate it with the contrast of the interference profile through the following equation:

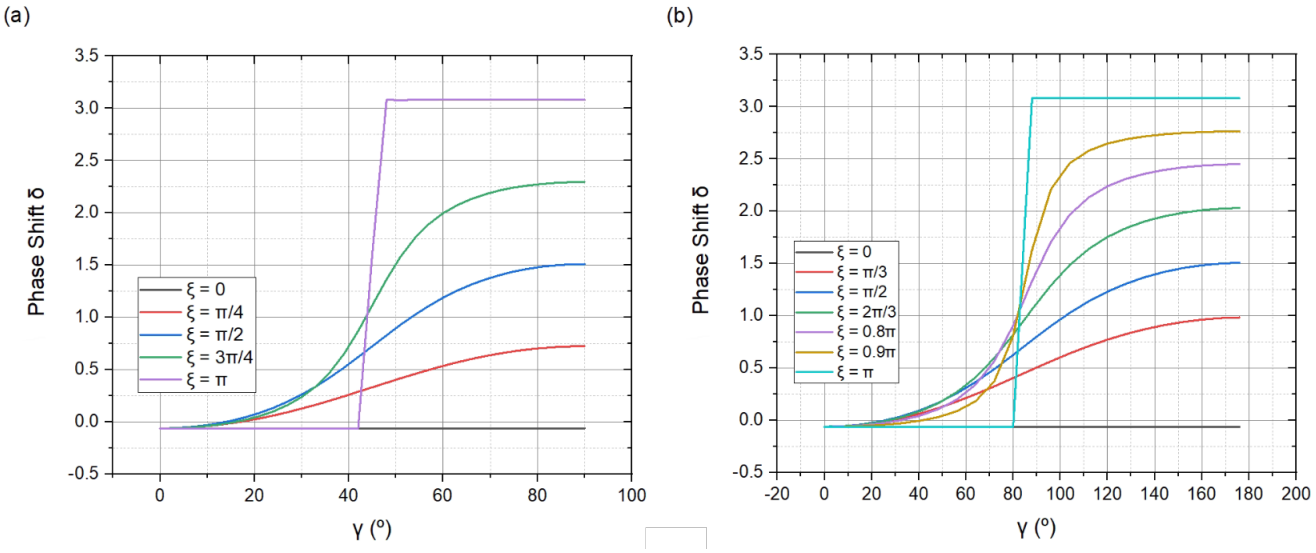

Figure 4.10: Both graphs outline the fringe's global phase δ behavior attributed to the polarization angle, which has a direct correlation to the factor γ. In (a), this behavior is depicted for a saturation parameter of $s = 0.0001$, while at (b) the global phase behavior is illustrated at $s = 0.07$. For higher ξ, a more noticeable phase δ is seen.

$$\langle \boldsymbol{\epsilon_1}, \boldsymbol{\epsilon_2} \rangle = \mathcal{C} e^{-i\delta} \tag{4.44}$$

It is then possible to relate that with equation 4.38 and discover that the expression that best describes the geometrical phase related to the Pancharatnam-Berry phase is:

$$\tan\delta = \frac{\sin\xi \ \tan^2\gamma}{1 + \cos\xi \tan^2\gamma} \tag{4.45}$$

Therefore, this global phase shift δ also is affected by the factors ξ and γ. Figure 4.10 showcase this dependence, just as the one related to the contrast. Yet again it is possible to notice the dependence on the saturation parameter s, which brings our discussion to the next subsections: the corrections needed on the total intensity equation in order to correctly describe the phenomenon that happens in our experiment.

Saturation Parameter Correction

During the calculations, I've stated we must consider that the system resides in the linear regime, $s \ll 1$, so that the total electrical field could be described by equation 4.2. This statement still holds to be true, but even though the linear regime is granted to our system, it is not as linear as to assure negligible effects, so a small correction on the intensity is needed. This correction is related to the contrast and it can be better understood if the reader goes back to figure 4.8. In it, it is possible to see two different graphs that explore two cases of the saturation parameter:

$s = 0.001$, which configures an exclusively linear regime ($s \ll 1$), with no other effects occurring, and $s = 0.07$, the one at our experiment.

For $s = 0.001$, one may notice that if the value of the factor ξ changes, a modulation on the contrast C becomes apparent. The physical aspect related to such effect is that as the relative phase shift induced by the dielectric mirror gets higher, the worst the detection of the fringes becomes, specially when $\gamma \approx 45°$. For this case, it is possible to notice that the equations for polarization $\boldsymbol{\epsilon_1}$ and $\boldsymbol{\epsilon_2}$, provided earlier in this text, reach a specific condition:

$$\boldsymbol{\epsilon_1} = \cos\gamma\ \boldsymbol{\epsilon_x} + \sin\gamma\ \boldsymbol{\epsilon_y} \rightarrow \boldsymbol{\epsilon_1} = \frac{1}{\sqrt{2}}\left(\boldsymbol{\epsilon_x} + \boldsymbol{\epsilon_y}\right) \tag{4.46a}$$

$$\boldsymbol{\epsilon_2} = \cos\gamma\ \boldsymbol{\epsilon_x} + \sin\gamma\ e^{i\xi}\boldsymbol{\epsilon_y} \rightarrow \boldsymbol{\epsilon_2} = \frac{1}{\sqrt{2}}\left(\boldsymbol{\epsilon_x} + \mathrm{e}^{i\xi}\boldsymbol{\epsilon_y}\right) \tag{4.46b}$$

Where now the effect of the added phase ξ reaches its maximum, causing the highest modulation in the contrast, as seen in 4.8a. At the same time, if we investigate what happens for $\gamma \approx 90°$, we see that:

$$\boldsymbol{\epsilon_1} = \boldsymbol{\epsilon_y} \tag{4.47a}$$

$$\boldsymbol{\epsilon_2} = e^{i\xi}\boldsymbol{\epsilon_y} \tag{4.47b}$$

Where, following equation 4.44, provide us with the information of $\mathcal{C}$ being maximum (in other words, not receiving any modulation), but simultaneously the fringes acquiring a maximum value in the shift δ, as also seen in figures 4.8a and 4.10a.

In section 3.5, I discussed both elastic and inelastic scattering regimes throughout the interference phenomena, and how the intensity profile from it is affected by the saturation parameter s. Here, this relation becomes relevant since it explains that for a saturated regime, we obtain a behavior mostly inelastic, with that causing an effect of diminishing the contrast. But that not only appears on a saturated regime, but also on the linear regime we encounter at our experiment. When comparing 4.8a and 4.8b, it is possible to see that the contrast for the case of our experiment ($s = 0.07$) presents an overall lower value than the one at the expressively linear regime ($s = 0.001$).

Taking such consideration into account, the small correction I mentioned earlier appears as the contrast becomes a function of the saturation parameter s and of the time delay τ_c related to the sections A' and B', seen in figure 4.7a. The dependence on the time delay also comes from the discussion made in section 3.5. Essentially, light is inelastically scattered, i.e., presents a

broadening of the spectrum when compared to the incoming original one due to the finite saturation parameter, the so-called Mollow triplet cited in that section, and the scattered light that travels through path B' undergoes a coherence loss with respect to the scattered light following path B. This would be the physical explanation for why the contrast becomes a function of s and τ_c. Mathematically, on the other hand, we must consider that the saturation parameter s_1 seen by one single atom at position z is given by [45]:

$$s_1(z) = 2s\left[1 + \cos\gamma\,\cos\left(2k\cos\theta_0 z\right)\right] \tag{4.48}$$

At the same time, it is possible to write the first order correlation function $g_z^{(1)}(\tau_c)$ as a function of this saturation parameter (and therefore the position z), where in the RWA it can be given by [45]:

$$g_z^{(1)}(\tau_c) = \frac{1}{1+s_1(z)} + \frac{1}{2}\left[\mathrm{e}^{-\Gamma\tau_c/2} + \frac{s_1(z)-1}{s_1(z)+1}\cos\left(\Omega_M(z)\,\tau_c\right)\mathrm{e}^{-3\Gamma\tau_c/4} + \frac{\Gamma}{4\Omega_M(z)}\frac{5s_1(z)-1}{s_1(z)+1}\sin\left(\Omega_M(z)\,\tau_c\right)\mathrm{e}^{-3\Gamma\tau_c/4}\right] \tag{4.49}$$

Which is the Fourier transform of equation 3.58, showcasing the direct link between the first order correlation function and the Mollow Triplet. Through some further more algebra, it is possible to find the following equation for the total intensity scattered by this single atom:

$$I_1(\mathbf{r}_j) \;=\; 4I_1\left[2 \,+\, \tilde{g}_z^{(1)}(\tau_c)\,\cos\left(2kz\cos\theta\right) \,\times\, \frac{2\cos\gamma \,+\, \cos\left(2kz\cos\theta_0\right) + \mathcal{C}\cos\left(2kz\cos\theta_0+\delta\right)}{1 \,+\, \cos\gamma\,\cos\left(2kz\cos\theta_0\right)}\right] \tag{4.50}$$

As done earlier on this section, we now integrate such intensity profile over a gaussian atomic distribution, obtaining for the whole cloud:

$$I_T = NI_a\left\{1 + \frac{1}{2}\mathcal{C}_s(s,\tau_c,\gamma,\xi)\,e^{-2(k\theta_0 s_z)^2(\theta-\theta_0)^2} \times \cos[2\theta_0 kh(\theta-\theta_0)-\delta]\right\} \tag{4.51}$$

Where now the contrast has been corrected for the finite saturation parameter s considered in our system (the expression of the contrast $\mathcal{C}_s(s,\tau_c,\gamma,\xi)$ as given in eq. 4.51 has no analytical form in general, and is found by numerical integration of eq. 4.50).

Optical Density correction

The final additional correction to the total intensity equation is the one related to the optical density b_0 of our system. Opposing to the correction related to s, here path I is explored. Such occurring happens since, in this path the field attenuation tend to be less when compared to the others, due to its smallest length inside the atomic cloud. But since path I contributes to the background intensity, a correction is in fact needed. Due to the fact that our parameter s keeps the system under the linear regime, and at first order it is possible to equate the contrast attenuation as a factor $1 - b_0$ [15], it is then possible to write the final expression that it was used to fit the data acquired in this thesis:

$$I_T = NI_a\left\{1 + \frac{1}{2}\,(1 - b_0)\,\mathcal{C}_s(s, \tau_c, \gamma, \xi)\; e^{-2(k\theta_0 s_z)^2(\theta-\theta_0)^2}\cos[2\theta_0 kh(\theta - \theta_0) - \delta]\right\} \tag{4.52}$$

4.4 Interferometric Setup

Our interferometric setup, as described earlier in this text, is constructed based on the model of an mCBS system. Figure 4.11a illustrates the installation of this system in our experiment, where the reader can identify the set of lenses with focal distance $f = 150$ mm. These lenses are responsible for creating the virtual mirror. Using such concept, we can project the necessary mirror as close as possible to our cloud without the light path being altered as so to change the phenomena we want to observe. Figure 4.11b demonstrates explicitly how this non-alteration of the phenomena observed and described thus far is preserved. The implementation of the virtual mirror is necessary due to the conditions of our experiment, where the samples provided by it are inside our vacuum-sealed science chamber, making it impractical to physically insert a mirror as close as possible to our atomic cloud.

A photo of how this was installed in our experiment can be seen in figure 4.12. It is worth to notice that, due to the fact of our mirror being installed in a translation mount, it was possible to characterize the distance h between the virtual mirror and the atomic cloud (since is dependent on the distance d between the mirror and the second lens), finding $h = 10.46$ mm for the RedMOT and $h = 11.41$ mm for the BlueMOT. These values provided the best fringes envelope for our interferometer, with $3.6° < \theta < 3.8°$ for the RedMOT and $4.1° < \theta < 4.3°$ for the BlueMOT, meaning that these intervals provided a clearer discernment of the fringes when compared to other values of h.

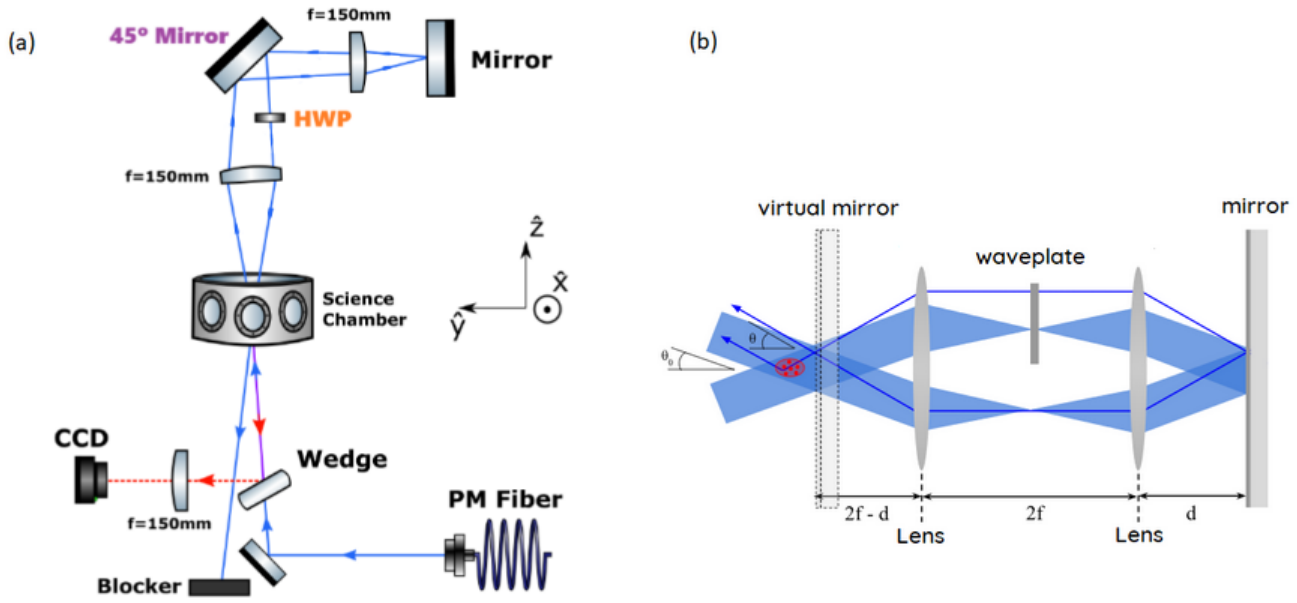

Figure 4.11: At (a), a schematic of the mCBS interferometric setup installed at our experiment. The blue continuous line represent the laser light, while the red dashed one represents the light scattered by our cloud. The purple segment represent the part of the path that both lights are present. At (b), a schematic of the same system is presented, showing how the interference phenomena is preserved when adding the virtual mirror, a necessary step in order to achieve a mirror as close to the cloud as the mCBS recquires.

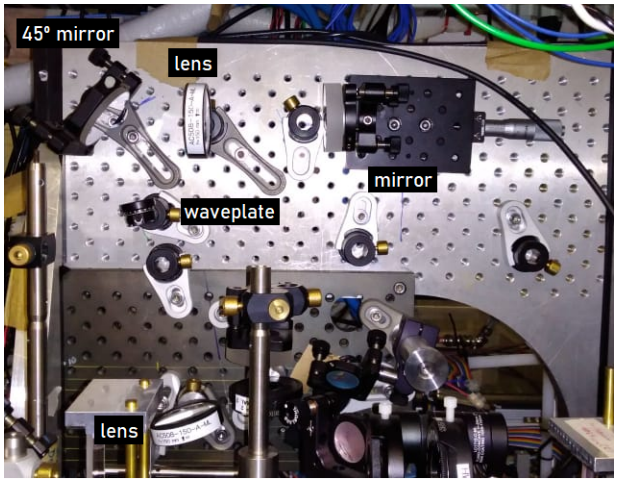

Figure 4.12: Photo of our experimental setup with the main components responsible for the optical paths indicated and named. The fact that the mirror is installed in a translation mount provided the possibility to characterize the distance h between the virtual mirror and the atomic cloud.

In order to illuminate our whole atomic sample with uniform light intensity and observe the phenomena calculated, a beam waist of $w_0 = 2.1$ mm was chosen. Also, due to the fact that we wanted to observe this at the linear regime, that is, $s \ll 1$, the beam power was chosen to

be 0.2 mW. The reason is that we consider the so called saturation intensity I_{sat}, related to the saturation parameter through $s = I/I_{sat}$. Since I_{sat} is a function of the resonance transition ω_0 and the transition linewidth Γ, then it is possible to calculate such value for each of our MOT's transitions, obtaining 40.74 mW/cm^2 for the 461 nm transition and 3.04 μW/cm^2 for the 689 nm one. Giving that the interferometer uses a 461 nm beam and a power of 0.2 mW, it provided the already mentioned saturation parameter value of $s = 0.07$ for our system. As seen, such value was enough to assure the desired linear regime of $s \ll 1$, but it wasn't enough to prevent some few effects to be noticeable, explaining the correction demonstrated in the last section.

Another important characterization is the one related to the waveplate, optical component responsible for the factor γ. Since this component is also responsible for the change in the polarization of the reflected beam, this means that the characterization takes into account the polarization from the incoming beam, chosen to be linear. In this characterization, linear polarization can be defined as either horizontal or vertical. To set the system as controllable as possible, we set the incoming beam polarization to be vertical. Six different angles for the reflected beam with respect to the incoming one were characterized, each corresponding to a specific value of the factor γ. The range spans from $\gamma = 0°$, representing vertical polarization, to $\gamma = 88°$, denoting practically horizontal polarization for the reflected beam (which would happen for $\gamma = 90°$).

The remaining characterization of this section is about the phase factor ξ the beam's polarization suffers when reflected twice by the dielectric mirror. A Shäfter und Kirchhoff polarization analyzer (model SK010PA-VIS) was used in order to gather such information. The obtained result reveals a value of $(81 \pm 5)°$ for a single reflection at the 45° mirror, denoting the extent of phase variation experienced by the orthogonal components. The determined value for ξ, thus, is found to be $(162 \pm 10)°$, taking into account the fact that the incident light undergoes two successive reflections from the mirror surface.

4.5 Experimental Sequence

From chapter 2 the reader learned that we have two main samples: the RedMOT and the BlueMOT. Both of them were used as to try and analyse the circular fringes of our interferometer. Since, at that chapter, I've explained the sequence to obtain the absorption images, here I'll do the same to explain the sequence to obtain the fringes image. Luckily, the sequence is basically the same with only the image treatment (and of course what is captured) changing. So, at figure 4.13 the reader will see almost the same as in figure 2.11.

Keeping the same name for the images (Atoms, Probe and Dark), we still have the same evaluation and concept for each one of them: the first having the cloud and the incoming laser beam, the second having only the beam and the third all the residual environmental light. But, another thing related to the interferometer beam is that it is in resonance with our Sr atoms (461 nm, the blue transition). This means that if the beam illuminates the cloud long enough, it

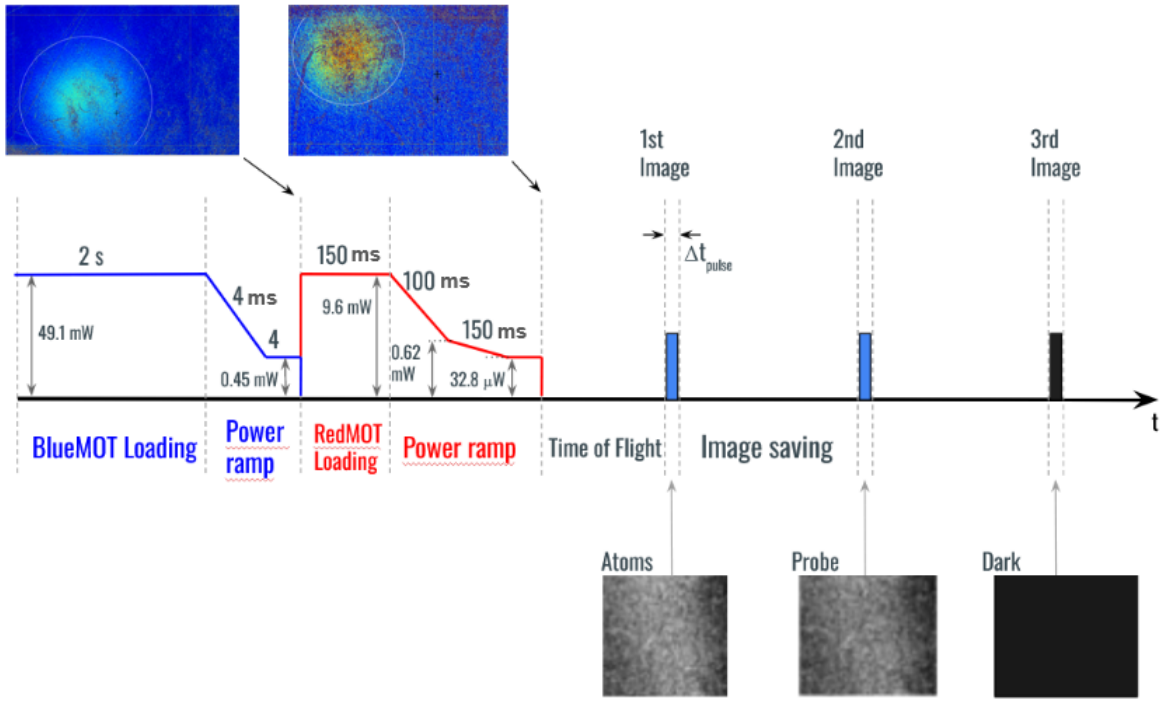

Figure 4.13: Interferometer experimental sequence schematics. We first load our samples (BlueMOT or RedMOT) and then, after specific ToF for each one of them, probe the interferometer beam

Source: [40]

can destroy it: by resonating with the cloud, the beam can create accelerations in the cloud that not only displace it but also expand it. The new created accelerations have the power to shift the cloud, therefore bringing our sample to regions with different Rabi frequencies that may kill the contrast, while on another aspect it can also bring the cloud out of resonance due to the Doppler effect resulting in not only a decreased signal but also invalidating the entire model discussed so far.

To prevent the effects stated at the former paragraph, we have developed a criterion for characterizing the pulse duration of the interferometer beam. It involves analyzing six different accelerations that are created due to each phenomena the cloud encounters: three related to its expansion and other three related to its displacement (paired to each one of the spatial axis). The plan is to probe the cloud with the interferometer beam, measure the six created accelerations and find the maximum pulse duration Δt_{pulse} that still avoids such destruction of both the contrast and the cloud.

To achieve this information, what was done was to measure both the cloud width and center of mass position for different time intervals Δt taken after the ToF seen at figure 4.13. To put it simply:

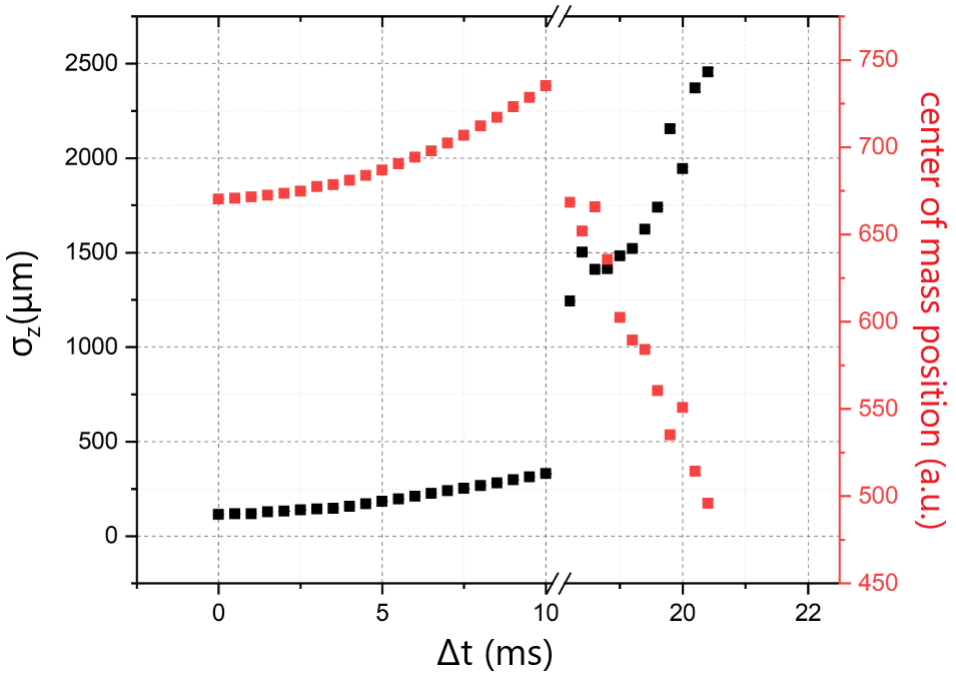

Figure 4.14: Example of acceleration measurement of our cloud due to interaction with the interferometer beam. Both width σ and center of mass position were measured for different Δt time intervals. For this specific measurement, a pulse of $\Delta t_{pulse} = 2$ µs and a power of 10 mW were used. For the pulse used in this thesis, the best value found was $\Delta t_{pulse} = 70$ µs, for a power of 0.2 mW.

Source: [40]

1. After creating the MOTs, we wait a fixed ToF = 15 ms so that the samples are the ones considered in figure 2.13.

2. We probe the cloud with the interferometer beam for a pulse duration of Δt_{pulse}, that changes for each measurement taken.

3. Then we wait the time interval Δt, after the pulse, in order to evaluate the cloud's evolution (both its center of mass position and its width).

These three steps provided what can be seen at figure 4.14, and it was taken for different Δt_{pulse} values. Afterwards, we calculate the derivative of each part of the curve in order to find the velocity of both aspects of our cloud (before and after the beam) and then be able to calculate its accelerations. The best values for these accelerations were the ones that keep the cloud from reaching limits set by our group due to experimental characteristics, such limits being: either the time that it takes for the cloud to be shifted by 0.3 Γ of the 461 nm transition or the time that it takes for both the cloud's position and/or size to be increased by a factor of 20%. This limit varies for each beam intensity, and for our power of 0.2 mW, we found that the best value for our pulse

is $\Delta t_{pulse} = 70$ µs. A more detailed characterization of this parameter considering other values of laser power can be found in [40].

However, what exactly do we capture from our system? Initially, a CCD camera is used in order to collect the light scattered in the backward direction, corresponding to the path B as illustrated in Figure 4.7. This light undergoes a shift by $2\theta_0 = 8.6°$ from the direction of the reflected beam, as to minimize the impact of stray light. A lens with a focal distance of $f = 150$ mm acts to conjugate the far-field scattering profile at its focal plane, where the camera is positioned to capture the field. When the image is precisely captured at the lens's focal plane, the angle formed by a specific beam and all its parallels with the lens normal translates into a distinct position, which is illustrated by figure 4.15b. If we denote the position in the focal plane as x and the angle as θ, the relationship can be expressed as $x = f\theta$. This equation allows us to ascertain that each pixel in the camera corresponds to a change of 0.0014° in the scattering angle θ.

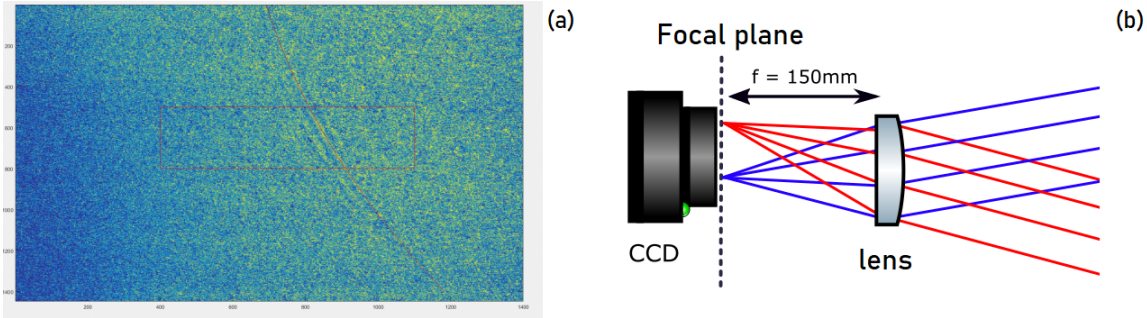

Figure 4.15: (a) Fringe's image obtained at our experiment after an average of 1230 images. (b) representation of our fringe's image capturing technique. Light scattered by our cloud at different angles θ(represented both in red and blue), reaches different positions x at the CCD camera. This allowed us to determine that our camera resolution: each pixel was equivalent to a change of 0.0014° in the scattering angle.

The final step to enlighten our experimental sequence involves determining how to obtain only the scattered light from the three captured images. Matrices corresponding to each of the images are generated through sequences developed by our research group using both LabView and Matlab. Such matrices can be determine as, in reverse order of capturing:

- M_{Dark}: matrix of the third image, represents the background noise.
- $M_{Probe} = M_{beam} + M_{Dark}$: matrix of the second image, it contains the sum of the matrix representing the interferometer beam light (M_{beam}) and matrix M_{Dark}.
- $M_{Atoms} = M_{fluo} + TM_{beam} + M_{Dark}$: matrix of the first image captured, contains the sum of the matrix representing the atomic fluorescence M_{fluo} (what we aim to acquire, since it represents light scattered by the cloud), and both matrices M_{beam} and M_{Dark}. Here, M_{beam} is multiplied by a transmission factor $T < 1$, due to the beam going through the cloud.

The goal is to acquire information that matrix M_{fluo} carries (atomic fluorescence). For that to be accomplished, a series of operations are performed along the matrices I just have described. First, is important to realize that these matrices carry information about every light present in our experiment, and we want to acquire only the light scattered by the atoms. In order to do that, a necessary step is to remove the background noise from the first two images, which give us the following new two matrices:

$$M_1 = M_{Atoms} - M_{Dark} \tag{4.53a}$$

$$M_2 = M_{Probe} - M_{Dark} \tag{4.53b}$$

An important aspect of these new matrices is that, even though the background noise is removed, the stray light of the interferometer beam itself is still present. While in matrix M_1 this light exists, it is attenuated since the atoms in our sample absorb an amount of it. In matrix M_2, on the other hand, such stray information is not attenuated. A linear fit outside the fringes region may solve that. Out of the spatial location where the fringes appear, the light scattered by the atoms has a constant value. At the same time, in this region, the stray light of the interferometer beam is not isotropic, but centered around the direction of k_0' (reflected beam). Due to this behavior, the linear fit of this region can be read as:

$$M_1 = F + TM_2 \tag{4.54}$$

where both $F > 0$ and $T > 0$ are parameters related to background fluorescence and transmission coefficient of the reflected beam through the cloud, respectively.

From this fit, it is possible to obtain information on the fringes region itself, which is given by the following expression:

$$M_{fluo} = M_1 - TM_2 \tag{4.55}$$

Such equation provides a two-dimensional profile of the atomic fluorescence along the fringes. However, if we consider only one fringe image, the signal intensity is insufficient for distinguishing it from the background noise. To ensure this does not affect the signal-to-noise ratio, we take an average of at least 1000 images. Which the result of this average is shown in figure 4.15a. At the same time, we can extract from this image the information about our intensity profile with respect to the scattering angle due to the $2D$ profile provided by equation 4.55. To do this, we first find the center of the circular fringes. Then, an azimuthal average is performed, and that allows us to plot an intensity profile with respect to the scattering angle, as shown in figures 4.16 and 4.17 at

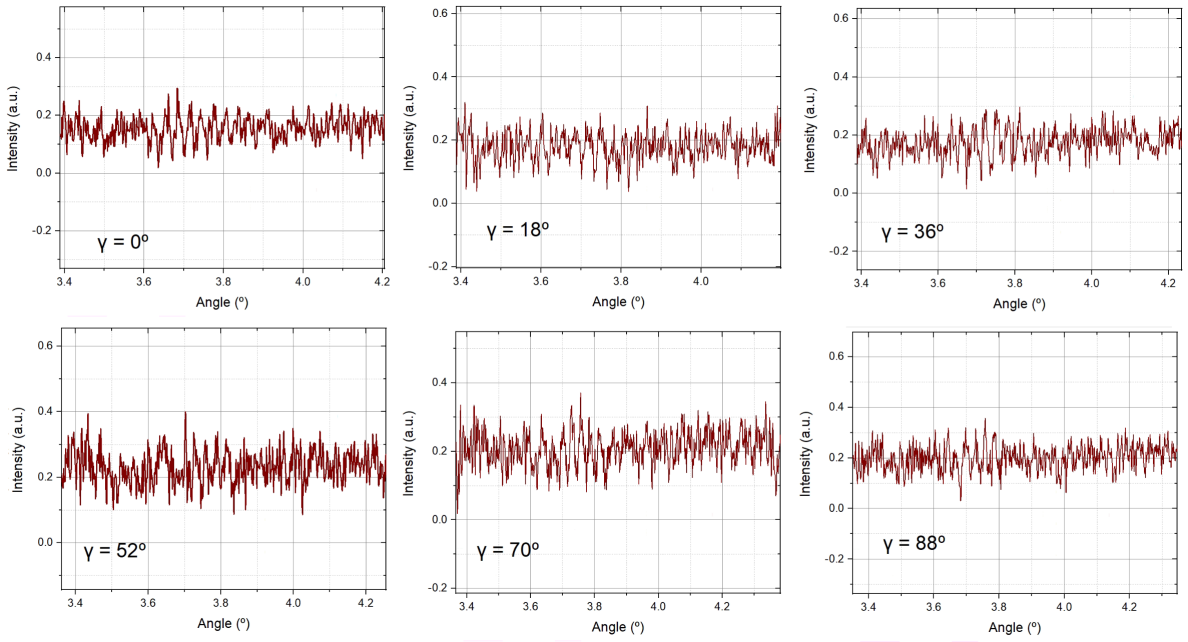

Figure 4.16: Intensity, in arbitrary units, versus the scattering angle θ, using the RedMOT, for each one of the waveplate angles characterized in this work. The small size of the cloud had its advantages, but due to the low number of atoms, it provided a bad signal-to-noise ratio.

the next section. Thus, all that is needed in order to evaluate and analyse the data obtained in this thesis' measurements is presented and now we move forward to the results discussion.

4.6 Results

As figure 4.15a shows, that is the result of after 1000+ images averaged in order to obtain one specific image. At the previous section, I also stated that in order to investigate the intensity profile, an azimuthal average is done. The result image of this azimuthal average can be seen in figure 4.16. As the reader may notice by the graphs presented, it was quite a challenge to get a good signal-to-noise ratio using the RedMOT. This sample was of interest to investigate such phenomenon discussed in this work since its size was enough to ensure that both incoming and reflected electric fields from the laser beam have constant amplitude when interacting with the cloud. It turns out, however, that such cloud characteristic was not as meaningful as the number of atoms N. Giving that the BlueMOT offers an order of magnitude of N higher than the RedMOT, way better fringes for each one of the waveplate angles were possible to be measured, as show in figure 4.17.

The subsequent step involved fitting these curves to extract information regarding the contrast. As detailed in section 4.3, the expression used for this fit was equation 4.52, with the resultant image of this procedure presented in figure 4.18. In it, fringes for each value of γ is depicted in a different color, and shifted vertically for easier visualization. A dashed vertical line is traced to demonstrate the displacement δ that happened in the center (θ_0) of the fringe's envelope, and as

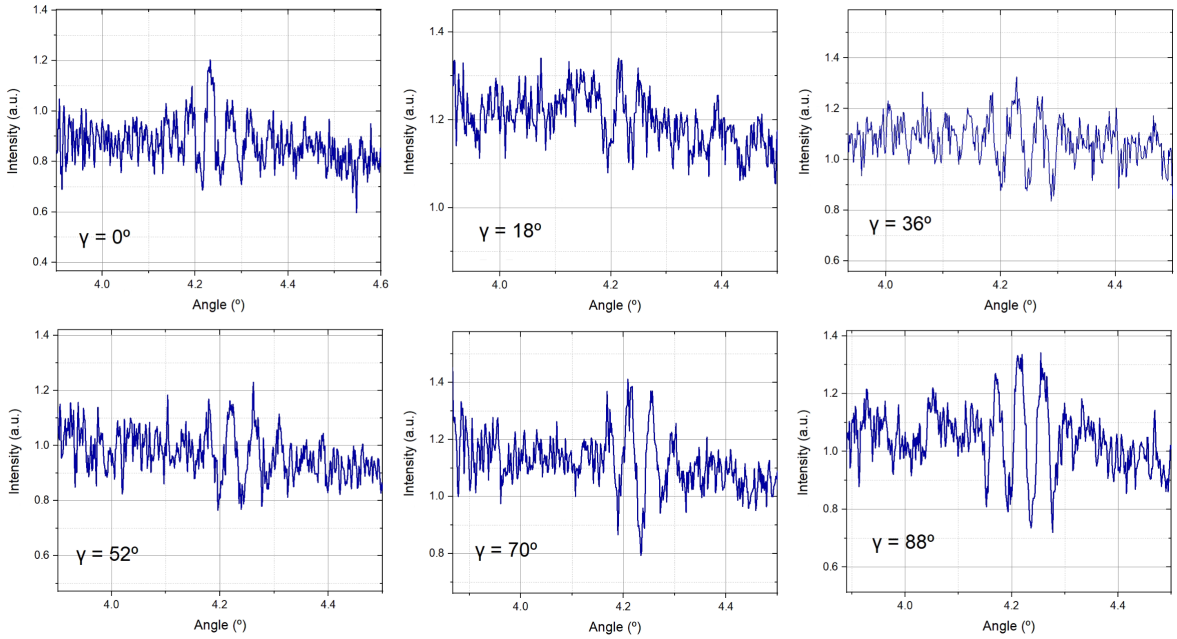

Figure 4.17: Intensity, in arbitrary units, versus the scattering angle θ, using the BlueMOT, for each one of the waveplate angles characterized in this work. Due to a order of magnitude higher in the number of atoms, the signal-to-noise ratio was much better, providing fringes with higher contrast.

discussed in the same section, is related to the Pancharatnam-Berry's phase.

From figure 4.19b, it is possible to notice how the measurement of the Pancharatnam-Berry phase δ presents a fair agreement with equation 4.45. Although the experimental data presented shows considerable error bars, the fact is that they arise from the noticeable uncertainty on the determination of θ_0 as γ approaches 45°. This uncertainty is due to the fact that close to $\gamma = 45°$, the contrast is too low and the phase of the fringes is badly identified, which is possible to observe in figure 4.19a. Nonetheless, a good agreement with the theory is present, specially if one considers not only the finite saturation parameter s that happens at our experiment but the also non-negligible OD of our cloud, $b_0 \sim 0.4$. When both factors are taken into account, it is possible to notice how well the theory describes the experimental data detected; we also note that the phase shift at $\gamma = 90°$ with respect to $\gamma = 0°$ is clearly seen from our data.

All of which can be explained by the break of reciprocity in such system. As seen, only paths II and III configure the paths responsible for the fringes, while paths I and IV actually describes the background intensity. At first glance, due to its geometry, one could intuitively think that paths II and III would be reciprocal, and one would be right to think so, if experimental properties such as the phase shift ξ, added by the dielectric mirror, didn't play a significant role in this research. Since that is not that case, these factors (ξ and γ) influence our interferometer in a way that breaks such reciprocity, which is mathematically explained by the non-commutation of the

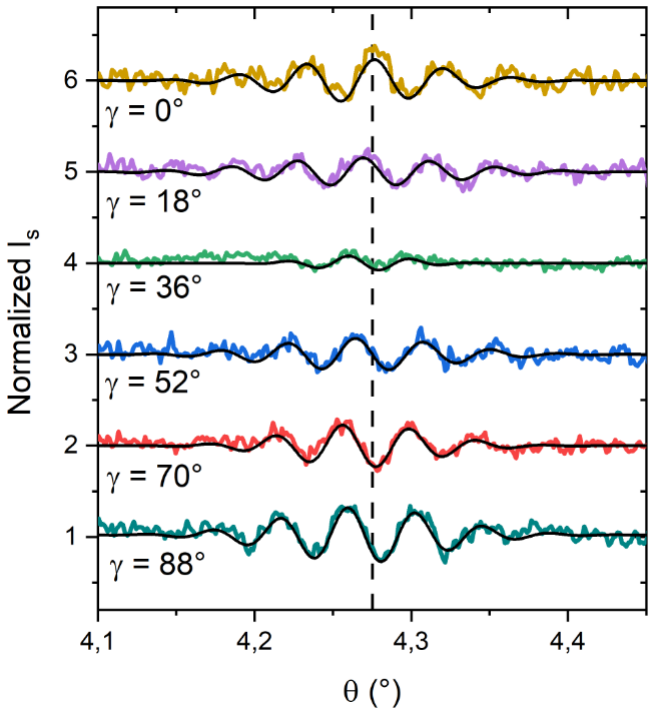

Figure 4.18: BlueMOT fringes organized in a single graph (shifted vertically by one for visibility) so to highlight not only their contrast but also the shift in the center's position. The colored lines represent the integration over the azimuthal direction, normalized to the background intensity, while the black continuous line represent the fitted profile following eq 4.52. The dashed vertical line is a tool to illustrate how the center of the fringes' envelope suffers the δ shift mentioned at the text.

polarizing optics.

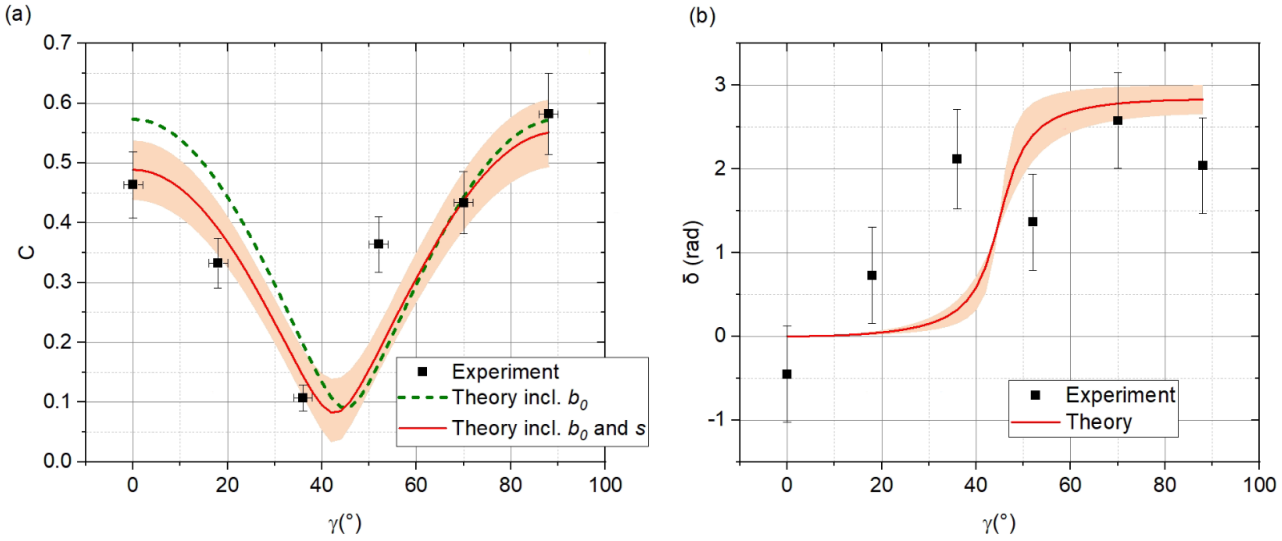

Figure 4.19: Graphs of both the contrast (a) and fringe's phase shift δ (b) over factor γ. The black squares represent the experimental data, the continuous red line represent the fit following equation 4.52, while the green dashed line on the contrast shows the behavior with only the finite optical density correction applied. The red shaded area corresponds to the theory confidence interval. An uncertainty is present around the region of $\gamma = 45°$, but such uncertainty also affects the error bars, which doesn't necessarily means a disagreement with the calculations presented in this thesis.

Chapter 5

CONCLUSION

Interference phenomena, including Anderson localization of light [47], [48], coherent backscattering [49], [50], and superradiance [51], are intricately linked to the interference patterns arising from light scattered by a disordered assembly of cold atoms. Most of these systems relies on the optical path's reciprocity, which in a optical system may be understood as the transformations two waves suffer when travelling along the same path, yet in opposite directions. Consequently, disrupting this reciprocity provides a way to control and manipulate these interference phenomena.

Within the context of this work, the disruption of optical path reciprocity within a mirror-assisted coherent backscattering setup (mCBS), where the light scattered by a large cold atomic cloud interfere with that from its mirror image, was investigated. Through non-commuting polarizing optics (such as a birefringent mirror and a half-waveplate), presents in the light's path, it was possible to observe that the fringes emanating from a disordered cloud of cold atoms experienced a reduction in contrast, as the polarization transformation cease to commute, rendering the two interfering paths related to the fringes in this setup being nonreciprocal.This breaking of reciprocity unveils a geometric interpretation on the Poincaré sphere, wherein the fringes' amplitude correlates with the geodesic distance between polarizations, while their angular displacement reflects the phase difference, aligning with Pancharatnam and Berry's concept.

This study used intricate details of both the intensity profiles and fringes in two different clouds of interest: the magneto-optical trap (MOT) based on the 689 nm transition and on the 461 nm one. The initial challenge was evident in achieving a favorable signal-to-noise ratio with the 689 nm, prompting a shift to the 461 nm, which demonstrated superior results due to a significantly higher number of atoms.

The subsequent focus was on fitting the measured curves and understanding the contrast reduction and the phase shift δ experienced by the fringes, related to polarization changes. This involved relating these shifts to the effects to the two polarization transformations, of the half-waveplate and the reflection by a 45° dielectric mirror. The linear scattering regime and corrections necessary for it were crucial aspects considered in the analysis. The results indicated distinct behaviors in contrast modulation and phase shift, emphasizing the impact of experimental parameters. The analysis extended to exploring the Pancharatnam-Berry phase, revealing a geometrical interpretation through the Poincaré sphere. The Pancharatnam-Berry phase (δ) was determined and compared with the experimental data, showcasing agreement with theoretical predictions despite uncertainties in determining certain parameters. Finally, the study elucidated how the break of reciprocity in the system, influenced by factors like finite optical density and saturation parameter,

played a pivotal role. The non-commutation of polarizing optics, illustrated through the matrix opperators $\hat{\mathcal{M}}$ and $\hat{\mathcal{P}}$, emphasized the dependence of reciprocity on specific values of γ and ξ.

In a broader context, the experimental findings presented in this study underscore the vectorial nature of light as a powerful tool for manipulating the reciprocity of interfering paths. This manipulation has a direct impact on the interference itself, all while preserving spectral and spatial coherence. This phenomenon closely parallels what occurs in multiple scattering regimes, exemplified by Anderson localization and Coherent BackScattering (CBS), particularly when time reversal symmetry is disrupted [52], [53], [54]. It is crucial to note that the interferometric system employed in this thesis, with its emphasis on the relevance of the light path to the mirror, facilitated the exploration of non-reciprocity. This stands in contrast to systems like Anderson Localization and CBS, where all light paths reside within the atomic cloud. The mirror-assisted Coherent BackScattering (mCBS) configuration offers a distinctive setup, enabling the straightforward introduction of noncommutative optics.

In essence, the experimental results highlight the intricate interplay of experimental parameters and system characteristics, providing valuable insights into the phenomena under investigation. The agreement between theoretical predictions and experimental data, despite uncertainties, validates the robustness of the study and opens avenues for further exploration in this complex and nuanced research domain.

Appendix A

TEMPERATURE MONITORING CIRCUIT

During this thesis, I developed a temperature monitoring circuit for our laboratory, a complementary project that would enhance our level of control (or at least monitoring) over yet another variable surrounding our experiment. This initiative necessitated a comprehensive command not only of the nuances associated with circuit board design using Autodesk' Eagle software but also a profound comprehension of the operational knowledge intrinsic to Arduino microcontrollers, PCB (Printed Circuit Board) designs, and temperature sensors. This extra chapter explores the concepts of each component and the logic behind their integration, providing a more profound understanding of the comprehensive design and its scientific foundations.

Figure A.1: Photo of the final project modules operating at our lab. The circuit functions through two distinct modules: Arduino and Mux. The Arduino Module not only accommodates the Arduino component but also includes the supply voltage regulator. In contrast, the Mux Module houses the multiplexer and the MAX6675 temperature sensor. These modules are interlinked through Molex connectors, facilitating troubleshooting efforts for each module individually.

The general concept of this project revolves around the acquisition of temperature data facilitated by the MAX6675 temperature sensor. These sensors are equipped with type K thermocouples, thereby enabling the conversion of thermocouple-induced voltage into precise digital temperature values. The temperature range of said sensor goes from 0 °C to +700 °C with a resolution of 0.25 °C, more than enough to assure the accuracy and reliability of temperature measurements at our laboratory.

Following the meticulous temperature data collection, the next step is the online visualization of this information through ThingSpeak, an Internet of Things (IoT) analytics platform integrated

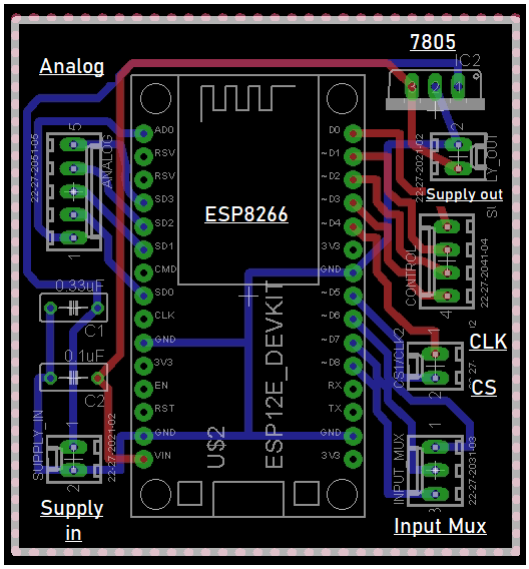

Figure A.2: Schematic of the Arduino Module PCB. This module accomodates the ESP8266 NodeMCU (micro-controller responsible for this circuit operation), an LM7805 voltage regulator (responsible for distributing the power for all components), and the necessary connections for controlling the Mux Module, such as: analog pins (which comunicate to the multiplexer which pin the circuit should read and its reading) and both the CLK and CS pins of the MAX6675 sensors. This module is powered by a Minipa Power Supply.

seamlessly with Matlab. This integration introduces sophistication to the data analysis process, providing a dynamic platform for real-time visualization and comprehensive analytics. To execute this task, the ESP8266 NodeMcu Arduino microcontroller variant plays an important role due for its Wi-Fi communication capability. This wireless feature establishes a seamless connection between the temperature monitoring system and ThingSpeak, facilitating real-time transmission, visualization, and analysis of experimental parameters (in our case, the temperature, but this can be done for multiple variables such as humidity for instance, it only depends on the sensor one works with). This communication link enhances the scientific rigor of the temperature monitoring framework.

To achieve the goal of gathering data with the MAX6675 sensors and subsequently visualizing it online through ThingSpeak, the first step was to learn how to design PCBs and to fabricate them. PCB design is not a one-size-fits-all process; it is contingent on the specific components used. For our temperature monitoring circuit, the optimal approach was to create a PCB that operates through two distinct modules: the Arduino module and the Mux module. The Arduino module, with its circuit schematic depicted in figure A.2, accommodates the ESP8266 NodeMcu, an LM7805 voltage regulator, and essential circuitry. In contrast, the Mux module (figure A.3, incorporates a multiplexer, the MAX6675 temperature sensors, and their associated circuitry. These modules are interconnected via straightforward molex extensions, offering modularity and facilitating easy separation for diagnostic or maintenance purposes. This modular design enhances

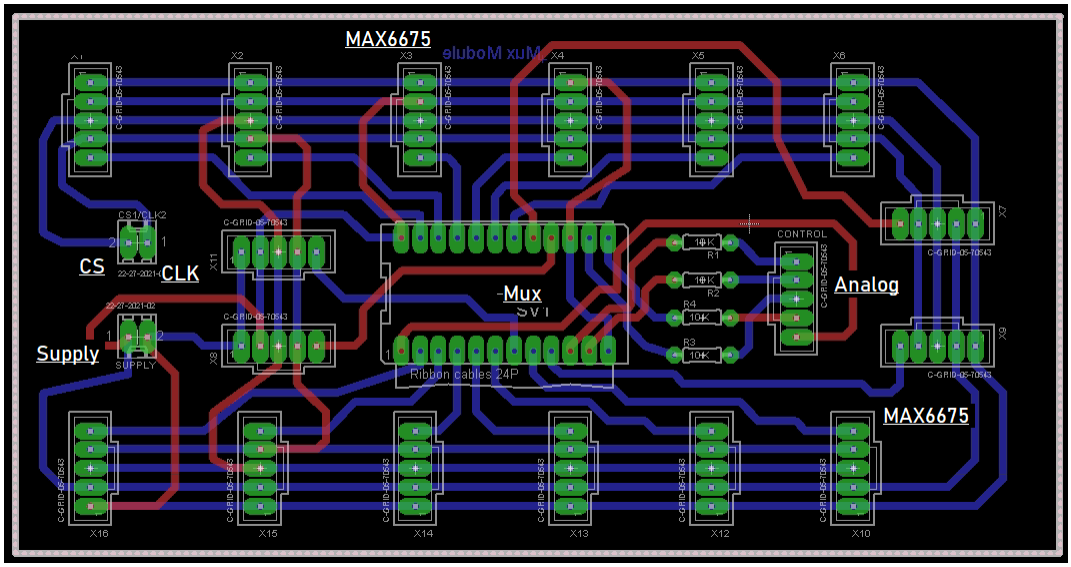

Figure A.3: Schematic of the Mux Module PCB. This module accomodates the multiplexer (mux) and the MAX6675 sensors. In order to receive communication from the Arduino Module, connections for the CS, CLK and Analog pins were made. The supply voltage from this circuit comes from the Arduino Module. It is clear from this picture how the multiplexer is a relevant addition to this circuit, providing a relative larger amount of possible sensors throughout our lab.

the circuit's adaptability and simplifies troubleshooting, aligning with the principles of effective electronic system architecture.

To delve deeper into the operational complexities of our temperature monitoring system, lets first consider the MAX6675 temperature sensors. As said, these sensors are employed as the primary temperature sensing elements in the circuit, and operate on the principle of converting thermocouple-induced voltage into digital temperature values. The MAX6675 sensors feature three main pins: Clock (CLK), Chip Select (CS), and Signal Output (SO).

Both the CLK and CS pins serve as input pins, allowing for their connection to multiple sensors. This connectivity feature is essential when employing multiple sensors in a single circuit, simplifying the connection and ensuring efficient utilization of available pins. However, the SO pin, serving as an output pin, requires a dedicated connection for each sensor. Since the Arduino have limited pin available, the solution to this challenge was to integrate a component know as multiplexer, sophisticated logic gates that offer a systematic mechanism for reading multiple sensors.

The multiplexer becomes a key component in our circuit due to its operation as a logical gate that offers 16 possible read pins controlled by four input control pins. This interesting design allows for the selective reading of each MAX6675 sensor through binary code communication using the four control pins. The response read from the selected sensor is then transmitted to the Arduino through the response pin (SO), facilitating a streamlined process of data acquisition. In scenarios

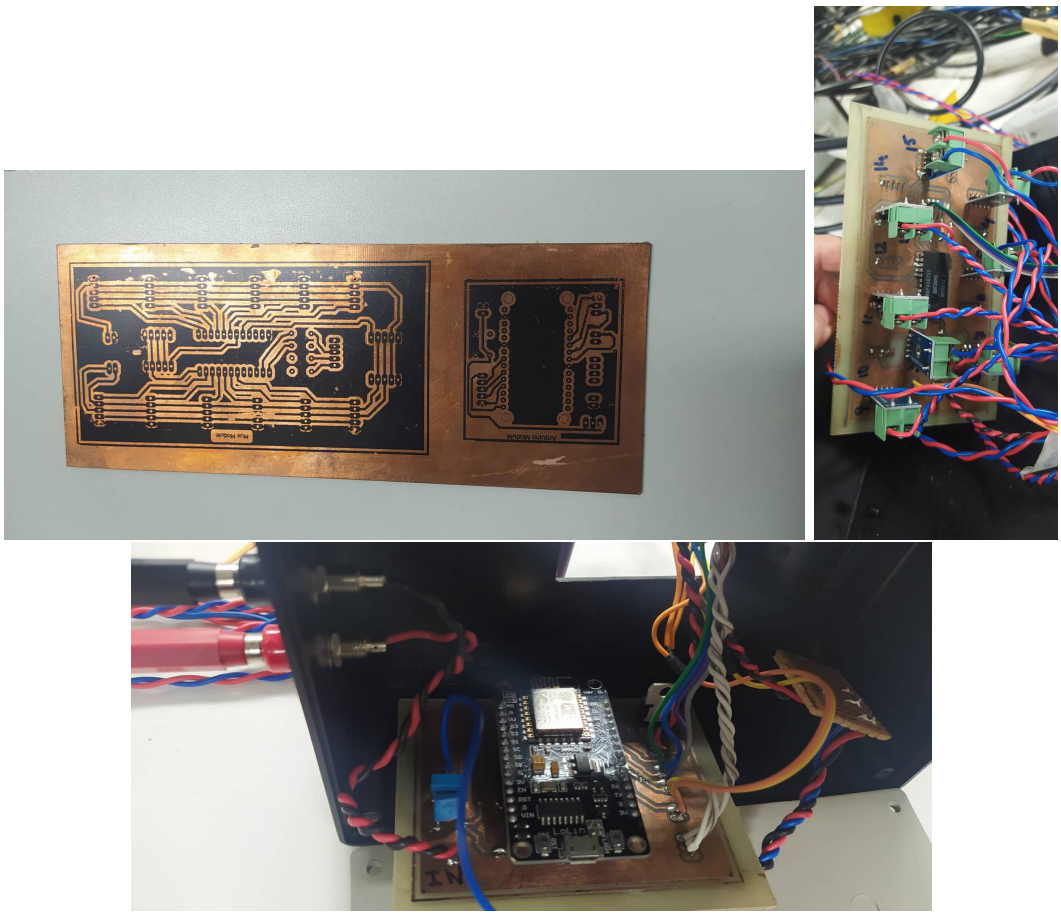

Figure A.4: In the top-left corner is a photo of the PCB designed for this project before the corrosion process needed for fabrication. On this case, both the Arduino and Mux modules underwent this process simultaneously. The top-right image displays the final Mux Module PCB with all components installed, while the bottom section showcases the completed Arduino Module PCB. These visuals illustrate the evolution from the initial design phase to the fully integrated PCBs for both modules.

where the number of MAX6675 sensors surpasses the available Arduino pins, the use of the multiplexer becomes clear. Without the multiplexer, each additional sensor would demand two more pins (three in total: SO, CLK and CS), limiting the system to a mere 9 different thermocouples. The incorporation of multiplexers removes this constraint, enabling the simultaneous monitoring of up to 16 thermocouples per multiplexer (with two multiplexers total per circuit) without imposing impractical limitations on the system's scalability. Furthermore, the incorporation of the LM7805 voltage regulator also ensures the upscale of this system, maintaining a stable power supply for both the Arduino and multiplexer modules. This voltage regulator, positioned within the Arduino module, exemplifies a thoughtful design choice aimed at optimizing power distribution. By supplying voltage to both modules and allowing for the extension of power to potential future Mux modules, this regulator enhances the circuit's modularity and adaptability.

The modularity of the temperature monitoring circuit I've built is a feature that provides

Figure A.5: Temperature monitoring graphs at ThingSpeak, with data collected over different points at our experiment.

advantages to this project, as it facilitates maintenance, diagnostics, and potential future expansions. So far, we only use one multiplexer at our lab, but not only does the circuit already have the capability of providing an extra multiplexer, it also have room for design improvement that may or may not provide more possible multiplexers per Arduino Modules. The molex connectors employed for module interconnection exemplify this modularity, allowing for the separation of the Arduino and Mux modules when required. This modularity extends beyond the immediate circuitry, as the connectors necessary for additional Mux modules have been incorporated into the Sr circuit. This forward-thinking design approach simplifies the integration of multiple modules without compromising the structural integrity of the system.

Having all the data collected correctly by the combination of sensors and the multiplexers, what is needed to be done next is to sent the data to ThingSpeak. Due to the Wi-Fi connection provided by the ESP8266 variant, the only necessary step in order to achieve this was to code correctly both the Wi-Fi and the ThingSpeak account connections. One can create a ThingSpeak account for free, but it will be limited regarding the number of channels available. Each channel support up to eight graphs, meaning eight different MAX6675 temperature sensors.

Figure A.6 shows the temperature data collected over more than two weeks. It is important to notice how the temperature fluctuations passes the confidence interval proposed by the air conditioning manufacturer, which was $\pm 1°C$. This is relevant since at our experiment, a lot of different

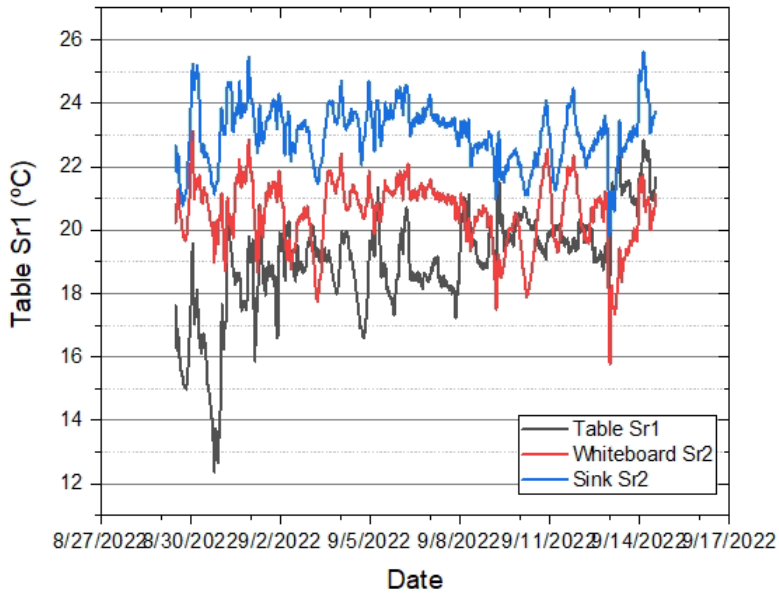

Figure A.6: Temperature data monitored through more than two weeks in order to measure temperature fluctuations. It is noticeable how the temperatures in different part of the labs fluctuates way more than a $\pm 1°C$ interval, which was the air conditioning manufacturer confidence fluctuation interval.

delicate apparatus need a stable room temperature in order to maintain data reproducibility. This includes not only the super cavity located at the red system, for example, but also all the mirrors used to align all of our beams, becoming a crucial problem if such beams were necessary to be re-aligned every day due to temperature changes. Of course, factors as temperature isolating systems could be employed in the lab room itself, but that means a high money cost, which is impracticable once the experiment is up and running. The main concern was the new air conditioning, which offered a specific temperature interval, but did not delivered. Precautions to avoid high fluctuations are always employed, such as periodic filter changes, but a better solution is still to be found.

As of the writing of this thesis, we currently have 16 operational MAX6675 temperature sensors distributed across various sections of our experiment. These sensors play a crucial role in gathering comprehensive data not only on the temperature dynamics within our workspace but also on the experiment's intricate behavior. The project's capacity to measure temperature serves as a valuable experimental ally, offering insights into a variable necessary for optimizing the ambient conditions essential to the advancement of our research. The real-time data acquisition provided by these sensors enhances the experimental setup's versatility and contributes significantly to the precision and control required for the research protocols in progress. Last but not least, in the following pages is the code I wrote for this circuit, which was uploaded to the ESP8266 Arduino module.

Listing A.1: Code used for this Temperature Monitoring Project

```
/*
 Every arduino code runs with a specific order:
1st) Include the libraries that will be used;
2nd) Declare the variables;
3rd) Specify the 'void setup()' function: steps that will be done just
   once by your code;
4th) Specify the 'void loop()' function: steps that will repeat itself
   indefinitely;
5th) Other may or may not used functions;

This code has a purpose of measuring temperatures with multiple MAX6675,
    using a comunication between
multiples multiplexers and the ESP8266 arduino wifi module.
*/


//-------------- Step one: including libraries --------------//

#include <ESP8266WiFi.h>  /*arduino library*/
#include <max6675.h>
#include <ThingSpeak.h>


//-------------- Step two: declare variables ---------------//


#define TIME_BETWEEN_READINGS    20000 /*ms*/

/*
Declaring the Arduino pins related to the Max6675 sensors. It functions
   with 3 signals: i)Clock (CLK), ii) Channel Select (CS, input), iii)
   Signal OutPut (SO).
At the circuit, the pin SO is the Output from our Multiplexer (pin Z at
   the multiplexer). We can use the same CLK and CS for all of them, but
    only one SO per multiplexer.
If you are using more than one Multiplexer Module, uncomment the others
   pin_SO elements.
*/
```

```
#define pin_CLK D5
#define pin_CS  D4
#define pin_SO  D6
//#define pin_SO_2  D7
//#define pin_SO_3  D8

//-- Wifi & ThingSpeak login --//

char ssid[] = "StrontiumLab"; /*wifi network name*/
char pass[] = "$trontium88"; /*wifi password*/

WiFiClient client;


//Login: strontium@ifsc.usp.br
//Password: $r88-707Lab


/*Login and Password for ThingSpeak channels, you need one per
   ThingSpeak channel (each channel suports 8 graphs).*/


//Channel 1 (at our ThingSpeak, it is labelled 'Optical Tables'):
unsigned long OpticalTablesID = 1834835;
char *OpticalTablesKey = "05Q63PMPDJ0FSH6I";



//Channel 2 (Lab Temperatures):
unsigned long LabTemperaturesID = 1834836;
char *LabTemperaturesKey = "OG0IZK2IUPD8W99P";




//-- Defining the Mux thermocouples readings --//

/*
If you are using more than one Multiplexer Module, uncomment the others
   Max6675 elements.
```

```
The order must always be: CLK, CS and then SO.
*/

MAX6675 termopar(pin_CLK, pin_CS, pin_SO);
//MAX6675 termopar2(pin_CLK, pin_CS, pin_SO_2);
//MAX6675 termopar3(pin_CLK, pin_CS, pin_SO_3);



//-- Variables for Thermistor reading --//

/*
This section is quite specific, if you don't have a thermistor you want
   to measure, you can go for Step Three.
Here we not only indicates the pins related to the thermistor but also
   calculates its resistance. The c coeficients we got from the
   datasheet.
*/

int ThermistorPin = A0; //AnalogPin A0
int Vo; //Voltage value in Bits
const float analogLimit = 3.3; //Limit of Analog In
const float analogLimitReal = 3.30011; //Analog Limit fitted from
   circuit characterization
float VoVolts; //Voltage Value in Volts
const float R1 = 0.8344; //resistance, in units of 10k Ohms, fitted from
    circuit characterization
float logRth, Rth, T, Tc;
float c1 = 3.3540154e-3, c2 = 2.5627725e-4, c3 = 2.0829210e-6, c4 =
   7.3003206e-8; //Thermistor coeficients from datasheet



//-------------- Step three: 'void setup()' ---------------//

void setup() {
  // put your setup code here, to run once:

  Serial.begin(115200);
  WiFi.mode(WIFI_STA);
```

```
  ThingSpeak.begin(client);

  pinMode(D3, OUTPUT);
  pinMode(D2, OUTPUT);
  pinMode(D1, OUTPUT);
  pinMode(D0, OUTPUT);

}



//--------------- Step four: 'void loop()' ---------------//


void loop() {
  // put your main code here, to run repeatedly:


  //-- Loop for WiFi connection --//

  if(WiFi.status() != WL_CONNECTED){
    while(WiFi.status() != WL_CONNECTED){
      WiFi.begin(ssid, pass);  // Connect to WPA/WPA2 network. Change
         this line if using open or WEP network
      delay(5000);
    }
  }



/*
From this point on, if you have more than one Channel at the ThingSpeak,
    you should separate the elements that will be at the first channel
   from the elements of the second channel etc.
The basic order for it to function the right way is to first put the
   elements at each field, then the channel you want that element to be
   in.
For example: Thermistor will be at field 7 from channel 1. So first we
   write the value read from the Thermistor at its specific field with '
   ThingSpeak.setField(field_number,value)'.
```

```
After all the elements have been writen, we then specify the channel
   with 'ThingSpeak.writeFields(Channel_ID, Channel_WriteKey)'.
*/



  /*
  Optical Tables Channel
  */

  //-- Reading Thermistor Temperature --//

  Vo = analogRead(ThermistorPin);
  VoVolts = (float)Vo * (analogLimit/1024);
  Rth = VoVolts * R1 / (analogLimitReal - VoVolts);
  logRth = log(Rth);
  T = (1.0 / (c1 + c2*logRth + c3*logRth*logRth + c4*logRth*logRth*
     logRth));
  Tc = T - 273.15;
  delay(4000);
  ThingSpeak.setField(7,Tc); //It creates a graph at field 7 from
     ThingSpeak, ploting the value 'Tc'


  //-- Defining the Mux ports --//

  /* If you are using more than one Multiplexer Modules, add more 'float
     ' elements as you need them. I also prefered to separate the
     float_Temps used for channel 1 from the ones used at
  channel 2. I don't think there's any problem not doing this but I keep
      it that way since I find easier to understand. There are some
     pin_Temp_i commented bellow, if you want you can
  just uncomment these when using more than one Multiplexer Modules. */

  float pin_Temp[6];
  //float pin_Temp_2[9];
  //float pin_Temp_3[9];

   mux (0,0,0,1);  //Set the multiplexer to door 1 (meaning Thermocouple
       2; Thermocouple X = multiplexer door Y + 1), this function will
      be defined at step 5
```

```
  delay(4000);
  pin_Temp[0] = termopar.readCelsius(); //read as temperature
  //pin_Temp_2[0] = termopar2.readCelsius();
  //pin_Temp_3[0] = termopar3.readCelsius();
  delay(4000);
  ThingSpeak.setField(1,pin_Temp[0]);
  //Serial.print("T2: ");
  //Serial.print(pin_Temp[0]);
  //Serial.println("C");


  mux (0,1,0,0);  //Set the multiplexer to door 4 (Thermocouple 5)
  delay(4000);
  pin_Temp[1] = termopar.readCelsius(); //read as temperature
  //pin_Temp_2[1] = termopar2.readCelsius();
  //pin_Temp_3[1] = termopar3.readCelsius();
  delay(4000);
  ThingSpeak.setField(2,pin_Temp[1]);
  //ThingSpeak.setField(2,pin_Temp_2[1]);
  //ThingSpeak.setField(3,pin_Temp_3[1]);


  mux (0,1,1,0);  //Set the multiplexer to door 6 (Thermocouple 7)
  delay(4000);
  pin_Temp[2] = termopar.readCelsius(); //read as temperature
  //pin_Temp_2[2] = termopar2.readCelsius();
  //pin_Temp_3[2] = termopar3.readCelsius();
  delay(4000);
  ThingSpeak.setField(3,pin_Temp[2]);
  //ThingSpeak.setField(2,pin_Temp_2[2]);
  //ThingSpeak.setField(3,pin_Temp_3[2]);


  mux (1,0,0,0);  //Set the multiplexer to door 8 (Thermocouple 9)
  delay(4000);
  pin_Temp[3] = termopar.readCelsius(); //read as temperature
  //pin_Temp_2[3] = termopar2.readCelsius();
  //pin_Temp_3[3] = termopar3.readCelsius();
  delay(4000);
  ThingSpeak.setField(4,pin_Temp[3]);
```

```
 //ThingSpeak.setField(2,pin_Temp_2[3]);
 //ThingSpeak.setField(3,pin_Temp_3[3]);


 mux (1,0,1,0);  //Set the multiplexer to door 10 (Thermocouple 11)
 delay(4000);
 pin_Temp[4] = termopar.readCelsius(); //read as temperature
 //pin_Temp_2[4] = termopar2.readCelsius();
 //pin_Temp_3[4] = termopar3.readCelsius();
 delay(4000);
 ThingSpeak.setField(5,pin_Temp[4]);
 //ThingSpeak.setField(2,pin_Temp_2[4]);
 //ThingSpeak.setField(3,pin_Temp_3[4]);


 mux (1,1,0,0);  //Set the multiplexer to door 12 (Thermocouple 13)
 delay(4000);
 pin_Temp[5] = termopar.readCelsius(); //read as temperature
 delay(4000);
 //pin_Temp_2[5] = termopar2.readCelsius();
 //pin_Temp_3[5] = termopar3.readCelsius();
 ThingSpeak.setField(6,pin_Temp[5]);
 //ThingSpeak.setField(2,pin_Temp_2[5]);
 //ThingSpeak.setField(3,pin_Temp_3[5]);


 ThingSpeak.writeFields(OpticalTablesID, OpticalTablesKey);

 delay(TIME_BETWEEN_READINGS); /* This delay is important so we have
    sufficient time for ThingSpeak to write everyfield before going to
     the next channel.
 We have another one after the second channel readings. */


/*
Lab Temperatures Channel
*/

float pin_Temp2[8];
```

```
mux (0,0,0,0);  //Set the multiplexer to door 0 (Thermocouple 1)
delay(4000);
pin_Temp2[0] = termopar.readCelsius(); //read as temperature
//pin_Temp_2[6] = termopar2.readCelsius();
//pin_Temp_3[6] = termopar3.readCelsius();
delay(4000);
ThingSpeak.setField(1,pin_Temp2[0]);
//ThingSpeak.setField(2,pin_Temp_2[6]);
//ThingSpeak.setField(3,pin_Temp_3[6]);
//Serial.print("T1: ");
//Serial.print(pin_Temp[6]);
//Serial.println("C");

mux (0,0,1,0);  //Set the multiplexer to door 2 (Thermocouple 3)
delay(4000);
pin_Temp2[1] = termopar.readCelsius(); //read as temperature
//pin_Temp_2[7] = termopar2.readCelsius();
//pin_Temp_3[7] = termopar3.readCelsius();
delay(4000);
ThingSpeak.setField(2,pin_Temp2[1]);
//ThingSpeak.setField(2,pin_Temp_2[7]);
//ThingSpeak.setField(3,pin_Temp_3[7]);


mux (0,0,1,1);  //Set the multiplexer to door 3 (Thermocouple 4)
delay(4000);
pin_Temp2[2] = termopar.readCelsius(); //read as temperature
//pin_Temp_2[8] = termopar2.readCelsius();
//pin_Temp_3[8] = termopar3.readCelsius();
delay(4000);
ThingSpeak.setField(3,pin_Temp2[2]);
//ThingSpeak.setField(2,pin_Temp_2[8]);
//ThingSpeak.setField(3,pin_Temp_3[8]);
//Serial.print("Temperatura 8: ");
//Serial.print(pin_Temp[0]);
//Serial.println("C");

mux (0,1,0,1);  //Set the multiplexer to door 5 (Thermocouple 6)
delay(4000);
```

```
pin_Temp2[3] = termopar.readCelsius(); //read as temperature
//pin_Temp_2[9] = termopar2.readCelsius();
//pin_Temp_3[9] = termopar3.readCelsius();
delay(4000);
ThingSpeak.setField(4,pin_Temp2[3]);
//ThingSpeak.setField(2,pin_Temp_2[9]);
//ThingSpeak.setField(3,pin_Temp_3[9]);

mux (0,1,1,1);  //Set the multiplexer to door 7 (Thermocouple 8)
delay(4000);
pin_Temp2[4] = termopar.readCelsius(); //read as temperature
//pin_Temp_2[10] = termopar2.readCelsius();
//pin_Temp_3[10] = termopar3.readCelsius();
delay(4000);
ThingSpeak.setField(5,pin_Temp2[4]);
//ThingSpeak.setField(2,pin_Temp_2[10]);
//ThingSpeak.setField(3,pin_Temp_3[10]);
//Serial.print("Temperatura 10: ");
//Serial.print(pin_Temp[1]);
//Serial.println("C");

mux (1,0,0,1);  //Set the multiplexer to door 9 (Thermocouple 10)
delay(4000);
pin_Temp2[5] = termopar.readCelsius(); //read as temperature
//pin_Temp_2[11] = termopar2.readCelsius();
//pin_Temp_3[11] = termopar3.readCelsius();
delay(4000);
ThingSpeak.setField(6,pin_Temp2[5]);
//ThingSpeak.setField(2,pin_Temp_2[11]);
//ThingSpeak.setField(3,pin_Temp_3[11]);
//Serial.print("Temperatura 1: ");
//Serial.print(pin_Temp[0]);
//Serial.println("C");

mux (1,0,1,1);  //Set the multiplexer to door 11 (Thermocouple 12)
delay(4000);
pin_Temp2[6] = termopar.readCelsius(); //read as temperature
//pin_Temp_2[12] = termopar2.readCelsius();
//pin_Temp_3[12] = termopar3.readCelsius();
delay(4000);
```

```
ThingSpeak.setField(7,pin_Temp2[6]);
//ThingSpeak.setField(2,pin_Temp_2[12]);
//ThingSpeak.setField(3,pin_Temp_3[12]);
//Serial.print("Temperatura 12: ");
//Serial.print(pin_Temp[2]);
//Serial.println("C");

mux (1,1,1,0);  //Set the multiplexer to door 14 (Thermocouple 15)
delay(4000);
pin_Temp2[7] = termopar.readCelsius(); //read as temperature
//pin_Temp_2[13] = termopar2.readCelsius();
//pin_Temp_3[13] = termopar3.readCelsius();
delay(4000);
ThingSpeak.setField(8,pin_Temp2[7]);
//ThingSpeak.setField(2,pin_Temp_2[13]);
//ThingSpeak.setField(3,pin_Temp_3[13]);

//mux (1,1,1,0);  //Set the multiplexer to door 14
//delay(2000);
//pin_Temp2[8] = termopar.readCelsius(); //read as temperature
//pin_Temp_2[14] = termopar2.readCelsius();
//pin_Temp_3[14] = termopar3.readCelsius();
//ThingSpeak.setField(1,pin_Temp2[9]);
//ThingSpeak.setField(2,pin_Temp_2[14]);
//ThingSpeak.setField(3,pin_Temp_3[14]);

//mux (1,1,1,1);  //Set the multiplexer to door 15
//delay(2000);
//pin_Temp2[9] = termopar.readCelsius(); //read as temperature
//pin_Temp_2[15] = termopar2.readCelsius();
//pin_Temp_3[15] = termopar3.readCelsius();
//ThingSpeak.setField(7,pin_Temp2[9]);
//ThingSpeak.setField(2,pin_Temp_2[15]);
//ThingSpeak.setField(3,pin_Temp_3[15]);*/


ThingSpeak.writeFields(LabTemperaturesID, LabTemperaturesKey);
```

```
   delay(TIME_BETWEEN_READINGS);


}


//--------------- Step five: other functions ---------------//

//-- Function used to implement the binary reading of the Mux's ports.
/* The order here is important since it writes the mux element as: A3 A2
    A1 A0 (meaning that door 1010, or door 10, is A3 = 1; A2 = 0, A1 = 1
    and A0 = 0) */
void mux (int state1,int state2,int state3,int state4){

digitalWrite(D3, state1); //A3 port from the mux
digitalWrite(D2, state2); //A2 port from the mux
digitalWrite(D1, state3); //A1 port from the mux
digitalWrite(D0, state4); //A0 port from the mux

}
```

BIBLIOGRAPHY

[1] et al Rui-Bo Jin. Quantum interferometers: principles and applications. *arXiv:2310.16378*.

[2] Martin Ryle. Radio telescopes of large resolving power. *Nobel Lectures*, Physics 1971-1980:187–203, 1974. URL https://www.nobelprize.org/prizes/physics/1974/ryle/lecture/.

[3] et al Min Shao. The mark iii stellar interferometer. *Astronomy and Astrophysics (ISSN 0004-6361)*, 193:357–371, 1988. URL https://ui.adsabs.harvard.edu/abs/1988A%26A...193..357S/abstract.

[4] et al Min Bao. Uncovering the formation of the counter-rotating stellar discs in sdss j074834.64+444117.8. *Monthly Notices of the Royal Astronomical Society*, 528:2643–2652, 2024. URL https://ui.adsabs.harvard.edu/abs/1988A%26A...193..357S/abstract.

[5] et al Gael Chauvin. Chasing extreme planetary architectures: I- hd 196885 ab, a super-jupiter dancing with two stars? *Astronomy Astrophysics (AA)*, 675, 2023. URL https://www.aanda.org/articles/aa/full_html/2023/07/aa44502-22/aa44502-22.html.

[6] et al Zhihui Feng. High precision line-of-sight angle measuring and large ranging laser radar system for deep-space rendezvous and docking. *Optica Publishing Group: Applied Optics*, 59:10565–10573, 2020. URL https://opg.optica.org/ao/abstract.cfm?uri=ao-59-33-10565.

[7] Alexander Hellemans Bryan Bunch. *The History of Science and Technology*. Scientific Publishing, Inc, 2004.

[8] et al B.P. Abbott. Observation of gravitational waves from a binary black hole merger. *Physical Review Letters*, 116:061102–1 – 061102–16, 2016. URL https://journals.aps.org/prl/abstract/10.1103/PhysRevLett.116.061102.

[9] et al Lahaye. Evaporative cooling of a guided rubidium atomic beam. *Physical Review A*, 72, 2005.

[10] Patrícia Castilho. *New experimental system to study coupled vortices in a two-species Bose-Einstein condensate ^{23}Na-^{41}K with tunable interactions*. PhD thesis, Instituto de Física de São Carlos - IFSC, Universidade de São Paulo - USP, 2017.

[11] Simon Stellmer. *Degenerate quantum gases of strontium*. PhD thesis, Faculty of Mathematics, Computer Science and Physics, University of Innsbruck, 2013.

[12] Cord Axel Müller. *Schwache Lokalisierung von Licht in einem Gas kalter Atome: koh arente Ruckstreuung und interne Quantenstruktur*. PhD thesis, École doctorale: Sciences Fondamentales et Appliquées, Université de Nice Sophia-Antipolis, 2001.

[13] R. Corey; M. Kissner; P. Saulnier. Coherent backscattering of light. *American Journal of Physics*, 63(6):560–564, 1995.

[14] Joseph W. Goodman. *Speckle Phenomena in Optics: Theory and Applications*. Roberts and Company Publishers, 2007.

[15] et al P. H. Moriya. Coherent backscattering of inelastic photons from atoms and their mirror images. *Physical Review A*, 94(053806), 2016.

[16] et al T. Wellens. Coherent backscattering of light by two atoms in the saturated regime. *Physical Review A*, 70(023817), 2004.

[17] E. Noether. Invariante variationsprobleme. *Nachrichten von der Gesellschaft der Wissenschaften zu Göttingen, Mathematisch-Physikalische Klasse*, pages 235–257, 1918.

[18] Emmy Noether. Invariant variation problems. *Transport Theory and Statistical Physics*, 1 (3):186–207, jan 1971. doi: 10.1080/00411457108231446. URL https://doi.org/10.1080/00411457108231446.

[19] R J Potton. Reciprocity in optics. *Reports on Progress in Physics*, 67(5):717–754, April 2004. doi: 10.1088/0034-4885/67/5/r03. URL https://doi.org/10.1088/0034-4885/67/5/r03.

[20] R. Carminati, J. J. Sáenz, J.-J. Greffet, and M. Nieto-Vesperinas. Reciprocity, unitarity, and time-reversal symmetry of the s matrix of fields containing evanescent components. *Phys. Rev. A*, 62:012712, Jun 2000. doi: 10.1103/PhysRevA.62.012712. URL https://link.aps.org/doi/10.1103/PhysRevA.62.012712.

[21] S. Pancharatnam. Generalized theory of interference, and its applications. *Proceedings of the Indian Academy of Sciences - Section A*, 44(5):247–262, November 1956. doi: 10.1007/bf03046050. URL https://doi.org/10.1007/bf03046050.

[22] M.V. Berry. The adiabatic phase and pancharatnam's phase for polarized light. *Journal of Modern Optics*, 34(11):1401–1407, November 1987. doi: 10.1080/09500348714551321. URL https://doi.org/10.1080/09500348714551321.

[23] Peter van der Straten Harold J. Metcalf. *Laser Cooling and Trapping*. Springler-Verlag New York, 1999.

[24] Claude Cohen-Tannoudji. *Quantum Mechanics*. 1973.

[25] Pedro Henrique Nantes Magnani. Armadilha Óptica de dipolo para sr^{88}. Master's dissertation, Departamento de Física, Universidade Federal de São Carlos - UFSCar, 2019.

[26] Paulo Hisao Moriya. *Collective effects in light scattering from cold strontium clouds*. PhD thesis, Instituto de Física de São Carlos - IFSC, Universidade de São Paulo - USP, 2016.

[27] Christopher J. Foot. *Atomic Physics*. Oxford University P, 2003.

[28] et al Moriya. Comparison between 403 nm and 497 nm repumping schemes for strontium magneto-optical traps. *Journal of Physics Communications*, 2(12), 2018.

[29] Weng W. Chow. Theory of line narrowing and frequency selection in an injection locked laser. *IEEE Journal of Quantum Electronics*, QE-19(2):243–249, 1986.

[30] John David Jackson. *Classical Electrodynamics*. John Wiley Sons, 1962.

[31] Moysés Nussenzveig. *Curso de Física Básica Vol. 2: Fluidos, Oscilações e ondas, Calor*. Editora Blucher, .

[32] Moysés Nussenzveig. *Curso de Física Básica Vol. 4: Ótica, Relatividade, Física Quântica*. Editora Blucher, .

[33] Tabish Qureshi. Coherence, interference and visibility. *Quanta*, 8:24–35, 2019.

[34] Parameswaran Hariharan. *Basics of Interferometry*. Academic Press, 2007.

[35] Elias N. Glytsis. Spatial and temporal coherence. Slides presentation, 2023. URL http://users.ntua.gr/eglytsis/OptEng/Coherence_p.pdf. School of Electrical Computer Engineering National Technical University of Athens.

[36] Christopher Gerry Peter Knight. *Introductory Quantum Optics*. Cambridge University Press, 2004.

[37] Rodney Loundon. *The Quantum Theory of Light*. Oxford Science Publications, 1973.

[38] Marlan O. Scully; M. Suhail Zubairy. *Quantum Optics*. Cambridge University Press, 1997.

[39] Claude Cohen-Tannoudji; Jacques Dupont-Roc; Gilbert Grynberg. *Atom-Photon Interactions: Basic Processes and Applications*. John Wiley Sons, 1998.

[40] Pablo Gabriel Santos Dias. Coerência espectral da luz espalhada por Átomos frios saturados. Master's dissertation, Physics Department, Federal University of São Carlos - UFSCar, 2017.

[41] Bejamin R. Mollow. Power spectrum of light scattered by two-level systems. *Physical Review*, 188, 1969.

[42] Nicola Piovella et al. Mirror-assisted coherent backscattering from the mollow sidebands. *Physical Review A*, 96(053852), 2017.

[43] R. Clark Jones. A new calculus for the treatment of optical SystemsI description and discussion of the calculus. *Journal of the Optical Society of America*, 31(7):488, July 1941. doi: 10.1364/josa.31.000488. URL https://doi.org/10.1364/josa.31.000488.

[44] Edward Collett. Equation summary. In *Field Guide to Polarization*, pages 114–123. SPIE, 1000 20th Street, Bellingham, WA 98227-0010 USA, 2009.

[45] et al Pablo G. S. Dias. Mirror-assisted backscattering interferometry to measure the first-order correlation function of the light emitted by quantum scatterers. *Physical Review A*, 104, 2021.

[46] Wolfgang Dultz; D. B. P. Telekorn Darmstadt. Pancharatnam's phase in polarization optics. *Advanced Electromagnetism: Foundations, Theory and Applications*, pages 357–375, 1995.

[47] Philip W Anderson. Absence of diffusion in certain random lattices. *Physical review*, 109(5): 1492, 1958.

[48] Eric Akkermans and Gilles Montambaux. *Mesoscopic physics of electrons and photons*. Cambridge university press, 2007.

[49] Yasuo Kuga and Akira Ishimaru. Retroreflectance from a dense distribution of spherical particles. *J. Opt. Soc. Am. A*, 1(8):831–835, Aug 1984. doi: 10.1364/JOSAA.1.000831. URL https://opg.optica.org/josaa/abstract.cfm?URI=josaa-1-8-831.

[50] G. Labeyrie, F. de Tomasi, J.-C. Bernard, C. A. Müller, C. Miniatura, and R. Kaiser. Coherent backscattering of light by cold atoms. *Phys. Rev. Lett.*, 83:5266–5269, Dec 1999. doi: 10.1103/PhysRevLett.83.5266. URL https://link.aps.org/doi/10.1103/PhysRevLett.83.5266.

[51] M. Gross and S. Haroche. Superradiance: An essay on the theory of collective spontaneous emission. *Physics Reports*, 93(5):301–396, December 1982. doi: 10.1016/0370-1573(82)90102-8. URL https://doi.org/10.1016/0370-1573(82)90102-8.

[52] Tobias Micklitz, Cord A Müller, and Alexander Altland. Echo spectroscopy of anderson localization. *Physical Review B*, 91(6):064203, 2015.

[53] Kilian Müller, Jérémie Richard, Valentin V Volchkov, Vincent Denechaud, Philippe Bouyer, Alain Aspect, and Vincent Josse. Suppression and revival of weak localization through control of time-reversal symmetry. *Physical Review Letters*, 114(20):205301, 2015.

[54] Clément Hainaut, Isam Manai, Jean-François Clément, Jean Claude Garreau, Pascal Szriftgiser, Gabriel Lemarié, Nicolas Cherroret, Dominique Delande, and Radu Chicireanu. Controlling symmetry and localization with an artificial gauge field in a disordered quantum system. *Nature communications*, 9(1):1382, 2018.